Observational studies of a dense cloud core on the verge of star formation

Ana Chacón Tanarro

München 2018

Observational studies of a dense cloud core on the verge of star formation

Ana Chacón Tanarro

Dissertation
an der Facultät für Physik
der Ludwig–Maximilians–Universität
München

vorgelegt von
Ana Chacón Tanarro
aus Madrid, Spanien

München, den 14. Mai 2018

Erstgutachter: Prof. Dr. Paola Caselli
Zweitgutachter: Prof. Dr. Thomas Preibisch
Tag der mündlichen Prüfung: 28. Juni 2018

Contents

List of Figures

List of Tables

Zusammenfassung

Prästellare Kerne vertreten die erste identifizierbare Stufe der Sternentwicklung und sind deshalb perfekte Laboratorien für Astronomen, um zu erforschen, wie unser eigenes Sonnensystem entstanden ist. Diese Arbeit konzentriert sich auf L1544, ein prästellarer Kern, der mit einer Entfernung von 140 pc zu uns in der nahe gelegenen Taurus Molekülwolke sitzt. Die Lage erlaubt uns, die innere Struktur des Kerns mit gegenwärtig nutzbaren Teleskopen aufzulösen und in die inneren, sehr dichten Bereiche hinein zu zoomen. Der Kern zeigt klare Merkmale von Kontraktion und chemischer Evolution und sein Kern ist sehr dicht ($n_{\mathrm{H_2}} > 10^7 \mathrm{cm}^{-3}$) und kalt ($T < 7$ K). Die physikalische Struktur von L1544 wurde kürzlich modelliert und dieses Modell stimmt gut mit der beobachteten molekularen Linien- und Kontinuumsemission überein. Darüber hinaus sagt das Modell einen Anstieg in der Staubopazität um einen Faktor von 4 in Richtung der zentralen Bereiche von L1544 voraus, die Staubkornkoagulation in Richtung des Zentrums suggeriert. Diese Theorie kann nur durch das Studium der Kontinuumsemission bei Millimeter Wellenlängen getestet werden, da dies das spektrale Fenster ist, bei dem man erwartet, dass es durch die Emission von großen Körnern beeinflusst wird. Gegenwärtig weiß man nicht, ob Kornkoagulation bereits während der prästellaren Phase, vor der Formation eines Protosterns, wirksam ist. Es ist wichtig, diesen Effekt zu studieren, da Staubkoagulation die Entstehung und Entwicklung einer protoplanetaren Scheibe beeinflussen kann.

In dieser Arbeit präsentiere ich Studien über Eigenschaften der Staubemission sowie physikalische und chemische Zustände im prästellaren Kern L1544. Diese Studien basieren auf Beobachtungen im Kontinuum und von spektralen Linien bei Millimeter Wellenlängen. Die Beobachtungen im Kontinuum mit dem IRAM 30 m Teleskop, vorgestellt im ersten Teil dieser Arbeit, kann mit einem konstanten Wert der Staubopazität und des Spektralindizes ohne irgendein Anzeichen von Kornwachstum in dessen Kern modelliert werden. Es zeigt sich jedoch, dass die räumliche Auflösung und die Sensitivität der Beobachtungen nicht ausreichen, um den vorhergesagten Effekt zu beobachten. Interferometer wie ALMA sollten allerdings in der Lage sein, Nachweise von Kornwachstum in den inneren 2000 AU des Kerns zu finden.

Der zweite Teil dieser Arbeit setzt sich mit deuteriertem Methanol (CH_2DOH), einem Molekül, das ausschließlich auf Staubkornoberflächen gebildet wird, und seiner Beziehung zu CO, H_2CO und deren Isotopologen auseinander. Zur Bildung von CH_2DOH benötigt man große Mengen CO auf den Körnern, deshalb ist es von Nutzen, beide Moleküle gleichzeitig zu erforschen. Vergleiche mit H_2CO, welches sich auch im Gaszustand bilden

kann, hilft die unterschiedlichen Bedingungen, welche Reaktionen in der Gasphase und festen Phase regulieren, zu verstehen. Wie erwartet beobachten wir, dass sich CH_2DOH und Methanol (CH_3OH) unter ähnlichen Bedingungen gut bilden und dass sich beide Spezies dort formen, wo CO ausreichend aufgebraucht ist. Auf der anderen Seite zeigen H_2CO und seine deuterierten Spezies andere Verteilungen als die von CH_3OH, CH_2DOH und $C^{17}O$, was andeutet, dass Reaktionen in der Gasphase eine wichtige Rolle spielen könnten. Der Vergleich von zwei unterschiedlichen chemischen Modellen zeigt, dass theoretische Berechnungen reaktionsfreudige Desorption, Quantentunneln und Zeitentwicklung berücksichtigen sollten. Auf den Bedarf an weiterer Arbeit im Labor wird ebenfalls hingewiesen.

Der letzte Teil dieser Arbeit konzentriert sich auf die Kontinuumsemission des Staubs von L1544 bei 1.1 und 3.3 mm. Diese neuen Karten, die mit zwei der neuesten Teleskope zur Beobachtung des Kontinuums im mm-Bereich (AzTEC im LMT und MUSTANG-2 im GBO) erlangt wurden, zeigen Gradienten in der Staubopazität verteilt in der gesamten Wolke, was mit Variationen in der Dicke der Eismäntel auf den Oberflächen der Staubkörner konsistent ist. Unsere Ergebnisse zeigen auch, dass gegenwärtige physikalische Beschreibungen der Wolke überarbeitet werden müssen.

Abstract

Pre-stellar cores represent the first identifiable stages of star formation, and are therefore perfect laboratories for astronomers to study how our own Solar system was formed. This thesis focuses on L1544, a pre-stellar core situated in the nearby Taurus Molecular Cloud, at a distance of 140 pc from us. The proximity allows us to resolve the inner structure of the core with currently available telescopes, and to zoom in on the inner, very dense regions. The core shows clear signs of contraction and chemical evolution, and its nucleus is very dense ($n_{\mathrm{H_2}} > 10^7$ cm^{-3}) and cold ($T < 7$ K). The physical structure of L1544 has been recently modeled, and this model agrees well with the observed molecular line and continuum emission. Moreover, the model predicts an increase in the dust opacity by a factor of 4 towards the central regions of L1544, which suggests grain coagulation towards the center. This theory can only be tested studying the continuum emission at millimeter wavelengths, as this is the spectral window expected to be affected by emission from large grains. Currently it is not known if grain coagulation is effective already during the pre-stellar phase, before the formation of a protostar. Studying this effect is important, as dust coagulation can affect the formation and evolution of protoplanetary disks.

In this thesis, I present studies of dust emission properties and physical and chemical conditions in the pre-stellar core L1544. These studies are based on continuum and spectral line observations at millimeter wavelengths. The continuum observations with the IRAM 30 m telescope, presented in the first part of this thesis, can be modeled with a constant value of the dust opacity and spectral index, with no indication of grain growth in this core. It is shown, however, that the spatial resolution and the sensitivity of the observations are not sufficient for detecting the predicted effect, but interferometers, such as ALMA, should be able to find evidence for grain growth in the inner 2000 au of the core.

The second part of this thesis discusses deuterated methanol (CH_2DOH), a molecule which is solely formed on the dust grain surfaces, and its relation to CO, H_2CO, and their isotopologues. The formation of CH_2DOH requires large amounts of CO on grains, so it is useful to study both molecules simultaneously. Comparison with H_2CO, which can also form in the gas, helps to understand the different conditions governing gas-phase and solid-phase reactions. As expected, we find that CH_2DOH and methanol (CH_3OH) thrive in similar conditions, and that both species form where CO is sufficiently depleted. On the other hand, H_2CO and its deuterated species show different distributions than those of CH_3OH, CH_2DOH, and $C^{17}O$, indicating that gas-phase reactions may play an important role. Comparison between two different chemical models shows that theoretical calculations

should take into account reactive desorption, quantum tunneling, and time evolution. A need for further laboratory work is also pointed out.

The last part of the thesis focuses on the dust continuum emission from L1544 at 1.1 and 3.3 mm. These new maps, obtained with two of the newest mm-continuum facilities (AzTEC at the LMT and MUSTANG-2 at the GBO) show gradients in the dust opacity across the cloud, which is consistent with variations in the thickness of the ice mantles on the dust grains surfaces. Our results also show that the current physical description of the cloud needs to be revised.

Chapter 1

Introduction

1.1 Low mass star formation

The interstellar medium (ISM) is formed of gas and dust, which represent 99% and 1% of its mass, respectively. It can be divided into five phases, depending on the temperature, density and chemical characteristics: hot ionized, warm ionized, warm neutral, cold neutral, and molecular. Temperature and density range from 10^5 K and $n \sim 3 \times 10^{-3}$ cm^{-3} in the hot ionized regions to 10 K and $n > 300$ cm^{-3} in the molecular regions. These temperatures and densities help to understand the form in which hydrogen is found: ionized, atomic or molecular.

In this work we focus on the molecular gas or clouds, which only represent 1% of the ISM. Although not abundant, they are important, as it is here where stars form. Star formation starts thanks to the influence of turbulence, magnetic fields and gravitational pressure. Denser regions of ∼0.1 pc in size can then be formed within molecular clouds, and they represent a decisive stage: they may further collapse due to gravitational forces, maintain or even dissipate due to, for example, gas pressure or magnetic fields. The criteria which is commonly used for determining if these sub-structures, usually called cores or clumps, can collapse or not is the Jeans criterion (or Jeans mass). This criterion determines the mass that a cloud needs to have in order to undergo gravitational collapse. The Jeans mass depends on the temperature and density of the gas in the following way:

$$M_{\rm J} = \left(\frac{5kT}{G\mu m_{\rm H}}\right)^{3/2} \left(\frac{3}{4\pi\rho}\right)^{1/2}, \tag{1.1}$$

where μ is the mean molecular weight, k the Boltzmann constant, T the temperature, G the gravitational constant, $m_{\rm H}$ the hydrogen atom mass and ρ the density.

Therefore, as one can see, the colder and denser a region is, the more favored the collapse is. For a typical dense core this criterion is satisfied when the mass overcomes 5 solar masses ($M_\odot$). However, as collapse proceeds, the energy coming from the gravitational collapse heats up the medium, increasing the Jeans mass and making it difficult to further collapse. This means that a cooling system is needed for avoiding the core to heat up.

There are two such mechanisms present in the ISM: the most efficient one is dust at volume densities above $\sim 10^5$ cm^{-3} (Goldsmith 2001), which transforms the gravitational energy into infrared emission; the second one is molecular emission, through the excitation of different molecular levels and the subsequent de-excitation.

Once the Jeans mass is overcome and the core is collapsing, it passes through several steps until a new star is formed (see Figure 1.1):

1. **Pre-stellar core.** Pre-stellar cores are starless cores which show clear signs of contraction, are self-gravitating and chemically evolved (Crapsi et al. 2005). Having temperatures of $\sim$10 K, these objects emit at sub- and millimeter- wavelengths.

2. **Class 0.** These objects are characterized by a central protostellar object and a massive envelope. Showing slightly higher temperatures than pre-stellar cores, their emission peak is in the far infrared around 100 μm. They still can fragment into a multiple system.

3. **Class I.** The envelope has mostly accreted its mass to a very thick disk, which surrounds a central object now called protostar. The emission peak is at mid infrared, around 24 μm.

4. **Class II or Classical T Tauri stars.** The envelope has disappeared, and the protostar, having almost its final mass, has started burning deuterium in its nucleus: now it is considered to be a pre-main sequence star. The spectral energy distribution (SED) of these objects clearly shows two components: the one from the star in the optical and the one from the disk (or protoplanetary disk) in the infrared. The disk will evolve and may form a planetary system.

5. **Class III or Weak T Tauri stars.** The disk of these objects has almost disappeared, and now it is called debris disk. This young star has already achieved its final mass and it is contracting and evolving towards the main sequence. The main emission from these objects is in the optical wavelength range.

Once the Class III stars start to burn hydrogen in their nuclei, a new main-sequence-star is born.

There are several star forming regions in our Galaxy, which depending on the environment, present different kinds of star formation. The Orion Molecular Cloud, for example, is a very dense and massive region giving birth to massive stars. On the contrary, Taurus or Lupus represent low-mass star forming regions, being more quiescent and less dense.

In this work we focus on what is considered the first stage of the process of star formation: pre-stellar cores (Bergin & Tafalla 2007; Caselli & Ceccarelli 2012). These systems are very dense ($>10^4$ cm^{-3}) and cold, and their study helps us to understand the physical and chemical evolution that our own Solar System underwent. For this, we study the properties of the dust and the gas, trying to connect both physical and chemical properties.

Therefore, an introduction to the emission coming from the dust, and also to that from the gas, is needed before entering into the details of the project here presented. This is provided in the following sections.

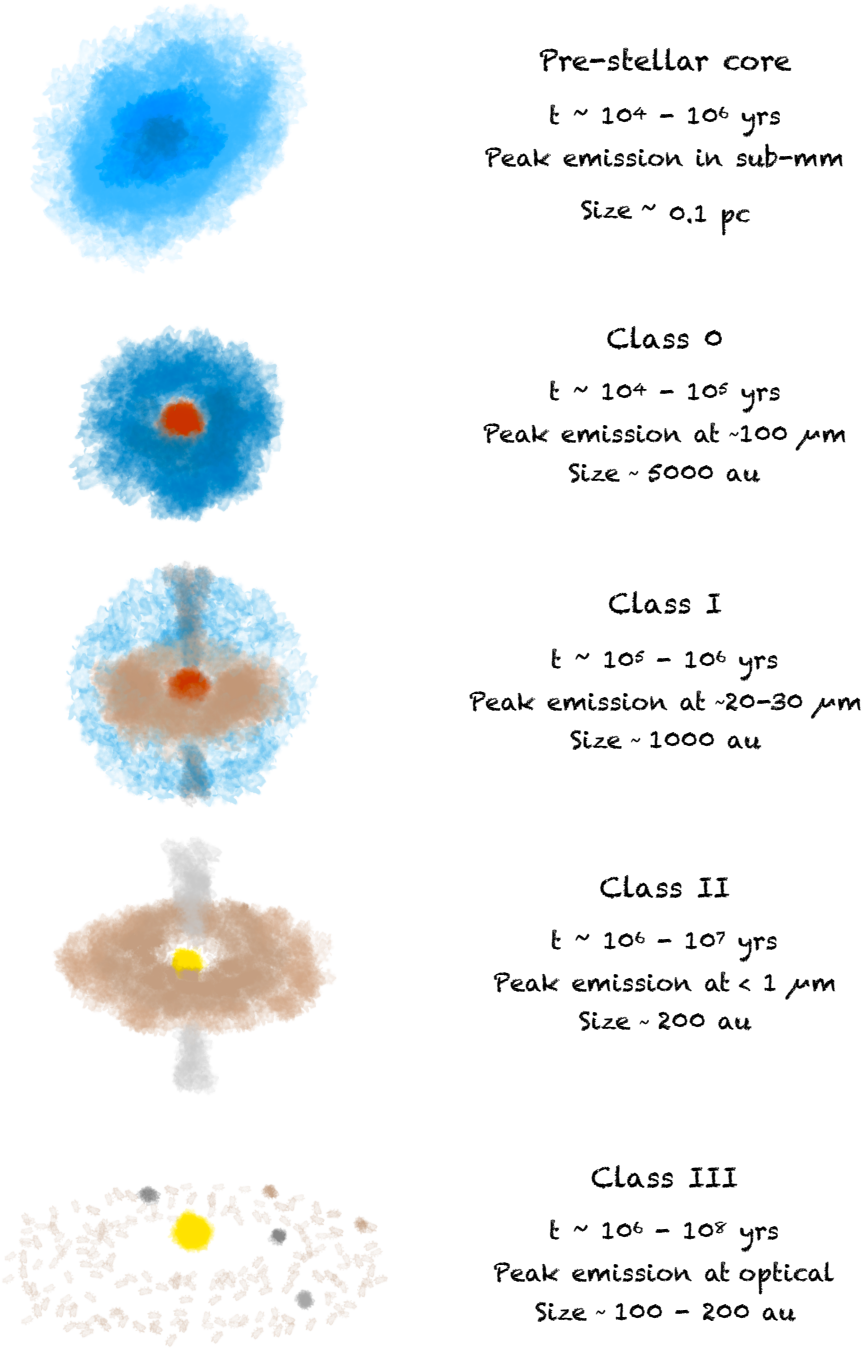

Figure 1.1: Schematic representation of the evolution of a pre-stellar core into a Class III object.

1.2 The study of the interstellar dust

The study of the night-sky view shows several dark clouds in the sky. Since William and Caroline Herschels' studies 200 years ago, astronomers did not know whether these dark clouds were caused by the lack of stars in those regions or by the presence of something attenuating their light. But after several studies focused on how the light of the same type of stars, determined by their spectroscopic features, vary in different regions, the answer was found: there was something in the interstellar medium attenuating the light of the stars. This attenuation was caused by solid particles, whose composition and form has been determined from the way the emission from stars was attenuated through the whole spectrum.

These solid particles were later named interstellar dust. As already mentioned, dust particles are only 1% of the mass of the ISM, and are formed in the envelopes of evolved stars. However, their presence is very important for the formation of stars and planets, and the chemical richness of the Universe. Their typical size is 0.1 μm, although they can grow up to kilometer sizes in protoplanetary disks, and they are formed mainly of silicates and carbonaceous material. Depending on their physical and chemical properties, they interact differently with the electromagnetic field, and are easily observable through 3 different phenomena: scattering and absorption (together they give the extinction) and emission.

1.2.1 Extinction

The extinction measures the absorption and scattering that the starlight suffers due to the interstellar material. By studying the dependence of the extinction of the starlight with wavelength (A_λ), it was discovered that generally $A_\lambda \propto \lambda^{-1}$, indicating that dust absorbs shorter wavelengths better. This effect is also known as reddening, as the bluer wavelengths are more affected by extinction. The dependency of the extinction on the wavelength was called the extinction curve, and it shows also some more localized spectroscopic characteristics which reflect the material which composes the dust grains, like the silicate absorption features at $\lambda = 9.7\,\mu$m and $18\,\mu$m, the hydrocarbon feature at $3.4\,\mu$m, and the Polycyclic Aromatic Hydrocarbons (PAHs) feature at 6.2 μm.

However, for a more detailed analysis of the extinction, the study of the interaction of dust particles with the electromagnetic field is needed. Three different regimes can be identified:

- In the limiting case in which the size of the particle is much smaller than the wavelength, the absorption dominates over the scattering and the extinction goes with λ^{-1}. The scattering term, although it is not dominant, is known as Rayleigh scattering, and it is proportional to λ^{-4}. However, the absorption depends on the dielectric function of the dust grain, so if these approximations are applied to the limit case of perfect insulators and conductors, it is found that the absorption goes with λ^{-2}.

- For the case in which the grain size is comparable to the wavelength, the treatment is more difficult. The most used approximation is the Mie theory (Mie 1908; Debye 1909), which describes the interaction of spherical particles with the electromagnetic field. The behavior of the extinction in this regime is very much dependent on the material and the phase of the electromagnetic wave with respect to the grain size at the moment of the interaction. One interesting result is that for grains in this regime the extinction efficiency, which is the ratio between the extinction cross section and the geometric cross section of the dust grain, tends to 2 at short wavelengths. This means that all the radiation that reaches the dust grain geometric cross section is either absorbed or scattered. At long wavelengths, however, the extinction efficiency is 0.

- Finally, in the case in which the grain size is much larger than the wavelength, i.e. the x-rays part of the spectrum, it is seen that the scattering creates a halo towards x-ray sources located behind dusty regions. The size of this halo depends on the dust grain size distribution, and therefore it gives insights on the interstellar dust sizes.

If one takes all of this into account, the extinction curve should show scattering at short wavelengths, significant extinction at wavelengths close to the particle size, and decrease at longer wavelengths. A general behavior is that the absorption is more important at long wavelengths, while scattering is predominant at short wavelengths.

As one can imagine, the extinction curve seen in our Galaxy (see Figure 1.2) therefore depends on the size distribution of dust grains, and this is the way it was found that interstellar dust grains should have sizes between 0.01 μm and $\sim$0.2 μm (Mathis et al. 1977).

Nevertheless, this does not explain what happens with the dust grain once it absorbs the energy from the photon that is absorbed or scattered. This question leads us to the next characteristic of dust grains: their emission.

1.2.2 Emission

The energy that grains gain when they absorb the interstellar radiation, mostly at the optical and ultraviolet frequencies, is re-emitted afterwards. There are two phenomena associated with the light emitted by dust grains: the photoluminescence, which produces a broad band in the optical; and the thermal emission, which produces continuum emission in the infrared (IR) and millimeter.

The energy of the photon excites an electron in the dust grain. Either the electron escapes from the grain if it gets enough energy (causing the charging of the grain), or decays rapidly emitting a photon whose energy is similar to the initial photon absorbed (producing the effect of photoluminescense), or it decays slowly transferring its energy to different vibrational modes of the grain (which produces the heating of the dust grain).

The third one is the most important and probable consequence. Thus, the result of the interaction of the radiation field with dust particles is that dust grains will heat up.

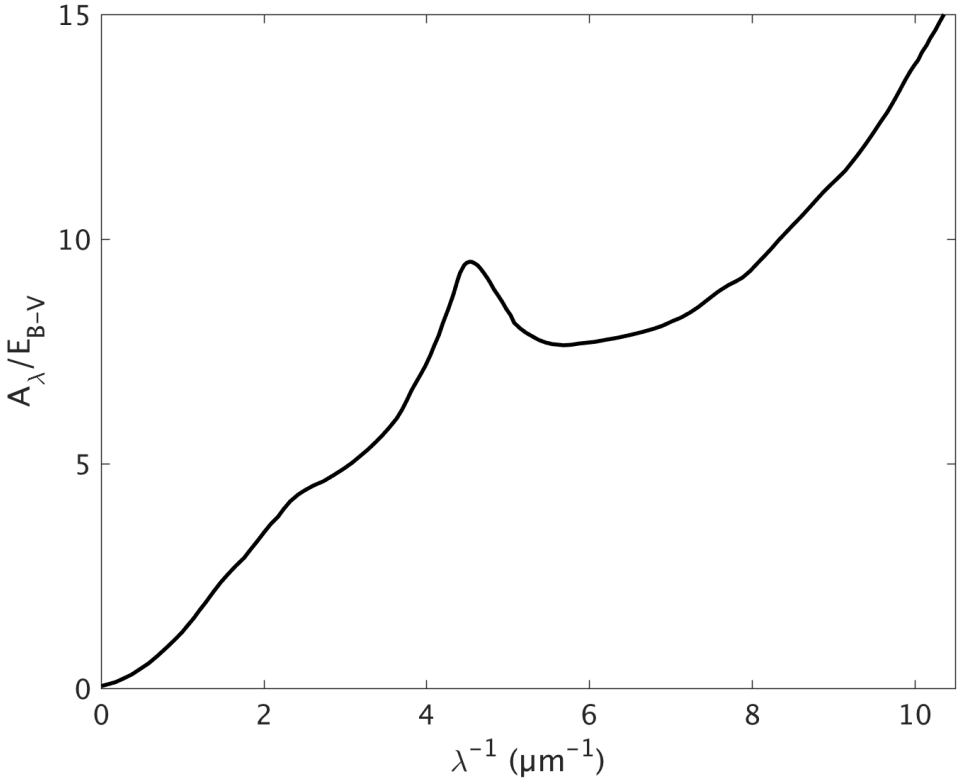

Figure 1.2: Normalized total extinction to the color excess, $E_{B-V} = A_B - A_V$, as a function of inverse wavelength. Here, V and B refer to the visual (∼550 nm) and blue (∼430 nm) part of the visible spectrum, respectively. This figure is based on Stahler & Palla (2005).

How much they are heated depends on the absorption capability of dust grains and the intensity of the interstellar radiation field.

Nevertheless, radiation field is not the only source of heating for dust grains. They can also gain temperature by cosmic rays, chemical reactions, and collisions, which can only play a role in shocks and dense clouds, where the radiation field is not strong enough to efficiently heat dust grains.

The energy that dust grains obtain is later re-emitted by thermal emission. The emission that we observe can be described by the radiative transfer equation:

$$I_\nu(\tau_\nu) = I_\nu(0)e^{-\tau_\nu} + \int_0^{\tau_\nu} S_\nu e^{-(\tau_\nu - \tau'_\nu)} \mathrm{d}\tau'_\nu, \tag{1.2}$$

where the term $I_\nu(0)e^{-\tau_\nu}$ describes the attenuation that the background source intensity, $I_\nu(0)$, is experiencing due to the material present along the line of sight, measured by the optical depth τ_ν, at the frequency ν. The second term represents the emission of the material along the line of sight. The source function, S_ν, can be described by the black body function if thermal emission is assumed, i.e.

$$S_\nu = B_\nu(T) = \frac{2h\nu^3}{c^2} \frac{1}{e^{\frac{h\nu}{kT}} - 1}, \tag{1.3}$$

where h is the Planck constant and c the speed of light.

If we now consider the case in which there is only a cold cloud and no strong emitting source in the background, which is the case for dense clouds observed at long wavelengths, and assuming that the cloud along the line of sight is isotropic, we obtain:

$$I_\nu(\tau_\nu) = S_\nu(1 - e^{-\tau_\nu}). \tag{1.4}$$

In the case of dense cores, the emission is optically thin, which means that $\tau_\nu \ll 1$, and this simplifies the emission of the cloud to:

$$I_\nu(\tau_\nu) = \tau_\nu B_\nu(T). \tag{1.5}$$

The optical depth, as seen in the previous section, depends on physical and chemical properties of the grain distribution present in the cloud. However, in astronomy the material which is present along the line of sight must be taken into account, and we therefore express it as:

$$\tau_\nu = \int \kappa_\nu \rho \mathrm{d}s, \tag{1.6}$$

s being the line of sight and κ_ν the dust opacity. κ_ν is a measurement of the dust absorption cross sections weighted by the mass of gas and dust, and also depends on the dust grain's physical and chemical properties. At millimeter wavelengths it has been observed that the opacity can be described by a power-law:

$$\kappa_\nu = \kappa_{\nu_0} \left(\frac{\nu}{\nu_0} \right)^\beta , \tag{1.7}$$

where β is called the spectral index and depends on the grain properties as well.

The density of the cloud can be described in terms of the number density of hydrogen molecules by $\rho = \mu_{\mathrm{H}_2} m_{\mathrm{H}} n_{\mathrm{H}_2}$. Therefore, integrating along the line of sight and considering κ_ν constant, we obtain:

$$\tau_\nu = \kappa_\nu \mu_{\mathrm{H}_2} m_{\mathrm{H}} \int n_{\mathrm{H}_2} \mathrm{d}s = \kappa_\nu \mu_{\mathrm{H}_2} m_{\mathrm{H}} N_{\mathrm{H}_2}, \tag{1.8}$$

where N_{H_2} is the molecular hydrogen column density, which is the measurement of the volume density along the line of sight.

This gives the emission of dust in cold clouds, which is described by:

$$I_\nu = \kappa_{\nu_0} \left(\frac{\nu}{\nu_0} \right)^\beta \mu_{\mathrm{H}_2} m_{\mathrm{H}} N_{\mathrm{H}_2} B_\nu(T). \tag{1.9}$$

For extended sources this equation is also usually expressed in terms of surface brightness, S_ν (not to be confused with the source function defined above), which is I_ν integrated over a solid angle. Equation (1.9) is widely used for determining dense clouds masses from the emission seen at millimeter wavelengths. However, this is usually done assuming certain dust grains properties, which is not appropriate if the dust grain distribution is variable. One example for this is a region dense enough to let dust grains coagulate and grow.

Nevertheless, the consequence of the emission of dust grains is that if the emission is efficient enough, dust grains will be thermalized. This means that all the energy absorbed by the dust grains coming from collisions or radiation will be efficiently released as thermal emission, and this has been shown to be the most efficient cooling mechanism in the ISM. However, this happens to be true only for grain sizes larger than $\sim$0.03 μm. For the very small grains, the rate at which they cool or emit is not high enough, and they therefore show temperature peaks or variations depending on the instantaneous energy absorbed. Moreover, when collisions are too energetic, as it happens in hot gas, for example, dust grains may not be able to redistribute or re-emit the energy gained fast enough, and they can thus suffer sputtering.

There are still other phenomena seen in the ISM which are the result of the presence and characteristics of dust grains. They will be briefly discussed in the following section.

1.2.3 Other phenomena related with dust grains

Polarization

Dust grains, although they are usually assumed to have spherical shape for simplicity, present a diversity of shapes. This produces polarized light, which can be due to either absorption, emission or scattering.

Let us consider an elongated dust grain interacting with electromagnetic waves. The major axis of the grain will absorb more light than the minor axis of the grain, because it has a larger cross sectional area. The result of this interaction is that the component of the electromagnetic wave parallel to the major axis will be more absorbed than the perpendicular one, and the light will be polarized. Therefore, in this case, we will receive the emission from the star polarized perpendicularly to the orientation of the dust grains. The opposite happens if we look at the wavelengths at which those same dust grains emit: they will mainly emit along the major axis. Therefore, as observers, we will see optical emission polarized in one direction, and infrared emission polarized in the perpendicular direction.

If dust grains are arbitrarily oriented in the cloud, all the light is absorbed. But, if the grains are aligned, then we will observe polarized light. Dust grains are commonly assumed to be aligned with the magnetic field. This process is initiated by the interaction with radiation fields. When dust grains are immersed in an anisotropic radiation field, radiative torques are imparted onto the dust grains that cause them to spin. Dust grains are paramagnetic and have a small electric charge. Therefore, the rotation of dust grains create a magnetic moment along the axis of rotation, which interacts with the surrounding magnetic field. This forces them to rotate with their long axis perpendicular to the magnetic field lines (Larmor precession). This mechanism was proposed by Lazarian & Hoang (2007) as being efficient for micron-size grains in the interstellar medium and tens of microns size grains in dense cores. Therefore, the study of polarized light gives information about the magnetic field and the distribution of dust grains.

Another way of starlight polarization is due to scattering. This effect is important in reflection nebulae (which are clouds that reflect the light from very bright nearby sources) and sources which are embedded in dense regions.

Chemical complexity and depletion of atoms and molecules

In very cold and dense regions, dust grains are surrounded by icy mantles. These mantles are formed of molecules which have depleted from the surrounding gas to the dust surface or formed onto the surface.

The first evidence suggesting that heavy elements are frozen on the dust grains was the fact that the abundances of these elements in our Solar System are systematically higher than the abundances observed in diffuse clouds.

Collisions between molecules and dust grains can produce the adsorption of these molecules on the grains' surfaces under the effect of van der Waals or electrostatic forces. Once a molecule is trapped, energetic collisions or an elevated temperature of the dust particle can provoke the desorption of the molecule, returning it to the gas phase. However, in dense and cold regions, the probability of low energetic (or velocity) collisions is higher, and the dust temperature is low enough to reduce the thermal desorption, resulting in the depletion of heavy elements (i.e. species heavier than helium).

This depletion has therefore two main results: the formation of ice mantles on dust grains, the activation of the corresponding grain surface chemistry, and the switch on of

other type of chemistry in the gas phase, whose reactions would not be favored otherwise.

One of the molecules most affected by depletion is carbon monoxide. CO in the gas phase hinders the formation of several molecules, such as H_2D^+, N_2H^+ or $HCO_2{}^+$, because it reacts easily with their progenitors. However, when CO disappears from the gas phase (i.e. it depletes onto dust grains), the abundances of these molecules increase strongly.

On the grain surfaces, atoms and molecules can travel through the surfaces by thermal hopping or quantum tunneling, finding each other and reacting, forming more complex molecules. In pre-stellar cores, where the temperature is around 10 K, these mechanisms are only efficient for H, D and H_2. However, the efficiency is so high that all hydrogen atoms are supposed to react. Thus, when molecules like CO are on the dust surfaces, more complex molecules like methanol (CH_3OH) can easily be formed.

Unfortunately, it is very difficult to observe the composition of the ices and only the most abundant components (in particular CO, H_2O and CO_2) can be detected (see e.g. Boogert et al. 2015). Moreover, these observations require the detection of background sources in the near infrared. This is particularly difficult to accomplish toward dense pre-stellar cores, where the visual extinction can reach values close to 100 magnitudes, extinguishing all the background radiation.

However, the abundances of gas phase species can be derived through spectral line observations with radio telescopes. Thus, if a molecule is solely formed on the dust surfaces and it does not desorb somehow and go to the gas phase after its formation, its detection may not be possible. Fortunately, there are some processes favoring the desorption of molecules, apart from the thermal and collisional desorption, which are not probable in quiescent and very cold regions. For example, when an exothermic reaction is taking place, the resulting energy could release the products of the reaction from the ice mantle. Also the impact of cosmic rays or secondary UV photons produced by cosmic rays upon impact with H_2 molecules (which are excited and fluoresce back, emitting UV photons) can help in desorbing these molecules.

Oxygen, carbon, iron, or magnesium, are some of the atoms which are more affected by depletion, while elements like nitrogen do not seem to be affected by it, although this is still a matter of study (see e.g. Caselli et al. 2017). For a schematic diagram showing how molecules and ice mantles are distributed in a pre-stellar core, see Figure 1.3.

Apart from the depletion, another effect that dust grains have on the chemical complexity in cold and dense environments is that they shield the region from radiation fields, which can destroy molecules by breaking chemical bonds. Therefore, dust grains protect the molecules formed in these environments.

Understanding the processes occurring in cold clouds requires the study of both gas and dust emission.

1.3 The study of gas

As already mentioned, 99% of the mass of molecular clouds is in the form of molecular gas, the main component being H_2. Molecules, as well as atoms, interact with the radiation

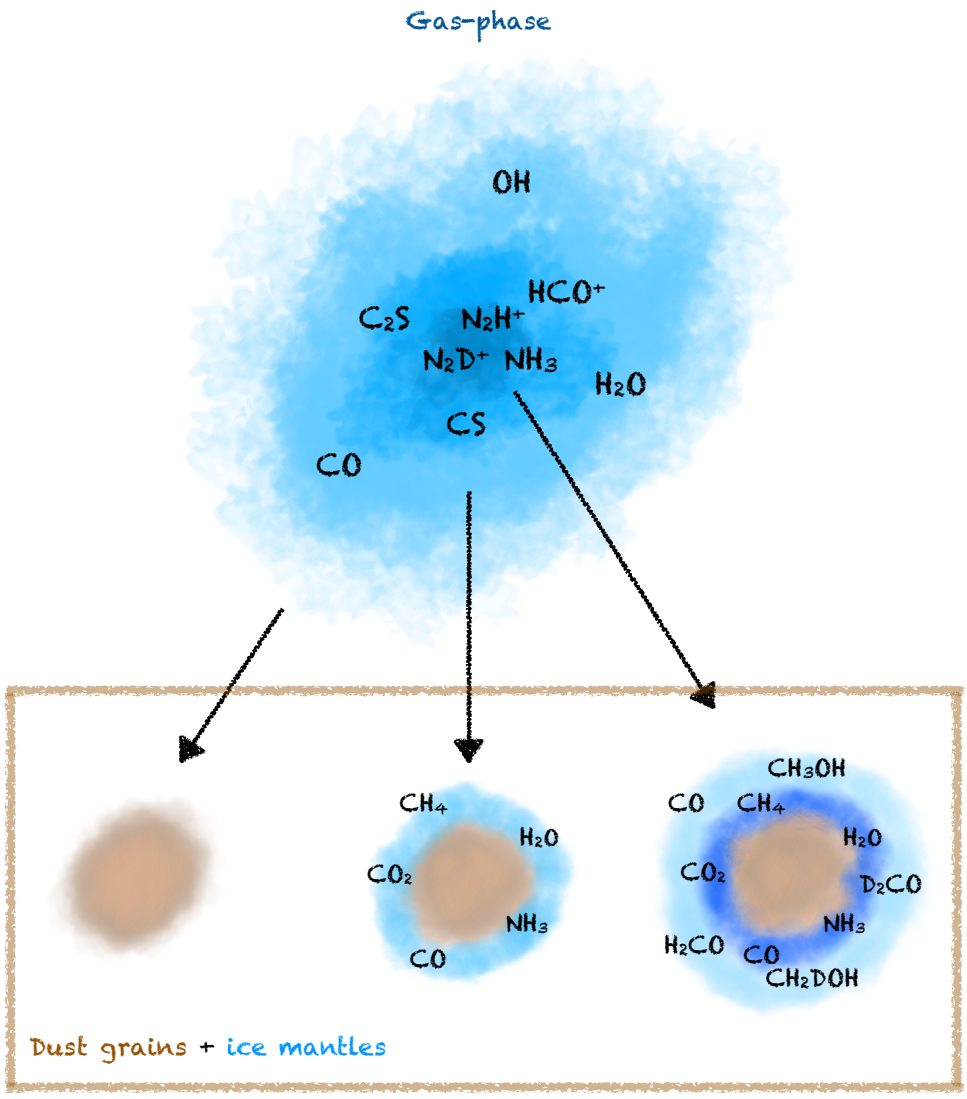

Figure 1.3: Diagram of some of the molecules that are seen in the different regions of a pre-stellar core, as well as how ice mantles on dust grains surfaces grow as molecules deplete onto them. This figure is based on Caselli & Ceccarelli (2012).

field, absorbing or emitting photons. This occurs through the excitation or de-excitation of the different energy levels of the molecules. Since the energy levels are discrete, only photons with certain frequencies (or energies) will be absorbed or emitted, producing what we know as the spectrum of a molecule, with a line for each jump between different energy levels. This spectrum is highly specific for each molecule because it strongly depends on its physical characteristics. Hence, the study of molecular spectral signatures in the ISM provides critical information on its chemical composition and physical and dynamical properties.

There are three energy domains that describe the spectrum of a molecule: rotational, vibrational, and electronic. The first one gives information about the geometry of the molecule, the second about the binding forces between the atoms conforming the molecule, and the third one describes the electronic configuration manifold. Each one dominates a different region of the spectrum, as the energies involved are different: the optical and UV are dominated by the transitions between different electronic states, the near-IR is dominated by the vibrational transitions, and the wavelength range from the far-IR to microwaves is dominated by rotational transitions. If the energy transmitted to the molecules is low (10^{-4}–10^{-1} eV), only the rotational transitions will show up, while if the energy is higher (0.1–1 eV), both the rotational and vibrational transitions can be activated. In very energetic regions (i.e. strong radiation field, >1 eV) also the electronic transitions will be seen together with the rotational and vibrational spectrum.

Thus, in very cold regions, molecules mainly emit via rotational transitions. However, there is still much information which can be retrieved from the rotational molecular lines, such as the density and temperature of the cloud, as well as the kinematic and chemical properties.

1.3.1 Relation between line intensity and molecular density

The emission or absorption of photons by an atom or molecule can occur through three different types of processes: spontaneous emission, stimulated absorption or stimulated emission. The transition probabilities are described by the Einstein coefficients. While the spontaneous emission does not, the stimulated emission and absorption depend on the radiation field, i.e. on the density of photons with the exact frequency needed to activate the energy jump.

Considering the transition between two energy levels of a molecule, 1 being the lower energy level and 2 the higher energy level, A_{21} is defined as the probability for spontaneous emission per unit time, B_{21} the probability of stimulated emission per unit time, and B_{12} the probability of stimulated absorption emission per unit time (the sub-indexes indicate the direction in which the transition is produced).

Now let's consider a set of these molecules and assume thermodynamic equilibrium. The process of populating level 2 depends on B_{12} according to:

$$\frac{\mathrm{d}n_2}{\mathrm{d}t} = n_1 B_{12} u_\nu, \tag{1.10}$$

for a frequency $\nu = \frac{E_2 - E_1}{h}$, and n_1 being the population of molecules in level 1 (or energy E_1). As seen, the stimulated absorption depends on the radiation energy density per unit frequency, expressed as u_ν. u_ν can be described in terms of intensity following $u_\nu \equiv \frac{1}{c}\int I_\nu \mathrm{d}\Omega$, Ω being the solid angle. Similarly, the depopulation of level 2 (or population of level 1) occurs in the following way:

$$\frac{\mathrm{d}n_1}{\mathrm{d}t} = n_2(A_{21} + B_{21}u_\nu). \tag{1.11}$$

Note that this process can proceed via spontaneous emission or stimulated emission. Therefore, the population in level 2 is described by the gain and loss of photons through both processes:

$$\frac{\mathrm{d}n_2}{\mathrm{d}t} = n_1 B_{12} u_\nu - n_2(A_{21} + B_{21}u_\nu). \tag{1.12}$$

In thermal equilibrium, the radiation field can be described by the emission of a blackbody, $B_\nu(T)$ (see Equation (1.3)), which is isotropic, so the radiation energy density per unit frequency can be described by:

$$u_\nu = \frac{4\pi}{c} B_\nu(T). \tag{1.13}$$

Other consequences of thermal equilibrium is that $\mathrm{d}n_i/\mathrm{d}t = 0$ and that Boltzmann's statistics can be applied, following:

$$n_2 = \frac{g_2}{g_1} n_1 e^{-(E_2 - E_1)/kT}, \tag{1.14}$$

where g_1 and g_2 are the degeneracy of the energy levels.

Thus, from Equations (1.12), (1.13) and (1.14), and considering $\mathrm{d}n_i/\mathrm{d}t = 0$, the Einstein coefficients follow:

$$B_{21} = \frac{c^3}{8\pi h \nu^3} A_{21}, \tag{1.15}$$

and

$$B_{12} = \frac{g_2}{g_1} B_{21}. \tag{1.16}$$

The Einstein coefficients are constants, so this shows that all these processes can in reality be described only by one the coefficients (here A_{21}). It can also be seen that for high frequencies the spontaneous emission dominates, whereas the stimulated emission becomes important at low frequencies.

As already mentioned, cold clouds mainly emit at low frequencies, more affected by the stimulated emission. Thus, going back to Equation (1.12), one can see that the radiation is going to be affected by the stimulated absorption and emission by a factor of

$$\alpha_{21} = n_1 B_{12} - n_2 B_{21} = \frac{c^3}{8\pi h\nu^3} n_2 A_{21}(e^{h\nu/kT} - 1), \tag{1.17}$$

where α_{21} is called absorption coefficient. This absorption coefficient determines the optical depth seen at the molecular transition frequencies.

Moreover, we can relate this absorption coefficient with the total gas density of the cloud. The Boltzmann equation has a general case which relates the number density of molecules in a determined energy level with the complete distribution of molecular levels:

$$n_2 = \frac{g_2}{Q(T)} n e^{-E_2/kT}, \tag{1.18}$$

where $Q(T)$ is the partition function of the molecule, which is a sum over all the states of a molecule, and n the total number density of molecules. Therefore, the absorption coefficient is directly related with the number density of molecules, which means that the intensity of a line is directly proportional to the density of the cloud.

It has to be taken into account that in these equations there is an effect that has been avoided for simplicity: Heisenberg's uncertainty principle. This principle implies that the probability of transition between two levels has an uncertainty associated with that of the energy of the levels. This would imply that u_ν would be written as $u_\nu \phi_\nu$, being ϕ_ν the line profile, which can be approximated by $\phi_\nu \sim 1/\Delta\nu$.

Another approximation made is to consider level population changes via radiation effects only, while in regimes where the density is high enough these processes can also proceed via collisions.

1.3.2 Absorption or emission, what is observed?

In the previous section it is shown that the absorption or radiation can also be due to molecules, and that this affects the optical depth in Equation (1.2), which therefore can be highly increased at certain frequencies.

However, the question regarding whether a dark cloud would show molecular emission or absorption is still not answered. Assuming an optically thin cloud with a star behind it, Equation (1.2) would be written as follows:

$$I_\nu = I_\nu(0) + \tau_\nu(S_\nu - I_\nu(0)). \tag{1.19}$$

This equation tells us that if the emission from the star, $I_\nu(0)$, is more intense than that of the cloud, S_ν, the light from the star is absorbed at those resonance frequencies of the molecules, i.e. we observe absorption lines. However, if the light of the star is less intense than the medium, we see emission lines form the cloud.

If there is a dense cold cloud, which absorbs all the light from behind, the second case holds. However, due to this high absorption, the source of emission in dense clouds cannot arise from the interaction of molecules with the radiation field. Nevertheless, due to the

high density of H_2 molecules, the collisions are frequent, and thus provide an efficient mean to excite the molecules.

If the rate of collision is not high enough, i.e. the density is low, the energy would be dissipated through line emission and the system would cool down to the radiation temperature of the background emission. On the other hand, if collisions are frequent, the system can enter into a stable regime in which the excitation temperature of the molecule (which corresponds to the temperature used in the equations of the previous section) equals the kinetic temperature of the gas (which makes possible the use of Boltzmann equations). This is the so-called Local Thermodynamic Equilibrium (LTE).

1.3.3 Kinematics

There are two features associated with the line emission which give important information regarding the kinematics of the clouds: the centroid velocity and the line width.

The first one refers to the velocity at which the object moves with respect to us. This modifies the frequency at which the line is observed, due to the Doppler effect. However, different parts of the cloud can move differently, which can be the case, for example, of a rotating cloud. In this case, the centroid velocity will be redshifted in the regions which move away from us, and blueshifted in the regions which are moving towards us. Other examples of mechanisms that can modify the centroid velocity we see in different parts of the clouds are cloud collisions, infall in contracting clouds, or jets driven by young protostars.

The Doppler effect also affects the line width, due to the spread of centroid velocities that are observed along the line of sight. If there are other physical mechanisms, such as turbulence, expansion or infall, the line widths can be also affected.

Therefore, the study of line emission not only gives us information regarding the chemical composition, density and temperature, but also informs us about the physical processes and dynamical properties of a cloud.

1.3.4 Astrochemistry

The study of molecular emission gave rise to a new field in astrophysics: astrochemistry. As it has been shown, the chemistry and physics of the ISM are completely connected and cannot be understood separately.

While light elements such as hydrogen, deuterium, helium and lithium were formed in the early Universe after the Big Bang, heavier elements had to wait for the formation of successive generation of stars to form. Active chemistry then started to take place in the interstellar and circumstellar media.

The formation of molecules

The different kinds of chemistry found in the different phases of the ISM can be understood in terms of the radiation field and density. The lower the density, the more the radiation

field can penetrate a region, dissociating the molecules or exciting the atoms; conversely, the denser the region, the more shielded it is against the radiation field, allowing the recombination of the atoms and the formation of molecules.

But even if the environment is shielded from the radiation field, the formation of a molecule is not straightforward. Its formation must start with the collision of its parent molecules/atoms. However, their collision and union without any external agent would imply the formation of an excited molecule, which contains the energy of the collision. This energy can be lost either by colliding with a third body, or by radiating a photon. The former requires very high densities which are not present in cold clouds, while the latter is not probable enough.

It seems easier then to consider the collision of two reactants forming more than one simple product, as in this case the energy from the collision would be divided into various molecules. However, if we consider two neutral species as reactants, this process would imply the initial breaking and the following formation of molecular bonds, and an extra energy in excess of 1 000 K (for typical bond energies of 0.1–1 eV) would be needed for that. This is not possible in cold cores, where temperatures are very low ($\sim$10 K). However, this energy wall is decreased when one of the reactants is an ion. In this case, an instantaneous charge separation is generated (polarization) in the neutral species, which creates an attraction between the ion and the neutral, allowing the reaction even in low temperature environments (Herbst & Klemperer 1973).

All of this poses another question on the table: if neutral-neutral reactions and the direct union of two atoms are two processes very unlikely to happen on cold environments, how does H_2, the most abundant molecule in these regions, form? To answer this question one has to go back to the role of dust grains in chemistry. As already mentioned, there is a probability for dust grains to trap atoms on their surfaces. H atoms, as they are quite light, can move around easily through quantum tunneling and find each other, forming H_2 molecules (Gould & Salpeter 1963; Hollenbach & Salpeter 1970). In this process, the dust grain serves as a third body that absorbs the exceeding energy, which is rapidly diffused. The H_2 molecule can then desorb and go back to the gas phase. Many molecules go through this process, and depending on the desorption, formation and depletion rates, we observe them on the gas phase or they remain frozen on the dust grains.

Deuteration

The different abundances of the different elements in space is a very debated question in astrochemistry and cosmology. After the Big Bang, there was a short period of time in which the Universe was a hot soup where free neutrons could combine with protons creating light elements. This period of time was very short due to the fast expansion and cooling of the Universe, and therefore only hydrogen, helium, deuterium, and lithium could be formed. The rest of the elements present in the Universe nowadays has been formed afterwards. In this section we focus on deuterium, D, which is an element whose abundance mainly comes from that early Universe.

The fraction of D atoms with respect to H atoms in the early Universe is 3×10^{-5},

while in the ocean water in the Earth, this fraction goes up to 1.5×10^{-4}, a factor of 10 higher than the nearby cosmic value (Linsky et al. 2006). Similar ratios to that found on Earth are found in Solar bodies, such as comets and carbonaceous chondrites (Caselli & Ceccarelli 2012, and references therein). These objects are thought to be fossils of the primordial Solar System, and thus their chemical properties are linked to that of the early stages of its formation. Therefore, the study of the evolution of the D/H ratio throughout the Universe History and, in particular, the evolution of this ratio through the different stages of the star formation process is needed to shed light on the observed D enrichment.

One particular case concerns molecular clouds, where it has been found that the D/H ratio in some molecules increases to values of 0.01-0.1. However, the majority of deuterium is in the form of HD, and the abundance of HD with respect to H_2 has been measured to be close to the cosmic value. Therefore, there must be a way in which the rest of molecules are being deuterated in molecular clouds. The most important reaction involving deuterium in cold environments is:

$$H_3^+ + HD \rightarrow H_2D^+ + H_2 + 230K.$$

This reaction is exothermic, and in really cold environments cannot proceed backwards. However, it competes with:

$$H_3^+ + CO \rightarrow HCO^+ + H_2,$$

which is much more efficient than the previous one because of the high abundance of CO. Moreover, CO also helps in the destruction of H_2D^+, forming HCO^+ and HD. Therefore, CO prevents the deuteration of other molecules more complex than HD.

However, as previously seen, CO freezes out onto the dust grains in dense cores, allowing the activation of a series of reactions which permit the presence of deuterium in many forms, and therefore increasing the D/H ratio.

Deuteration is also expected to happen on dust grains. In this context D atoms would move on the grain surfaces in a similar way than H atoms, although slower due to their higher masses, and react with other species forming deuterated molecules.

The evolution of the D/H fractionation from here to more evolved objects is a matter of debate. However, seeing large D/H values in cold environments tells us that somehow a higher D/H ratio than that of the cosmic value can be maintained through the evolution of a Solar-like system.

Not only does the hydrogen-deuterium isotope pair show this kind of behavior, but other elements also show important isotopic variance in different environments and materials. Nitrogen is one of the most striking examples of highly variable isotopic composition (^{15}N fractionation). This shows that a large variety of chemical fractionation processes took place during the formation of our Sun and our Earth.

1.4 Our laboratory: the pre-stellar core L1544

Judging from what is said in previous sections, it seems necessary to study both gas and dust, as they are related in many ways. For example, the presence of both is important to understand the collapse of a dense core into a protostar, as they are needed to transform the gravitational energy into radiation, cooling down the system and maintaining a low Jeans mass. Also, the chemistry present in a cloud cannot be understood without studying dust surface chemistry.

Unfortunately, in astrophysics there is no possibility of playing with different parameters and checking what the results are, like in a laboratory. Therefore, what is typically done is to select different objects in the sky with well-defined characteristics that can help us to understand the different evolutionary stages of any process, and try to see the connection between the physics and the chemistry, until we are able to better understand our Universe.

In the process of searching for a candidate for studying the earliest phase of low-mass star formation, L1544 appeared. L1544 is a pre-stellar core placed in the Taurus Molecular Cloud at a distance of 140 pc from us. Named by the Lynds' dark nebulae catalogue (Lynds 1962), it is placed in an isolated region of the molecular cloud, which avoids the influence from energetic sources, such as protostellar or stellar winds or strong UV field.

The 1.3 mm emission of L1544 was observed by Ward-Thompson et al. (1999), revealing an elongated and bright core. Follow-up studies have determined that its central volume density is over 10^6 cm^{-3} (Tafalla et al. 2002; Crapsi et al. 2007; Keto & Caselli 2010) and its temperature drops down to ~ 6 K (Crapsi et al. 2007) in the center. These kind of objects seem to have very short lifetimes, of about few times 10^4 years when their density is above 10^6 cm^{-3} (Könyves et al. 2015). This makes very dense pre-stellar cores, like L1544, very rare and difficult to observe, as they soon create a central object and stop being starless.

Inward motions were detected and studied by Tafalla et al. (1998) and Caselli et al. (2002a), and it was the first pre-stellar core in which water was detected (Caselli et al. 2012). The water line observed also showed an inverse P-Cygni profile, which arises from gravitational contraction.

Moreover, high deuterium fractions have been measured toward this source; for example, $[N_2D^+]/[N_2H^+] = 0.2$, $[DCO^+]/[HCO^+]$=0.04 and [c-C_3HD]/[c-C_3H_2] =0.12-0.17 (Caselli et al. 2002b; Spezzano et al. 2013). L1544 also shows a depletion factor of CO of $\sim$10, averaged along the line of sight, which means that the abundance of CO with respect that of the ISM is 10 times lower toward the center of the core (Caselli et al. 1999). Also complex organic molecules (COMs; in astronomy COMs are molecules with at least 6 atoms in size Herbst & van Dishoeck 2009) such as CH_3OH have been observed, which indicates that grain surface chemistry is efficient (as CH_3OH cannot efficiently form in the gas phase).

This makes L1544 the perfect laboratory to test what happens in the very early stages of star formation, just before a protostar is formed.

1.5 Radioastronomy

The best wavelength range to study all the observables mentioned previously, dust and molecules in very cold regions, is the radio. Therefore, radioastronomy is briefly described next.

Going from 0.3 mm to 10-15 mm, the radio spectral window was first detected by Karl G. Jansky, who found Galactic synchrotron emission in the 30s. However, radio detectors were first widely used and improved for military RADAR applications during the 20^{th} century. During this time, unknown signals from space were received, which caught the attention of scientists. Once the war was over, the era of radioastronomy began.

The instrument used for capturing these low frequency photons are radio antennas or radio telescopes (see Figure 1.4). They are characterized by having parabolic reflective dishes that collect all the radiation into a second mirror, which then redirects it to the detector. However, when the light is received by the telescope, it suffers from diffraction, described by the Fraunhofer diffraction. This limits the angular resolution of the telescope, which is known as main beam size, and it depends on the diameter of the main reflector and the wavelength observed. Moreover, the edges of the antenna will cause what we call secondary side lobes, which correspond to deviances on the refractory pattern.

The telescope has a certain efficiency in collecting the light (called aperture efficiency), which can be measured observing sources whose emission flux is known; and another efficiency in collecting that light via the main beam (called main beam efficiency). The latter is important for extended sources whose emission fill both the main beam and the side lobes.

The collected emission has two more sources of error: the emission arising from the atmosphere and the noise created by the electronics of the own instrument. However, the second one can be measured easily, and the first one can be corrected in different ways: for example, observing sources of known emission, i.e. calibrators, or filtering what is expected to be atmosphere emission.

Among the present radio facilities are the IRAM 30 m telescope in Granada, the Green Bank Observatory (GBO) in West Virginia, the James Clerk Maxwell Telescope (JCMT) in Mauna Kea, the Large Millimeter Telescope Alfonso Serrano (LMT) in Sierra Negra, and the Atacama Pathfinder EXperiment (APEX) in Llano de Chajnantor. Among the powerful radio interferometers are Karl G. Jansky Very Large Array (VLA) in Socorro, NOrthern Extended Millimeter Array (NOEMA) in Plateau de Bure, and the current most important and powerful telescope in radioastronomy, the Atacama Large Millimeter/Submillimeter Array (ALMA), in Chajnantor. This thesis only uses data from single dish telescopes.

1.6 Thesis overview

This thesis is focused on the study of the dust properties in the pre-stellar core L1544, together with observations of a deuterated species known to be formed on dust grain surfaces, CH_2DOH (or deuterated methanol).

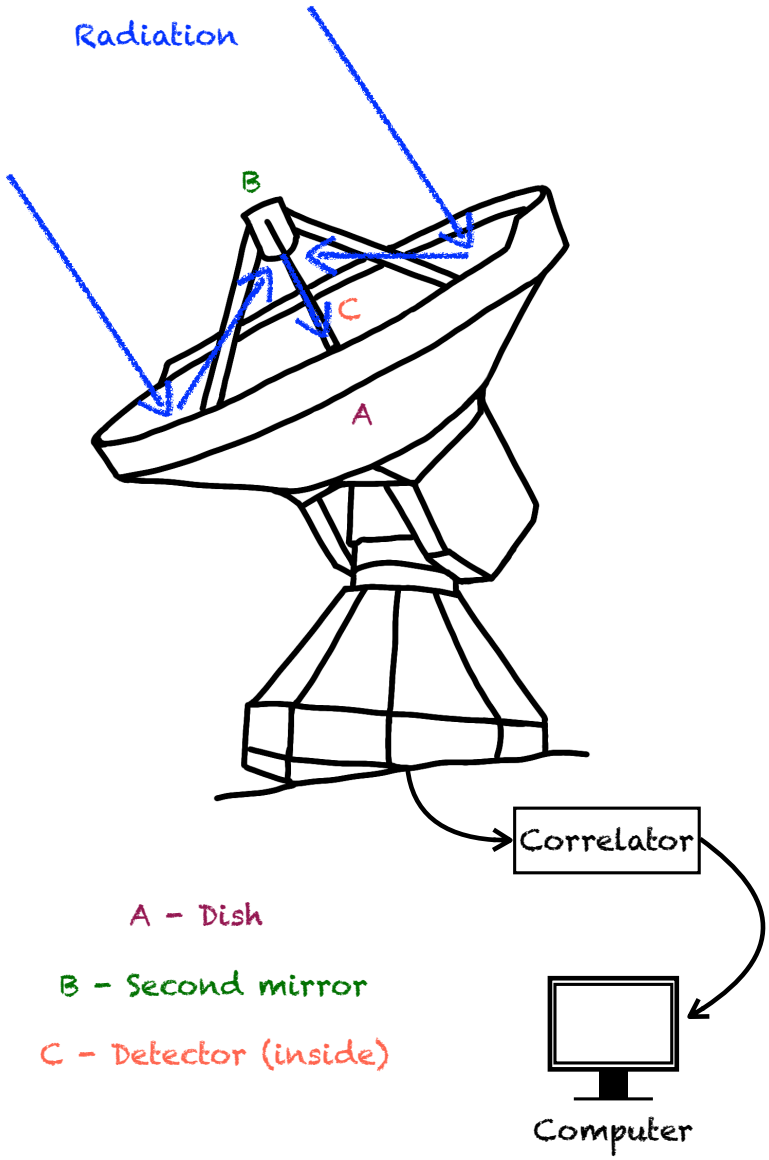

Figure 1.4: Artistic view of a photo taken at the IRAM 30 m telescope. The blue arrows show the path that the interstellar radiation follows, the labels indicate the main parts of the antenna, and the black arrows show the path that the detected signals follow. The information received by the detector is sent to the correlator, which transforms the detector signal to spectral signal. This spectral signal is then saved in a computer.

In **Chapter 2** I present the study of the dust emission in L1544 using two new millimeter continuum maps at 1.2 and 2 mm, obtained with the 30 m IRAM telescope, and a comparison with model predictions. To determine if there is grain growth in L1544, I focus on the search of dust opacity variations from the outskirts to the center, as this would indicate that the grain distribution changes. However, I will show that from these maps, there is no indication of dust coagulation or grain growth, and that a simple model predicts that only interferometers can see dust opacity variations.

Chapter 3 is focused on deuterated methanol in L1544 and the comparison of the emission of this molecule with CO, H_2CO and deuterated isotopologues of H_2CO. As seen in the Introduction, the presence of CO on dust grains activates chemical reactions which are important for the formation of more complex molecules, and this is also the case for methanol and deuterated methanol. I show that deuterated methanol emission is consistent with the idea of it being formed onto the dust grains, and released to the gas phase in the same way as methanol. Moreover, a comparison with two chemical models shows that effects like quantum tunneling and reactive desorption are important.

In **Chapter 4**, the first 3.3 mm continuum map of L1544 observed with the GBO will be presented, together with a new 1.1 mm map observed at the LMT. These maps give new insights into the dust properties in L1544 and its physical structure, as they clearly indicate that a change in opacity is mandatory to reproduce the observed maps.

Finally, I summarize the conclusions of my work in **Chapter 5**, and discuss about future prospects and activities.

1.6.1 Collaborations

Apart from the work done for my thesis, during my PhD I have participated in other projects:

Seeds Of Life In Space (SOLIS)

SOLIS is a NOEMA large program aimed at understanding organic chemistry in space and its evolution observing 7 different sources in different evolutionary stages in the process of star formation. I have participated actively in the data reduction and processing of the observations done toward L1544.

Within this project, I participated as co-author in the following publications:
Punanova, A., Caselli, P., Feng, S., et al. 2018, ApJ, 855, 112
Ceccarelli, C., Caselli, P., Fontani, F., et al. 2017, ApJ, 850, 176
Codella, C., Ceccarelli, C., Caselli, P., et al. 2017, A&A, 605, L3
Fontani, F., Ceccarelli, C., Favre, C., et al. 2017, A&A, 605, A57

Green Bank Ammonia Survey (GAS)

GAS is a large program at the GBO, focused on the observation of the NH_3 emission from all Gould Belt star-forming regions in the northern hemisphere. I have participated in this project as an observer, and as a co-author in the following publications:
Redaelli, E., Alves, F. O., Caselli, P., et al. 2017, ApJ, 850, 202
Keown, J., Di Francesco, J., Kirk, H., et al. 2017, ApJ, 850, 3
Kirk, H., Friesen, R. K., Pineda, J. E., et al. 2017, ApJ, 846, 144
Friesen, R. K., Pineda, J. E., co-PIs, et al. 2017, ApJ, 843, 63

1.7 Bibliography

This Introduction has been based on many books, courses, and reviews:

- The description of the process of low mass star formation has been based on Stahler & Palla (2005), *Star and Planet formation course* by A. Sicilia-Aguilar at the Universidad Autónoma de Madrid, *Astrochemistry and Star/Planet Formation* IMPRS advanced course by Prof. P. Caselli.

- The section *The study of the interstellar dust* was based on Draine (2011), Wickramasinghe & Hoyle (1991), which I recommend for a brief historic review of how interstellar dust was discovered, Latusseck (2008), Kauffmann et al. (2008), Tielens (2005), and Caselli & Ceccarelli (2012).

- The section *The study of gas* is based on notes from the course *Atomic and Molecuar Physics* by Prof. F. J. López Domínguez in the Universidad Autónoma de Madrid, *Radiative transfer* course by Prof. C. Eiroa at the Universidad Autónoma de Madrid, Böhm-Vitense (1992), Yamamoto (2017), Caselli & Ceccarelli (2012), LeBlanc (2010), and Draine (2011).

- The brief description of Radioastronomy was based on Yamamoto (2017) and Rohlfs & Wilson (2004).

Chapter 2

Search for grain growth towards the center of L1544

This Chapter is based on: Chacón-Tanarro, A., Caselli, P., Bizzocchi, L., Pineda, J. E., Harju, J., Spaans, M., and Désert, F.-X. 2017, A&A, 606, A142

2.1 Abstract

In dense and cold molecular clouds dust grains are surrounded by thick icy mantles. It is not clear, however, if dust growth and coagulation take place before the protostar switches on. This is an important issue as the presence of large grains may affect the chemical structure of dense cloud cores, including the dynamically important ionization fraction and the future evolution of solids in protoplanetary disks. To study this further, we focus on L1544 – one of the most centrally concentrated pre-stellar cores on the verge of star formation – which has a well-known physical structure. We observed L1544 at 1.2 and 2 mm using NIKA, a new receiver at the IRAM 30 m telescope, and we used data from the *Herschel* Space Observatory archive. We find no evidence of grain growth towards the center of L1544 at the available angular resolution. Therefore, we conclude that single-dish observations do not allow us to investigate grain growth towards the pre-stellar core L1544 and high-sensitivity interferometer observations are needed. We predict that dust grains can grow to 200 μm in size towards the central $\sim$300 au of L1544. This implies a dust opacity change of a factor of $\sim$2.5 at 1.2 mm, which can be detected using the Atacama Large Millimeter and submillimeter Array (ALMA) at different wavelengths and with an angular resolution of $2''$.

2.2 Introduction

Pre-stellar cores are self-gravitating starless dense cores with clear signs of contraction motions and chemical evolution (Crapsi et al. 2005). They are formed within molecular clouds, due to the influence of gravity, magnetic fields, and turbulence. They are thought

to be on the verge of star formation, and therefore represent the initial conditions in the process of star formation (Bergin & Tafalla 2007; Caselli & Ceccarelli 2012). These systems are characterized by high densities ($n_{\mathrm{H_2}} > 10^5\,\mathrm{cm^{-3}}$) and low temperatures ($T < 10\,\mathrm{K}$) towards their central regions (Crapsi et al. 2007).

In dense and cold molecular clouds dust grains are surrounded by thick icy mantles (e.g., Boogert et al. 2015, and references therein). It is not clear, however, if dust growth and coagulation take place before a protostar is born. This is an important issue as dust coagulation may affect the formation and evolution of protoplanetary disks forming from molecular clouds (Zhao et al. 2016). Foster et al. (2013) find a strong correlation between the visual extinction and the slope of the extinction law towards the Perseus molecular cloud. This can be interpreted as grain growth, but it is not clear if grain coagulation is needed or if the growth of icy mantle can explain the observed correlation. Large grains are also detected in young protoplanetary disks, again suggesting that grain growth may already be at work in the earlier dense core phases (Testi et al. 2014). There is evidence of large (micrometer-sized) grains through the observed extended emission at 3.6 μm in dense cloud cores (known as the coreshine effect; Pagani et al. 2010), but this interpretation has been questioned by Jones et al. (2013), who suggested that amorphous hydrocarbon material could actually produce the observed coreshine without the need of large grains. Moreover, Andersen et al. (2014) found a similar threshold for the coreshine and water ice, with the scattering efficiency at 3.6 μm increasing with the increase in the water-ice abundance, suggesting that water ice mantle growth in dense clouds may be at least partially responsible for the coreshine effect. However, recent findings by Lefèvre et al. (2016) show that the mid-infrared scattering phenomenon is still present at 8 μm and that grains proposed in Foster et al. (2013) would fail to explain scattering at such a long wavelength, as would the uncoagulated ice covered grains advocated by Andersen et al. (2014).

The study of the dust emission at long wavelengths sensitive to the larger grains is therefore important in order to gain a better understanding of the grain size distribution in the early phases of star formation. This emission depends on dust grain properties such as structure, size, and composition. Here we focus on the dust opacity and the spectral index, two parameters that depend directly on the grain size distribution.

The opacity, κ_ν, is a measurement of the dust absorption cross sections weighted by the mass of the gas and dust. As explained by Kruegel & Siebenmorgen (1994), when dust grains are small compared to the wavelength (the so-called Rayleigh limit), the mass absorption coefficient does not depend on the grain size, but only on the mass; when the grain size is much larger than the wavelength, the absorption coefficient depends inversely on the grain size; and when $a \sim \lambda$ (a being the grain radius), the mass absorption coefficient can increase up to 10 times its value because at these wavelengths dust grains are better radiators (Kruegel & Siebenmorgen 1994). When dust grains are coated by ices, their cross section increases and, consequently, so does κ_ν. This same trend is seen with fluffy dust grains (Kruegel & Siebenmorgen 1994; Ossenkopf & Henning 1994). Therefore, variations in the value of κ_ν along the spectrum can be a strong indicator of grain growth.

The dust opacity can be approximated by a power law at millimeter wavelengths,

$\kappa_\nu \sim \nu^\beta$, where β is the emissivity spectral index (Hildebrand 1983). For β, a more complex analysis is needed. Typical values found in the interstellar medium (ISM) at far-infrared and submillimeter wavelengths lie in the range 1.5-2. In presence of large grains, which increase the dust opacity at longer wavelengths, β can decrease to values close to or below 1 (Ossenkopf & Henning 1994; Draine 2006). When the minimum size of the distribution is lower than 1 μm, β is only affected by the largest grains and not by the smaller grains (Miyake & Nakagawa 1993; Draine 2006).

Laboratory measurements of the opacity and the spectral index at millimeter wavelengths found a dependence of the mass absorption on temperature for different grain compositions (Agladze et al. 1996; Mennella et al. 1998; Boudet et al. 2005; Coupeaud et al. 2011; Demyk et al. 2013). Agladze et al. (1996) found two different behaviors depending on the temperature range: for very low temperatures (1.2 - 20 K) the millimeter opacity decreases with increasing temperature, while for temperatures between 20 and 30 K it increases or is constant with temperature. This trend is the opposite for β. However, at mm-wavelengths the measured changes are not significant (within 20%) when the temperature is varied between 6 and 10 K, which is the temperature range relevant to the central regions of pre-stellar cores. Boudet et al. (2005) and Coupeaud et al. (2011) found similar results for amorphous material, as they observed an increase in the spectral index (decrease in the opacity) while decreasing the temperature (for $T > 10$ K). However, when they let the material crystallize, no temperature dependence was detected. Additionally, they also reported a frequency dependence on the opacity and the spectral index. Another interesting result was found by Demyk et al. (2013), who showed two extreme and completely different results depending on the material analyzed for temperatures ranging from 10 K to 300 K. For wavelengths longer than 500 μm, the spectral index value could take values higher than 2.5 and lower than 1.5 depending on the composition of the sample, which in their case depends on the oxidation state of the iron. This means that the increase in the opacity in the studied temperature range is more important at longer wavelengths. What Demyk et al. (2013) conclude is that the emission from dust cannot be described by only one power-law spectrum, but should be characterized by different spectral indexes at different wavelengths.

There are several astronomical studies constraining the value of β in protoplanetary disks, where it is known that dust coagulation takes place, giving birth to future planets. Natta & Testi (2004) found that despite the composition dependence and grain distribution shape, dust grains of 1 mm in size lead to β values lower than 1. For earlier stages in the process of star formation, Schnee et al. (2014) found low values for the spectral index towards OMC 2/3 with a low anticorrelation between β and temperature, which may indicate the presence of grains from millimeter size up to centimeter size. However, this was subject of further study by Sadavoy et al. (2016), who found higher values of the spectral index and suggested that the observations from Schnee et al. (2014) were contaminated or deviated from a single power law. After studying extinction maps, Forbrich et al. (2015) found that while a single spectral index can reproduce their observational data, the opacity increases towards the center of the starless core FeSt 1-457, possibly indicating grain growth. At larger scales, using *Planck* and *Herschel* results, Juvela et al. (2015a,b) observed

that the opacity increases with density and that there is an anticorrelation between the spectral index and the temperature.

Obtaining a value of the spectral index at early stages of star formation is a difficult task due to the known degeneracy between the spectral index and temperature, which appears when the spectral energy distribution of the dust emission is fitted using a least-squares method to obtain the temperature, density, opacity, and spectral index of the observed object (Shetty et al. 2009a,b). Moreover, it has also been proved that uncertainties in the measured fluxes, and an incorrect assumption of isothermality and the noise itself, can mimic the observed anticorrelation between the temperature and the spectral index of the dust (Shetty et al. 2009a,b).

Therefore, taking into account these studies and previous results on the spectral index, it is not clear what to expect from observations towards the dense and cold pre-stellar cores. Nevertheless, any variation in the κ_ν and/or β across a cloud core, from the outskirts to the center, would indicate grain growth. Köhler et al. (2015) show that dust evolution in dense clouds produces significant variations (factors of a few) in the opacity, while the spectral index changes by less than 30%, so that κ_ν variations should be easier to measure. Moreover, if the physical structure of the cloud is known, it is possible to directly measure the variation in the opacity across a core at millimeter wavelengths, while for the spectral index a multiwavelength study is needed.

In this work we focus on L1544, a well-known pre-stellar core in the Taurus Molecular Cloud at a distance of 140 pc. The zone within the central 1000 au is still unexplored, but we know that the temperature drops down to 7 K towards the central 2000 au (Crapsi et al. 2007) and it shows clear signs of contraction (Caselli et al. 2012). Detailed modeling of L1544 (Keto & Caselli 2010) found that an increase in the dust opacity is needed to reproduce the drop in the measured temperature towards the central 2000 au. This could be an indication of fluffy grains in the core center (Ossenkopf & Henning 1994; Ormel et al. 2009) where CO is heavily frozen (Caselli et al. 1999) and volume densities become larger than 10^6 cm^{-3}. The presence of fluffy grains can only be verified by multiwavelength millimeter observations. The well-known physical structure of L1544, with its high volume densities and centrally concentrated structure, makes this object the ideal target to study possible variation in the opacity. For this, we used the continuum emission at 1.2 mm and 2 mm from the IRAM 30 m telescope with an angular resolution of 12.5″and 18.5″, respectively (at 140 pc, this corresponds to 1800 and 2600 au). This is the first study of opacity variation and grain growth across a pre-stellar core at this resolution and at such long wavelengths using a single-dish telescope.

The Chapter is organized as follows. In Section 2.3 we describe the millimeter data for L1544 obtained with NIKA and far-IR data obtained with SPIRE. In Section 2.4 we describe the results for the maps of the spectral index and the opacity assuming constant temperature and density across the cloud, as done in previous studies. This is compared later with the same results assuming variations on both the temperature and the density along the line of sight, making use of the profiles presented by Keto et al. (2015). We end this section by presenting the results for the opacity and spectral index from the combination of NIKA and *Herschel*/SPIRE data, and a comparison between the modeled

emission and the observations. In Section 2.5 we compare our observational findings with a simple grain growth evolution model. In Section 2.6 we summarize our findings.

2.3 Observations

2.3.1 NIKA

The observations were carried out using the IRAM 30 m telescope located at Pico Veleta (Spain) during the spring of 2014 using the New IRAM KID Array (NIKA) (Catalano et al. 2014; Calvo et al. 2013). The project number is 151-13. A region of $3' \times 3'$ was mapped using the Lissajous pattern to observe the pre-stellar core L1544, $\alpha(\mathrm{J2000}) = 05^{\mathrm{h}}04^{\mathrm{m}}17.21^{\mathrm{s}}$ and $\delta(\mathrm{J2000}) = +25^{\circ}\,10'\,42.8''$ (dust peak from Ward-Thompson et al. 1999), at 1.2 and 2 mm. The main beam widths are $12.5''$ at 1.2 mm and $18.5''$ at 2 mm. At a distance of 140 pc, this corresponds to a resolution of 1800 au and 2600 au, respectively. The KID array has a field of view of $1.8'$ at 1.2 mm and $2.0'$ at 2 mm.

The data were reduced by the NIKA team. The original maps were corrected by the ratio of main beam to full beam, which is 1.56 at 1.2 mm and 1.35 at 2 mm, with an uncertainty of $\sim$10% on these factors. The noise level of the map at 1.2 mm is 0.007 Jy/$12.5''$-beam and that of the map at 2 mm is 0.002 Jy/$18.5''$-beam. In Fig. 2.1, both images have been converted into MJy/sr. In Section 2.4.2, the two maps have been convolved to a common resolution of $19''$, reducing the noise levels to 0.9 and 0.15 MJy/sr at 1.2 and 2 mm, respectively. The absolute uncertainty on the surface brightness is $\sim$15%.

The maps show two lobes of negative surface brightness: one to the northeast and another to the southwest, due to filtering of extended emission. As the field of view of the camera differs by $\sim$10% between the two NIKA bands, we expect this filtering to be the same for both bands, and therefore it should not affect our analysis where both bands are treated simultaneously (see Section 2.4.2). To quantify this statement, a study of the power spectra of the two bands is performed in Appendix A. Moreover, Adam et al. (2015) used simulations to estimate at which spatial scales NIKA filters the emission. They found that NIKA filtering starts to be important on scales larger than the field of view and that it is the same for the two bands. This is also mentioned in Adam et al. (2017). Thus, here filtering effects are also assumed to be within the errors found in Section 2.4.3 where the results are shown for each band separately, and only for the region above 3σ detection, which is $\sim 1'$ in size, and therefore smaller than the field of view.

2.3.2 *Herschel*

The *Herschel*/SPIRE data at 250, 350, and 500 μm used here have already been presented by Spezzano et al. (2016). They are part of the Level 3 mosaic maps of the Taurus molecular cloud complex observed in the SPIRE/PACS parallel mode in the course of the *Herschel* Gould Belt Survey (André et al. 2010). The data downloaded from the *Herschel* Science Archive (HSA) are reduced using the Standard Product Generation (SPG) software

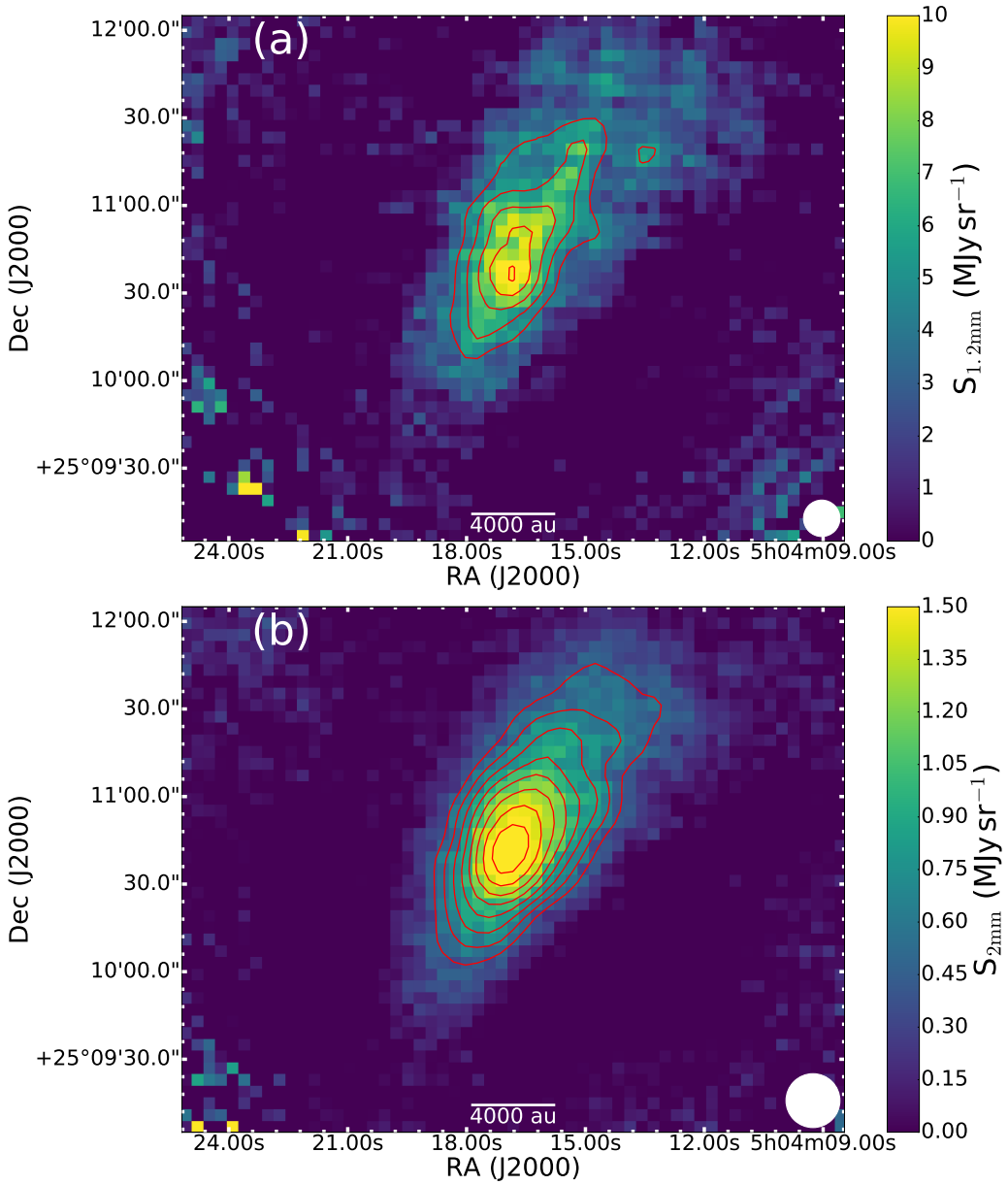

Figure 2.1: Maps of the continuum emission of L1544 at *a)* 1.2 mm and *b)* 2 mm. The angular resolution is 12.5″at 1.2 mm and 18.5″at 2 mm (HPBW shown by the white circle in the bottom right corner) and the contours are indicating the different σ levels of the emission above 3σ (3σ, 4σ, 5σ, etc., where $\sigma_{1.2\mathrm{mm}} = 1.4$ MJy/sr and $\sigma_{2\mathrm{mm}} = 0.15$ MJy/sr).

version 14.2.1. These data are calibrated assuming that the source is infinitely extended, and the surface brightness zero points have been corrected using absolute levels from *Planck* maps. The SPIRE flux densities are assumed to be accurate to 10% (Bertincourt et al. 2016). The resolution of *Herschel* at 500 μm is $\sim$38.5″. When combining the SPIRE maps with the NIKA data, we took into account that SPIRE is sensitive to the extended emission, while NIKA filters it out. To compensate for this difference, we subtracted from each SPIRE map a value that corresponds to the average surface brightness just outside the region seen by NIKA. The region where these averages are calculated was determined from the NIKA 1.2 mm map; this is a $\sim$35 arcsec wide ring outside the 1σ contour. After this subtraction, the peak emission and the errors at 250, 350, and 500 μm are 153$\pm$12, 120$\pm$12 and 62$\pm$9 MJy/sr, respectively. The dependence of our results on the width of the ring was checked, and found not significant.

2.4 Dust properties

2.4.1 Theoretical background

Dust grains emit as modified blackbodies:

$$S_\nu = \Omega B_\nu(T_\mathrm{d})\kappa_\nu \mu_{\mathrm{H}_2} m_\mathrm{H} N(\mathrm{H}_2), \tag{2.1}$$

where $B_\nu(T_\mathrm{d})$ is the blackbody function at a temperature T_d:

$$B_\nu(T_\mathrm{d}) = \frac{2h\nu^3}{c^2}\frac{1}{\exp\left(\frac{h\nu}{kT_\mathrm{d}}\right)-1}, \tag{2.2}$$

S_ν is the flux density, Ω is the solid angle subtended by the beam, κ_ν is the dust opacity at frequency ν (the absorption cross-section for radiation per unit mass of gas), $\mu_{\mathrm{H}_2} = 2.8$ is the molecular weight per hydrogen molecule (Kauffmann et al. 2008), m_H is the mass of the hydrogen atom, and N_{H_2} is the molecular hydrogen column density. The dust opacity can be approximated by a power law at mm wavelengths (Hildebrand 1983)

$$\kappa_\nu = \kappa_{\nu_0}\left(\frac{\nu}{\nu_0}\right)^\beta, \tag{2.3}$$

where κ_{ν_0} is the opacity at a reference frequency ν_0 and β is the spectral index. We assume a dust-to-gas ratio of 0.01[1] in Eq. (2.1), where there are several unknown parameters: the density, the temperature, the opacity, and the spectral index.

The above equations are typically used to derive dust temperatures, densities, and masses, assuming isothermal clouds and using fixed values for the dust opacity and the

[1]Although different dust-to-gas mass ratios have been measured towards different directions in our Galaxy (Draine 2011), we do not expect significant changes within the same cloud.

spectral index (e.g., Schnee & Goodman 2005). The value of the dust opacity is normally taken from Table 1 of Ossenkopf & Henning (1994), and the spectral index is mostly assumed to be within the range of 1.5-2 for pre-stellar cores. However, these approximations and assumptions can give incorrect temperatures, densities, and masses, or false anticorrelations between β and the dust temperature (Shetty et al. 2009a,b).

Here we first follow the calculation of the spectral index done by Schnee & Goodman (2005) assuming a constant temperature of 10 K for the core. We then do the same calculation but using the temperature and density profiles derived by Keto et al. (2015) and compare them to the constant temperature case. Finally, we consider a constant value of the spectral index and the opacity across the core to see if the observed millimeter emission can be reproduced by modeling.

2.4.2 Spectral index and opacity of the dust using NIKA

Assuming constant temperature

For isothermal clouds, the spectral index value can be derived using the ratio of the surface brightnesses at 1.2 and 2 mm:

$$\beta = \frac{\log \frac{S_{1.2\mathrm{mm}}}{S_{2\mathrm{mm}}} - \log \frac{B_{1.2\mathrm{mm}}(T_\mathrm{d})}{B_{2\mathrm{mm}}(T_\mathrm{d})}}{\log \frac{\nu_{1.2\mathrm{mm}}}{\nu_{2\mathrm{mm}}}}. \tag{2.4}$$

Considering a constant $\kappa_{250\mu\mathrm{m}}$=0.1 cm^{2}g^{-1} value (Hildebrand 1983), we can also derive a map for the opacity at 1.2 mm:

$$\kappa_{1.2\mathrm{mm}} = \kappa_{250\mu\mathrm{m}} \left(\frac{\nu_{1.2\mathrm{mm}}}{\nu_{250\mu\mathrm{m}}} \right)^{\beta}. \tag{2.5}$$

The values have only been derived for surface brightnesses above the 3σ level of the maps at 1.2 and 2 mm.

The resulting β and $\kappa_{1.2\mathrm{mm}}$ maps are shown in Fig. 2.2. There is a slight decrease in the spectral index towards the central regions, although its value ($\sim$2) is still consistent with interstellar medium (ISM) dust not affected by coagulation. This observed spatial gradient, which shows appreciable variations of $\sim$30% with an errorbar of $\sim$25% in the spectral index value, reflects the variation in the $S_{1.2\mathrm{mm}}/S_{2\mathrm{mm}}$ ratio across the core as the other quantities in Eq. (2.4) are constant. Therefore, an increase in the temperature in the outskirts would necessarily mimic an increase in β.

The opacity shows a significant increase (a factor of 10) towards the center, with errorbars of $\sim$0.001 cm^{2}g^{-1} in the determination of the opacity values. This could indicate grain growth. However, this result is also affected by the underlying assumption that the temperature is constant across the core, while this is not the case for L1544. Moreover, $\kappa_{250\mu\mathrm{m}}$ may vary as well across the cloud, so the assumption of a constant $\kappa_{250\mu\mathrm{m}}$ along the line of sight may not be a good one.

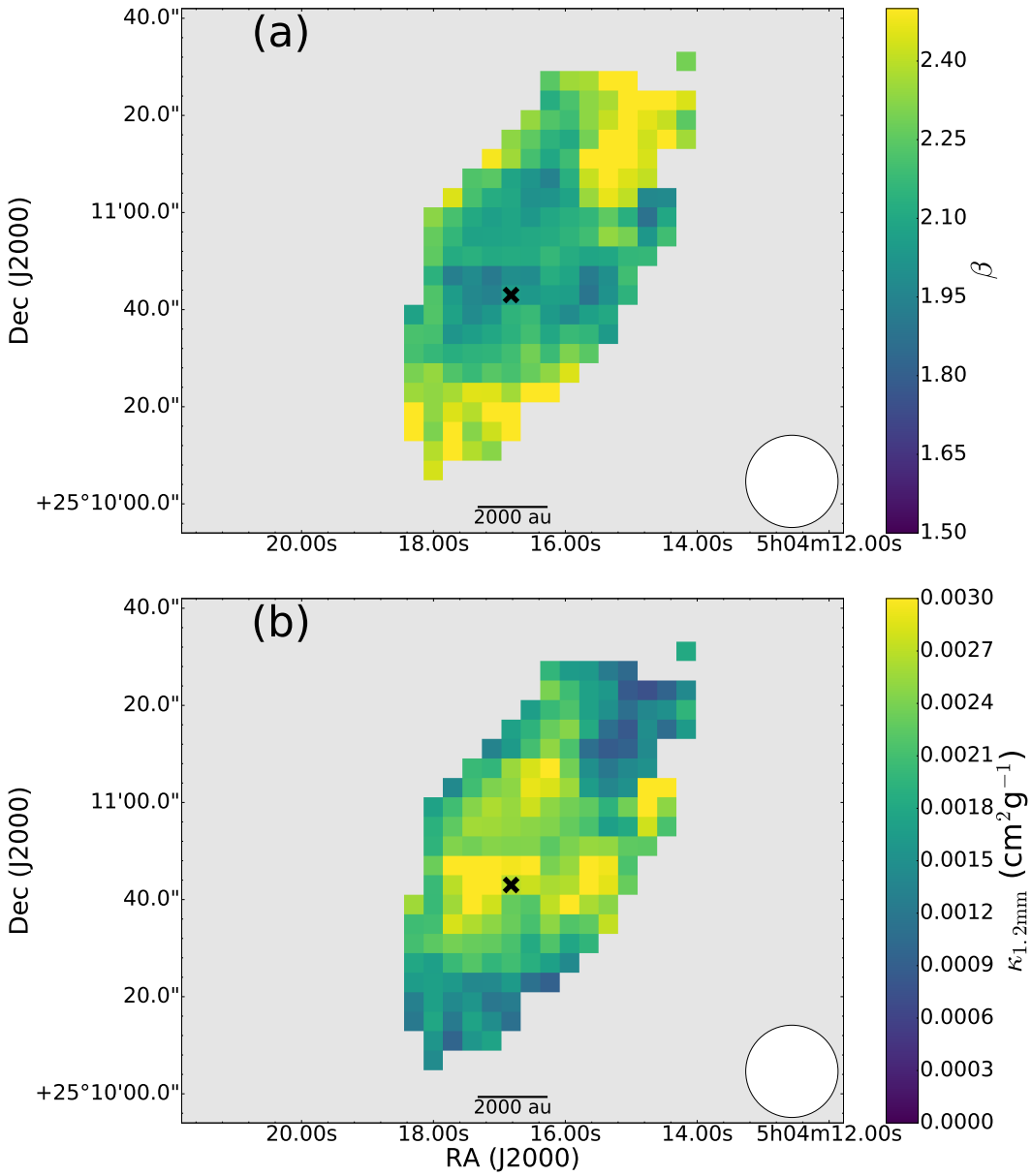

Figure 2.2: Maps of the *a)* spectral index and *b)* opacity at 1.2 mm assuming a constant core temperature of 10 K and a constant $\kappa_{250\mu m}$=0.1 cm^{2}g^{-1} value Hildebrand (1983). The 1.2 mm map was convolved to the 2 mm band resolution, which is 19″ (HPBW shown by the white circle in the bottom right corner). In both cases, the crosses mark the peak of the emission corresponding to the final 1.2 mm map convolved to 19″.

Using the known dust temperature and density profiles of L1544

For L1544 we can make use of the radial density profile, $n_{\mathrm{H_2}}(r)$, and temperature profile, $T(r)$, derived by Keto et al. (2015). These profiles correspond to a spherical model that follows the evolution of an unstable Bonnor-Ebert sphere, reproducing previous observations of L1544. The volume density, $n_{\mathrm{H_2}}$, is related to the column density, $N_{\mathrm{H_2}}$, as $N_{\mathrm{H_2}} = \int_{s_{\mathrm{los}}} n_{\mathrm{H_2}} ds$, i.e., the column density is the volume density integrated over the line of sight; $T(r)$ and $n_{\mathrm{H_2}}(r)$ are shown in Fig. 2.3.

The knowledge of the temperature and density of the core leaves Eq. (2.1) with only two unknown parameters: the dust opacity and spectral index. Therefore, taking into account the variation in the density and the temperature along the line of sight, and the units we use (MJy/sr), Eq. (2.1) for each pixel transforms to

$$S_\nu(r_{ij}) = \kappa_\nu(r_{ij}) \mu_{\mathrm{H_2}} m_{\mathrm{H}} \int_{s_{\mathrm{los}}} B_\nu[T_{\mathrm{d}}(r_{ij})] n_{\mathrm{H_2}}(r_{ij}) \mathrm{d}s, \tag{2.6}$$

where s is the path along the line of sight, which has a direct relation with the radius r, and i and j represent the pixel coordinates on the map.

As in the previous section, the ratio between the surface brightnesses at 1.2 and 2 mm gives us an estimate of β, and consequently the value of κ_ν, although in this case we derive it using

$$\kappa_\nu(r_{ij}) = \frac{S_\nu(r_{ij})}{\mu_{\mathrm{H_2}} m_{\mathrm{H}} \int_{s_{\mathrm{los}}} B_\nu[T_{\mathrm{d}}(r_{ij})] n_{\mathrm{H_2}}(r_{ij}) \mathrm{d}s}. \tag{2.7}$$

This approach is more accurate than the method used in the previous section because it does not assume a constant value for the opacity at a reference frequency, but it uses the clear incorrect assumption that the spectral index and the opacity do not change along the line of sight. This may not be the case: if changes from the outskirts to the center of the core are present, the same change should apply along the line of sight towards the center. This approach also assumes that the spectral index does not depend on the temperature, but as we see in Section 2.2, no significant temperature dependence is expected within the temperature range relevant for L1544 (e.g., Agladze et al. 1996; Mennella et al. 1998; Boudet et al. 2005; Coupeaud et al. 2011; Demyk et al. 2013).

The β and $\kappa_{1.2\mathrm{mm}}$ maps are shown in Fig. 2.4. The behavior of the spectral index does not seem to differ much from that presented in the previous section where a constant temperature was assumed. However, the spatial variations are not significant here; they are negligible within the errors (∼25%). This is due to the fact that the ratio of the term $\int_{s_{\mathrm{los}}} B_\nu[T_{\mathrm{d}}(r_{ij})] n_{\mathrm{H_2}}(r) \mathrm{d}s$ at the two different frequencies does not differ significantly from the value computed assuming a constant temperature of 10 K. On the other hand, the opacity value changes significantly (∼60% with uncertainties of 20%). Thus, the overall $\kappa_{1.2\mathrm{mm}}$ value dispersion is two times larger than before, and surprisingly, the opacity now shows a decreasing trend towards the central regions, contrary to the expectation of grain growth.

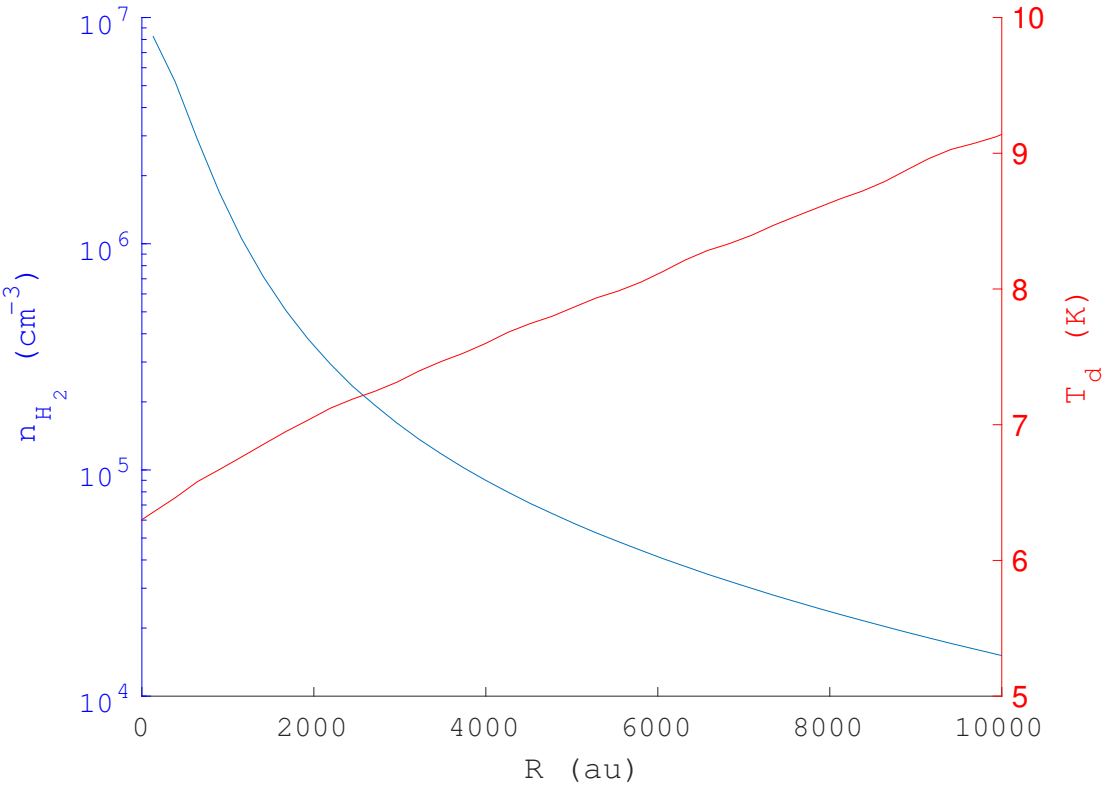

Figure 2.3: Temperature (red) and density (blue) profiles of L1544 from Keto et al. (2015).

The simplest explanation of this apparently contradictory result is that the model assumes spherical symmetry, while L1544 is clearly an elongated core, with an aspect ratio of about 2. This implies that the model cannot be used for the outer parts of the cloud, in particular along the major axis. Moreover, the derivation of the spectral index using the method of the flux ratios with only two wavelengths in the Rayleigh-Jeans limit leads to inaccurate values due to the uncertainties on the fluxes (Shetty et al. 2009b).

2.4.3 Spectral index and opacity of the dust using NIKA and SPIRE

Because of the complex and unknown dependence of the spectral index on the temperature, the uncertainties on the surface brightnesses, and the spherically symmetric model, we consider a different approach here. The modeled densities and temperature profiles are now used to predict the emission at 1.2 and 2 mm, fixing the values of the opacity and the spectral index of the dust. The adopted values for the opacity and the spectral index are derived from the best least-squares fit to the surface brightnesses in the five spectral windows available (three from *Herschel*/SPIRE and two from NIKA) towards the peak emission of L1544 at each band. We assume that the opacity and the spectral index are independent because possible degeneracies between the two parameters are beyond the

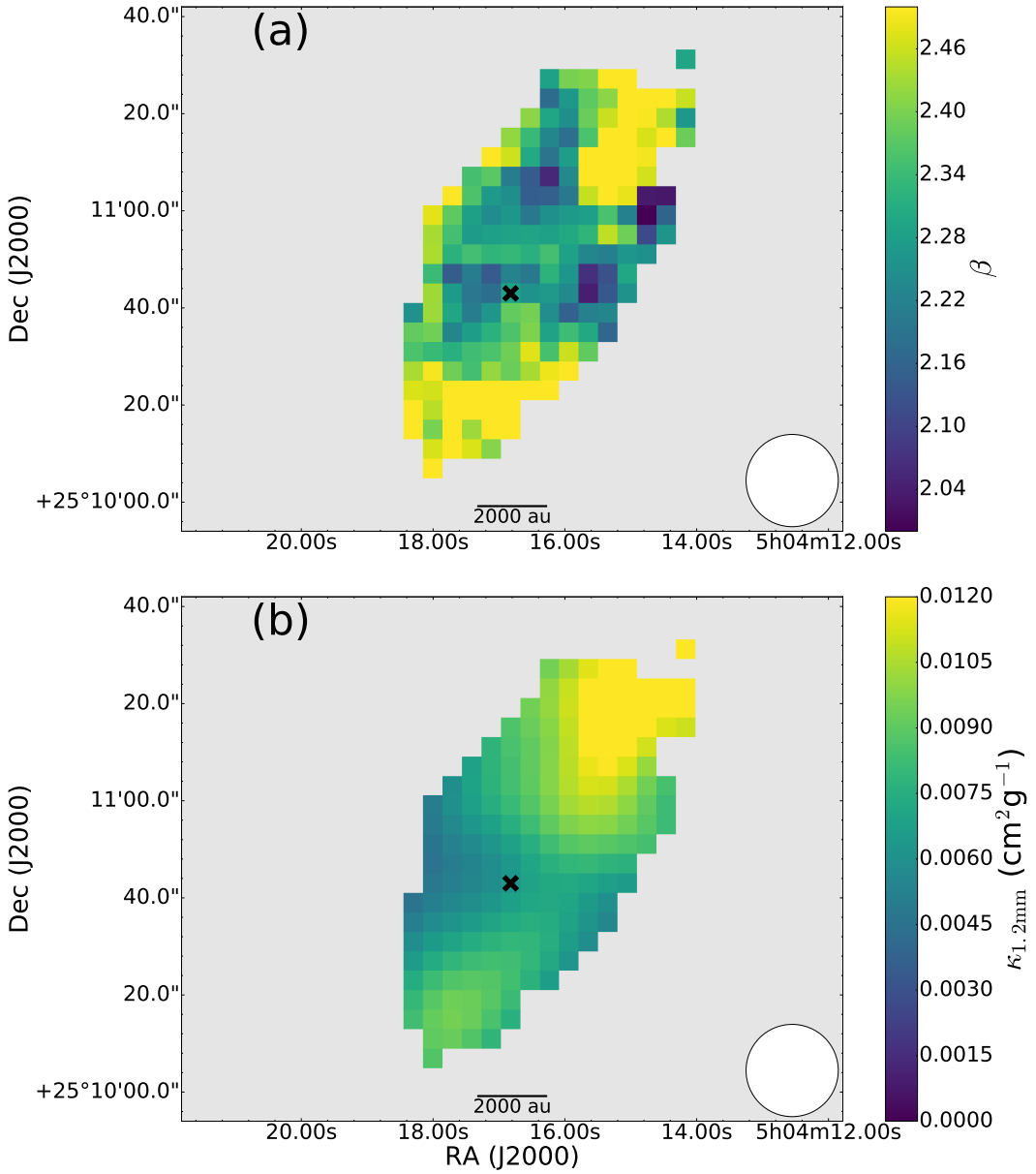

Figure 2.4: Maps of the *a)* spectral index and *b)* opacity at 1.2 mm derived with the method described in Section 2.4.2. The angular resolution is 19″ (HPBW shown by the white circle in the bottom right corner). The crosses mark the peak of the emission corresponding to the final 1.2 mm map convolved to 19″.

scope of this study and are not well-known. Before fitting, the five maps were convolved and regridded to the lowest resolution, i.e., the 500 μm band ($\sim$38.5″ beam and 14″ pixel size), and the *Herschel*/SPIRE bands have been color-corrected assuming an extended source with a spectral index of 2.0. From the model, we derive the term $\int_{s_{\rm los}} B_\nu[T_{\rm d}(r_{ij})]n_{\rm H_2}(r){\rm d}s$ for each pixel in the maps at each frequency and smooth this to the common resolution to introduce in the fitting the corresponding terms, which depend on temperature and density in the center. A least-squares fit is performed to find which values of the opacity and spectral index best match the observations. This procedure is iterative: the spectral index and the corresponding color-correction of the SPIRE bands are varied until a convergence is found. The resultant spectral energy distribution (SED) is shown in Fig. 2.5. The values of $\kappa_{250\mu{\rm m}}$ and β found with this procedure are

$$\kappa_{250\mu{\rm m}} = 0.2 \pm 0.1 \text{ cm}^2\text{g}^{-1} \text{ and } \beta = 2.3 \pm 0.4,$$

where the errors indicate the 95% confidence intervals of the estimates of the fit. Within the uncertainties, this value for the opacity is in agreement with those calculated by Ossenkopf & Henning (1994) for thin and thick ice mantles. However, the spectral index is significantly larger than the value derived by *Planck* for L1544: 1.608±0.007 (Planck Collaboration et al. 2016). This difference could be due to the significantly larger beam for the high-resolution (7.5 arcmin) thermal dust emission map derived using *Planck* frequencies above 143 GHz. In the derivation of the spectral index from *Planck*, a constant dust temperature of 16.55±0.08 K in a region of 1°×1° in size is assumed. This temperature is higher than that observed with ammonia by Crapsi et al. (2007). The sensitivity of *Planck* to large emission and its resolution imply that the variations in the temperature are averaged over a bigger structure along the line of sight, dominated by the envelope, increasing the observed temperature and tracing better the outer part of the core. Moreover, if no temperature variation along the line of sight is taken into account, β is expected to be underestimated (Juvela et al. 2015a); therefore, we adopt our derived value of β as representative for L1544.

To make the comparison between the modeled emission, which is for a sphere, and the observations, we average the emission of the core in ellipses at different distances from the center with an inclination of $\sim$65° (see Fig. 2.6). Only emission within the colored map in Fig. 2.6, which corresponds to positive surface brightnesses, is considered. The results are shown in Fig. 2.7 for NIKA and in Fig. 2.8 for SPIRE, where the ratio between the observed and modeled surface brightnesses is reported as a function of radius. For the observed emission this radius corresponds to the geometric mean of the major and minor axes of the ellipses. The resolution is the native resolution of each band, which corresponds to 18.5″, 12.5″, 38.5″, 26.8″, and 20.3″ at 2 mm, 1.2 mm, 500 μm, 350 μm, and 250 μm, respectively. The agreement is within a factor of 2 in all bands, which leads to the conclusion that there is no need to modify the opacity or the spectral index towards the central regions to reproduce the observed surface brightnesses. We have also checked the dependence of this ratio with the value of the spectral index and the opacity: the mm wavelengths are sensitive to the variation of β and $\kappa_{250\mu{\rm m}}$, increasing and decreasing the surface brightness by a factor of 2 or more. However, if the spectral index and the opacity increase at the same time within the 95% confidence intervals, the ratio between

the observed and the estimated surface brightness remains constant around 1 within the errors. This occurs because an increase in the spectral index decreases the expected surface brightness at mm wavelengths, but an increase in the opacity can compensate this effect and increases the prediction by the same amount. Therefore, variations in these two parameters within the uncertainties (50% and 20% for the opacity and the spectral index, respectively) cannot be detected with our data. The decrease in the ratio between the observed and modeled surface brightness at the outskirts of the core in the case of SPIRE is due to the harsh filtering applied to the data, and the error associated with this procedure is large at $R_m > 4000$ au because the filtering relies on the shape of the 1.2 mm emission, which goes below the 3σ level at $R_m > 4000$ au (see Section 2.3.2 and Appendix A).

These results indicate that the emission is consistent with a constant opacity, at the resolution and sensitivity achieved with NIKA. This is in apparent contradiction with the results of Keto & Caselli (2010), who needed to increase the opacity towards the central regions to reproduce the drop in the temperature measured by Crapsi et al. (2007) using interferometric observations. As explained in Section 2.5.3, higher angular resolution observations are needed to test the prediction made by Keto & Caselli (2010).

2.5 Model predictions on grain growth and comparison with our data

The theoretical studies on grain evolution of Ormel et al. (2009, 2011) show that little grain growth takes place when the cloud lifetime is similar to the free-fall time because the process of coagulation takes longer. However, pre-stellar cores may span a range of lifetimes which significantly exceed the free-fall time (see, e.g., Brünken et al. 2014; Kong et al. 2015; Könyves et al. 2015). If there are processes sustaining the cloud against gravitational collapse (e.g., turbulence and/or magnetic fields), some dust coagulation could take place. Ormel et al. (2009, 2011) show that about 100 μm dust grains can form if gas densities of 10^5 cm^{-3} can be maintained for 10 Myr, while after 1 Myr dust grains can grow up to $\sim$4 μm.

In the following, we present an analytical solution (Blum 2004) to estimate grain growth. Ormel et al. (2009) compared this analytical solution with their Monte Carlo simulation, finding a very good match. We apply this model to the pre-stellar core L1544. As mentioned, L1544 is a very well-known pre-stellar core, centrally concentrated and with high central densities ($\sim 10^6$ cm^{-3} within a radius of 500 au, see Fig. 2.3) which makes it unique and ideal for this study. We consider two different cases: a static core with the physical structure given in Fig. 2.3, and a dynamical core based on the quasi-equilibrium contraction model of Keto et al. (2015), which best reproduce spectroscopic data.

2.5.1 Analytical model

We used a simple analytical model derived by Blum (2004), and checked by Ormel et al. (2009), who compared it with their Monte Carlo simulation and demonstrated its validity

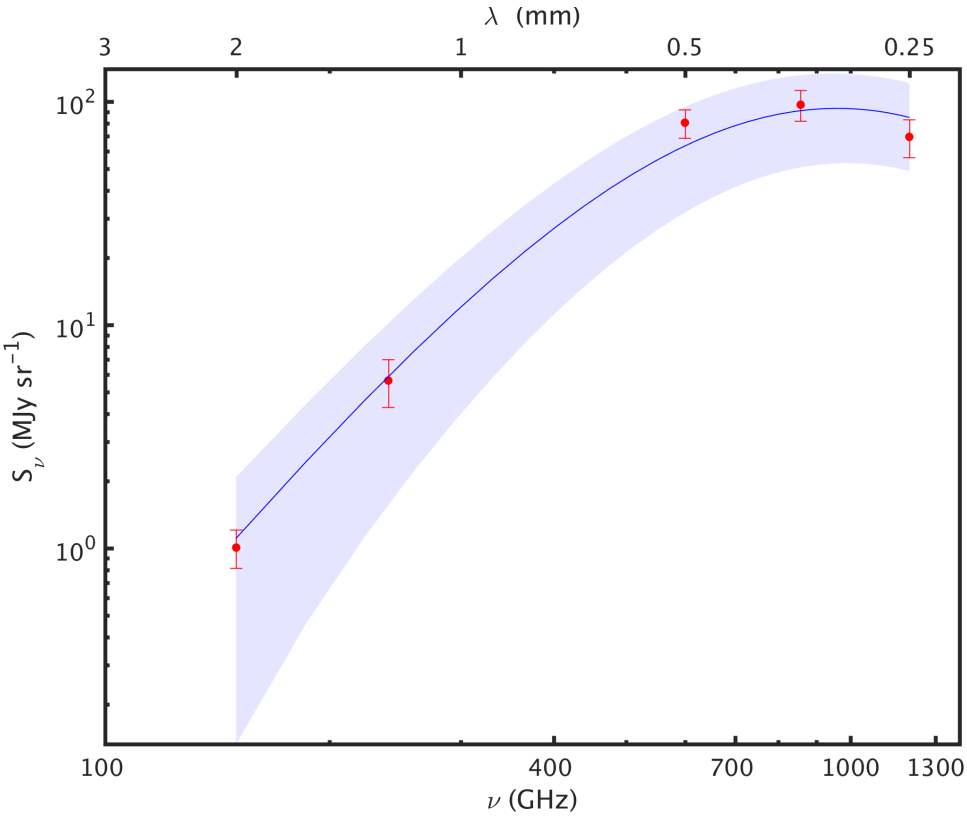

Figure 2.5: Fit of the SED to the five spectral windows available at 250, 350, 500, 1250, and 2000 μm at the peak emission when convolving and regridding all windows to the resolution of the 500 μm band. The error bars indicate the weights used in the fitting, which correspond to the uncertainties and noise associated with the data. The shadowed blue region show the 95 % confidence intervals of the fitted parameters.

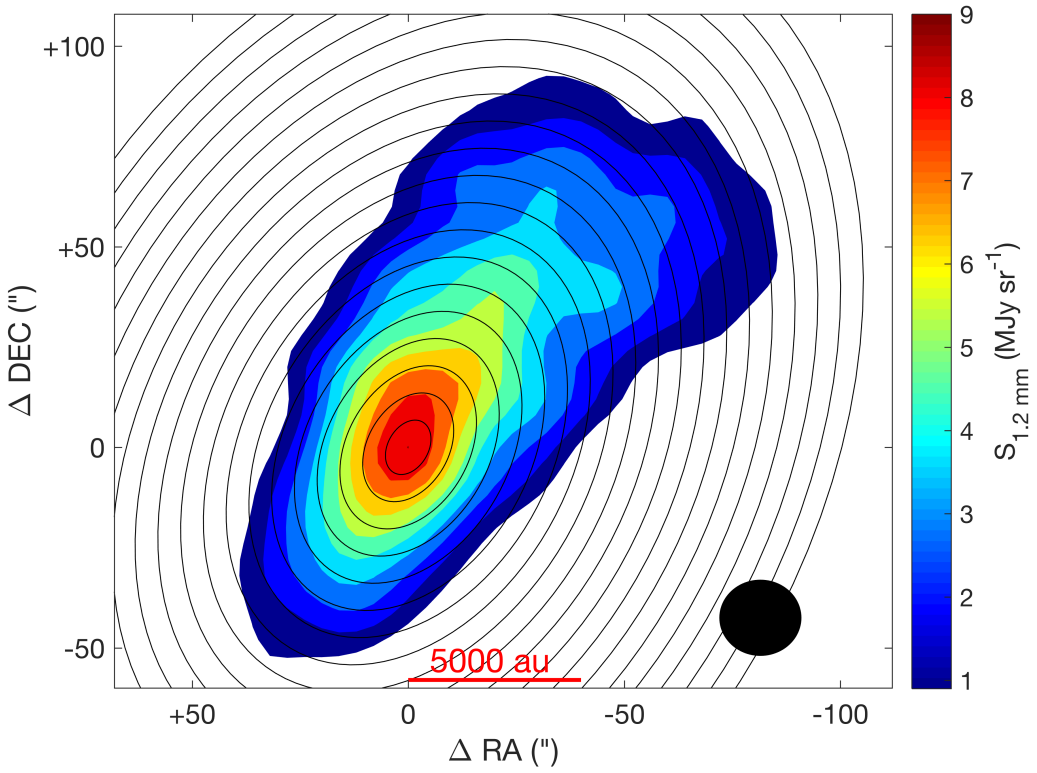

Figure 2.6: Ellipses where the emission has been averaged for the 1.2 mm and 2 mm maps superimposed on the 1.2 mm continuum map of L1544. Only the colored region is included in the average. The resolution is 19″ (HPBW shown by the black circle in the bottom right corner). For *Herschel*/SPIRE the distance between concentric ellipses is larger, due to a larger pixel size and resolution. For both NIKA and SPIRE, the distance between ellipses is chosen to be ∼1.8 pixels, averaging in a 1 pixel wide ring.

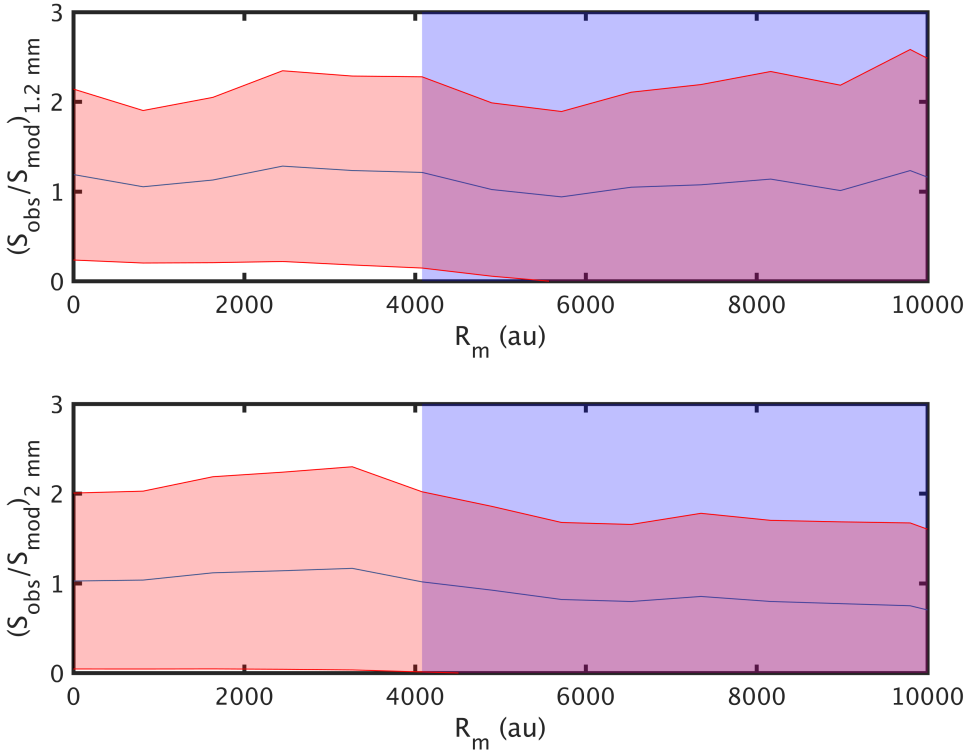

Figure 2.7: Ratio between the observed and the modeled surface brightnesses at 1.2 mm (*top*) and 2 mm (*bottom*) as a function of geometric mean radius of the ellipses in Fig. 2.6, using the temperature and density profiles from Keto et al. (2015) and an opacity value of $\kappa_{250\mu m} = 0.2 \pm 0.1$ cm^{2}g^{-1} and $\beta = 2.3 \pm 0.4$. The shadowed red region represents the uncertainties on the fluxes, the opacity, and the spectral index. The shaded blue region indicates the zone where the observed surface brightness is below 3σ.

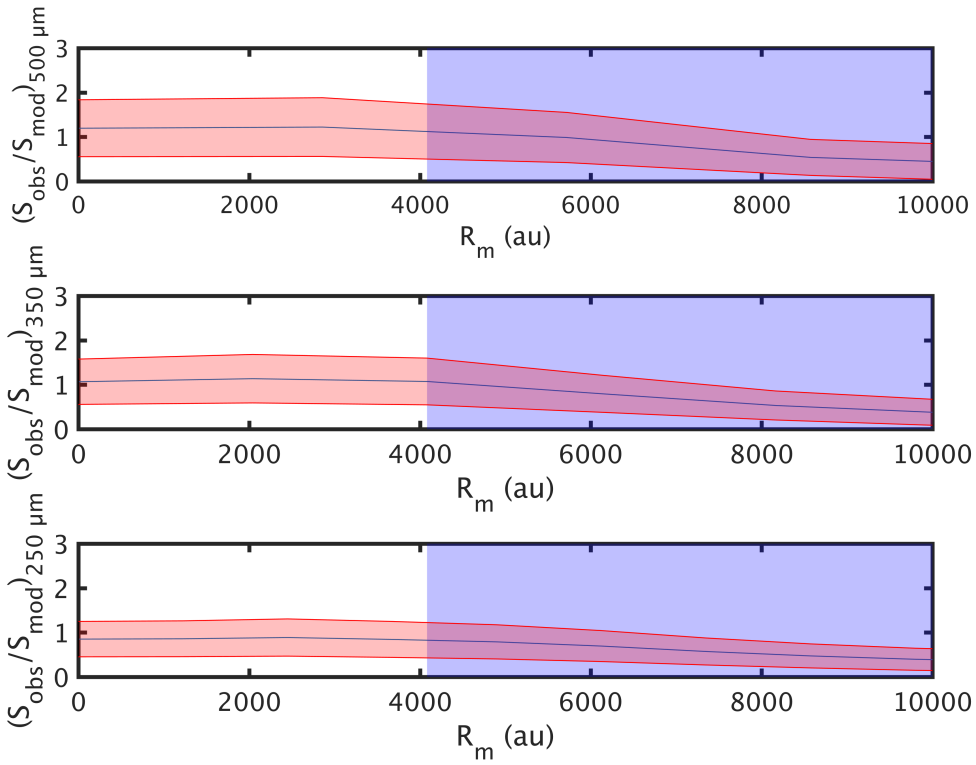

Figure 2.8: Ratio between the observed and the modeled surface brightnesses at 500 μm (*top*), 350 μm (*middle*), and 250 μm (*bottom*) as a function of the geometric mean radius of the ellipses, as explained in Fig. 2.6, using the temperature and density profiles from Keto et al. (2015) and an opacity value of $\kappa_{250\mu\mathrm{m}} = 0.2 \pm 0.1$ cm^{2}g^{-1} and $\beta = 2.3 \pm 0.4$. The shadowed red region represents the uncertainties on the fluxes, the opacity, and the spectral index. At 250 μm, the dashed lines coincide with the solid blue line, when $\beta = 2.3$, as the reference wavelength for the opacity is at 250 μm. The shaded blue region indicates the zone where the millimeter observed surface brightness is below 3σ as the artificial filtering of *Herschel*/SPIRE relies on the shape of the 1.2 mm emission (see Section 2.3.2 and Appendix A).

for average molecular cloud conditions (density 10^5 cm^{-3}, temperature 10 K, and intermediate velocity regimes[2], Ossenkopf 1993; Ormel et al. 2009; Ormel & Cuzzi 2007). The analytical model is based on the assumption of a monodisperse distribution of spherical particles. As the particles coagulate, they form bigger grains made out of N monomers with a characteristic filling factor that describes their shape (fractal or compact). Here we use the terminology used by Ormel et al. (2009), as well as the parameters and equations derived from their simulations.

The initial evolution of the process of grain growth through grain-grain collisions can be divided into two different regimes: the fractal regime and the compaction regime (Ormel et al. 2009; Blum 2004). The fractal regime is characterized by growth with no visible restructuring of the grain; which also includes the hit-and-stick regime. By contrast, during the compaction regime dust grains undergo changes in their structure. The transition point from one regime to another is determined by the parameter N_1 (see Appendix A from Ormel et al. 2009), which strongly depends on the grain size. The bigger the grain, the lower N_1 and the easier it is to reach the compact limit. Instead, N_2 (see Appendix A in Ormel et al. 2009) defines the transition point between the compaction regime and the fragmentation regime where grains start to lose monomers in grain-grain collision. When this regime is reached, it is assumed that the grains do not grow further, and the growth is compensated with fragmentation. When grains are close to this regime in high-density environments, the simple model overestimates the growth compared to Ormel et al. (2009), due to the high dependency of N_1 with density.

To define the transition points N_1 and N_2, we apply the same criteria as in Ormel et al. (2009). The complete expressions for N_1 and N_2 can be found in their Appendix A and follow

$$N_1 \propto \left(\frac{n}{10^5\,\mathrm{cm}^{-3}}\right)^{3.75} \left(\frac{a_0}{0.1\,\mu\mathrm{m}}\right)^{-22.5} \tag{2.8}$$

and

$$\frac{N_2}{N_1} \propto \left(\frac{a_0}{0.1\,\mu\mathrm{m}}\right). \tag{2.9}$$

It should be noted here that n is the number density of gas molecules, related to $n_{\mathrm{H_2}}$ as $n \simeq n_{\mathrm{H}}/1.7 = 2n_{\mathrm{H_2}}/1.7$, and a_0 is the initial grain size.

As derived in Blum (2004) and used by Ormel et al. (2009), the equation to solve is

$$\frac{\mathrm{d}N}{\mathrm{d}t} = \frac{N}{t_{\mathrm{coll}}} = \frac{N^{5/6}\phi_\sigma^{-1/3}}{t_{\mathrm{coll},0}}, \tag{2.10}$$

where N is the number of monomers and ϕ_σ is the filling factor of the dust grain, a quantity that indicates the fluffiness of the grains. Its value is assumed to be $N^{-3/10}$ for the fractal regime and $N_1^{-3/10}$ for the compact regime. For the fragmentation regime we adopted the value 0.33 (Ormel et al. 2009; Blum & Schräpler 2004). In our calculations the

[2]The intermediate velocity regime is defined as the velocity range within which the gas-dust friction time is greater than the eddy turnover time. In these conditions, the velocity scales with the square root of the largest particle friction time (Ormel et al. 2009; Ormel & Cuzzi 2007).

fragmentation regime is reached in the center of the core if we maintain the observed central density of L1544 constant with time for $t \gtrsim 0.7$ Myrs. However, as shown in Section 2.5.3, this regime is not reached when a more realistic dynamical evolution is taken into account.

2.5.2 Deriving optical properties

Once the final expressions for the number of monomers that can coagulate after a certain time of evolution are derived, the corresponding grain size and the grain opacity can be calculated.

To calculate dust grain opacities, we use the code described in Woitke et al. (2016)[3]. Additional information can be found in Toon & Ackerman (1981); Min et al. (2005); Dorschner et al. (1995); and Zubko et al. (1996). We do not enter into the details of dust grain composition and ice mantles in the calculation of the dust opacity as only differential values are of importance in our study and the option of adding ice mantles to dust grains has not been yet implemented in the online version of the code presented by Woitke et al. (2016). However, ice mantles should be considered in further detailed analysis. We refer to this code as the opacity calculator.

To relate the number of monomers with the final grain size, we follow the suggestion of Ormel et al. (2011) and consider the projected surface equivalent radius as the final particle size introduced into the opacity calculator:

$$a_\sigma = \left(a_0^3 \frac{N}{\phi_\sigma} \right)^{1/3} . \tag{2.11}$$

This is calculated for every value of N obtained.

Finally, the size distribution is approximated by a power-law function of the form $n(a)\mathrm{d}a \propto a^{-p}$ (Woitke et al. 2016) and then integrated between the maximum and minimum grain size present along the line of sight using the opacity calculator. Therefore, we give as input in the opacity calculator the different grain size distributions.

2.5.3 Results

Grain growth depends on density, temperature, and dust grain properties. As the temperature and density profiles of L1544 are relatively well known, we can estimate the grain growth in different points of the cloud and predict how much grain size variation is present across the core. We then convolve the modeled distribution with the instrumental beam size to simulate observations.

We consider two scenarios: one where the cloud has not evolved and has maintained its density structure over time, hereafter static cloud, and another where the cloud has evolved and changed its structure with time, hereafter dynamic cloud. In the dynamic scenario, we use the density profiles at different times of evolution of a Bonnor-Ebert sphere in quasi-equilibrium contraction, starting from an unstable dynamical equilibrium state with

[3]The code is available at `https://dianaproject.wp.st-andrews.ac.uk/`

an initial density of 10^4 cm^{-3} as deduced by Keto et al. (2015, their Fig. 3), and stopping when the observed L1544 central density is reached ($t \sim 1.06$ Myrs). The density change is followed in steps by interpolating the various density profiles at different times. Integrating over an interval of time, we can then obtain the grain size distribution evolution starting from an assumed monodisperse initial distribution, and the opacity corresponding to that distribution.

In both cases, the monodisperse distribution starts with $a_0 = 0.1$ μm, and follows the grain evolution at every period of time in the Keto et al. (2015) dynamical model. The corresponding opacity maps are convolved with a beam of $20''$ for simulating NIKA observations and of $2''$ to simulate observations with the Atacama Large Millimeter and submillimeter Array (ALMA).

In the static cloud, with the same density and temperature profiles as L1544, dust grains grow in the center up to cm sizes in 1.06 Myrs. We consider this result not realistic for two reasons. First, it implies a constant central density of 10^7 cm^{-3} for 1.06 Myrs, while Keto & Caselli (2010) and Keto et al. (2015) have shown that observed line profiles towards this pre-stellar core are consistent with quasi-equilibrium contraction motions; this dynamical evolution implies central densities larger than 10^6 cm^{-3} only in the last $\sim$0.06 Myrs. Second, the analytical model overestimates grain growth for densities significantly higher than 10^5 cm^{-3}. For densities of 10^6 cm^{-3} and 10^7 cm^{-3}, the analytic formula overestimates the grain growth by a factor of $\sim$3 and $\sim$50, respectively, after 1 Myr. In the more realistic dynamical cloud model, the grains reach sizes up to $\sim$230 μm in the core center after a time evolution of 1.06 Myrs.

The corresponding opacities at 1.2 mm, which without filtering are proportional to the expected flux, are shown in Fig. 2.9 and Fig. 2.10 for the static and dynamical cloud, respectively. In the case of a static cloud, the predicted variation in the opacity across the cloud would have been seen with our data, as it predicts a variation of a factor of $\sim$1.5 in the opacity value at NIKA's resolution. In Fig. 2.9, it is also evident that there is a drop in opacity when the grains are much larger than the wavelength at which the opacity is derived at ALMA's resolution, and an enhancement where $a \sim \lambda$ between 1000 and 2000 au. For the dynamic cloud (Fig. 2.10), the variation at NIKA's resolution is not observable with the sensitivity reached as it is below 15%, and the RMS of our data corresponds to $\sim$15% of the peak emission. This result is consistent with our observations, which show that no change in the opacity is seen or needed to reproduce the NIKA data. However, Fig. 2.10 shows that the dust opacity change should be detected with high-resolution telescopes like ALMA as an opacity increase of a factor of 2.5 is predicted towards the central regions of the pre-stellar core. This is a difficult task, as ALMA would filter the extended emission, but the scale we need to look at to find the opacity change is the central 1000-2000 au, and under the right observational configurations (an angular resolution of at least $\sim 5''$ to obtain an expected change in the opacity of a factor of $\sim$2, the inclusion of the Atacama Compact Array and mosaicking) this can be achieved. Therefore, we conclude that ALMA is needed to detect grain growth within pre-stellar cores similar to L1544.

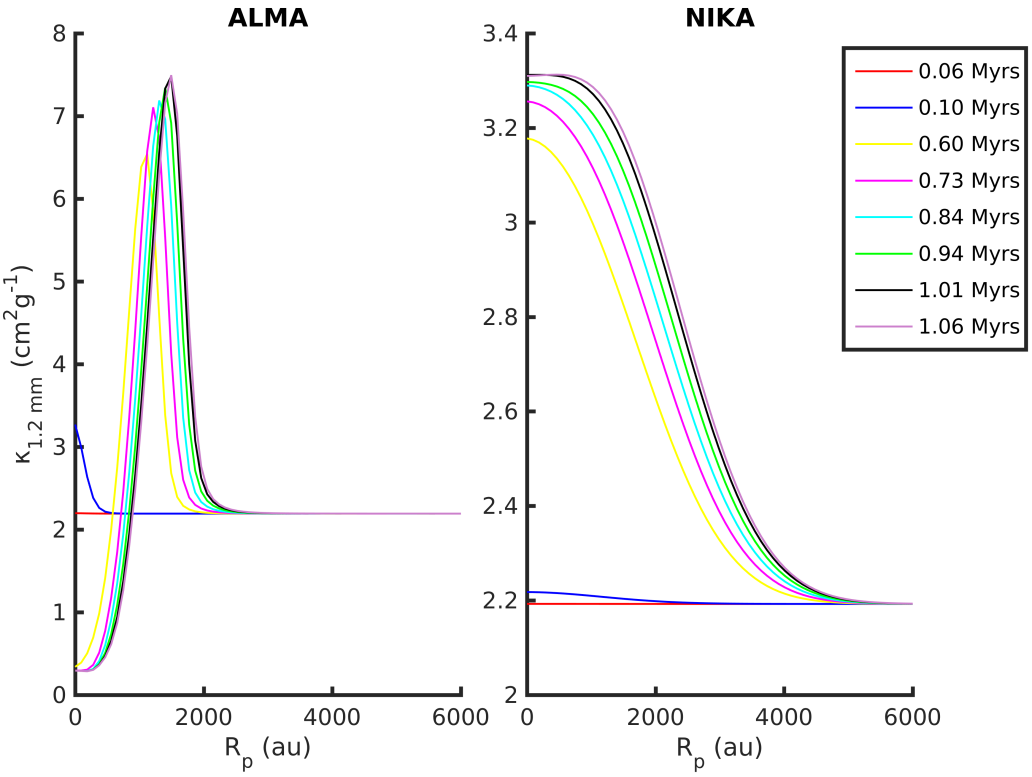

Figure 2.9: Opacity variation with time and projected radius deduced with ALMA (*left*) and NIKA (*right*) simulated observations for the case of a static cloud. The opacity for the NIKA simulated observations changed by a factor of ∼1.5, while for ALMA by a factor of ∼14.

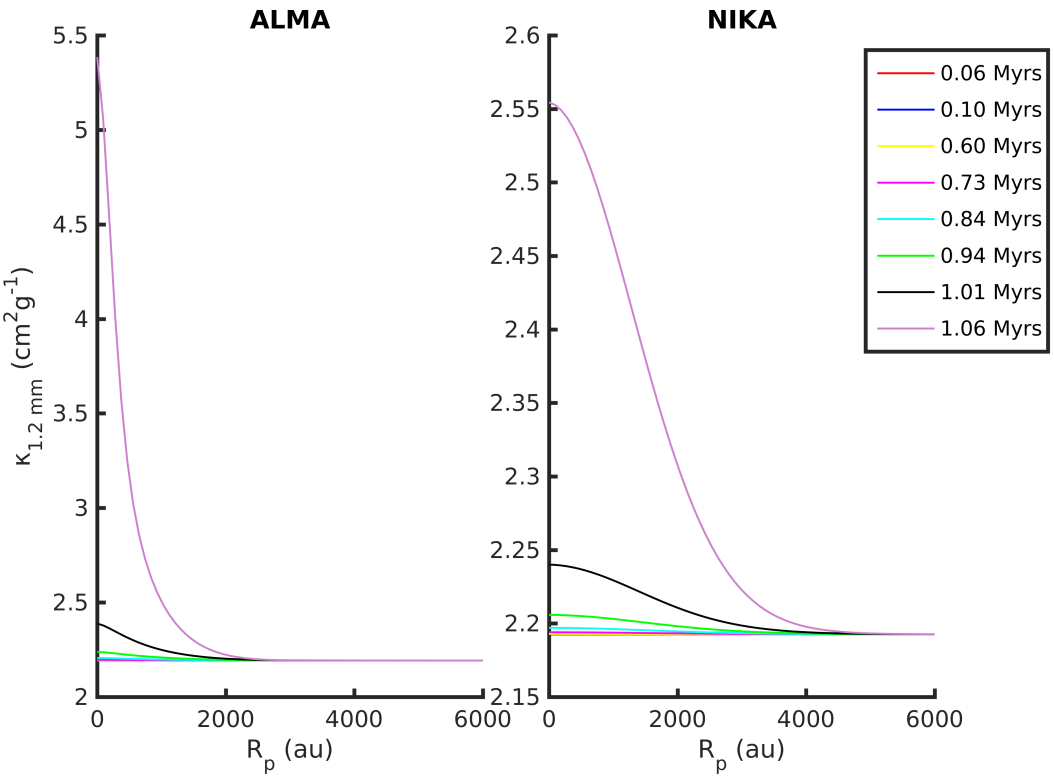

Figure 2.10: Opacity variation with time and projected radius deduced with ALMA (*left*) and NIKA (*right*) simulated observations for the case of a dynamical cloud. The change in the opacity between the center and the outer edge for the case of NIKA is less than 15%, while for ALMA it is a factor of ∼2.5 after 1.06 Myrs of evolution.

2.6 Conclusions

Our work has focused on the search of grain growth towards the central regions of a contracting pre-stellar core, at the earliest phases of the star formation process. We have analyzed the emission from L1544 at 1.2 and 2 mm using the continuum camera at the 30 m IRAM telescope, NIKA. We searched for variation across L1544 on the spectral index and the opacity of the dust as these parameters are sensitive to grain size.

In the derivation of the dust spectral index and opacity, we demonstrate that assumptions on constant dust temperature and spherical symmetry can lead to incorrect conclusions about grain growth.

We investigated the possibility of reproducing, from the model of Keto et al. (2015), the flux seen with NIKA using a constant opacity and spectral index. From the SED fit towards the center of the core using *Herschel*/SPIRE and NIKA bands, the derived values of $\kappa_{250\mu\mathrm{m}}$ and β are: $\kappa_{250\mu\mathrm{m}} = 0.2 \pm 0.1$ cm^{2}g^{-1} and $\beta = 2.3 \pm 0.4$. We find that there is no need to increase the opacity towards the central regions to be able to reproduce the observed fluxes. This means that no signatures of grain growth are present towards L1544, within the limits of our data.

Finally, a simple analytical model of grain growth applied to L1544 shows that NIKA observations cannot detect opacity changes across the core and that only interferometers, in particular ALMA, can provide information about grain growth towards the central regions of L1544.

To know the grain size distribution in the earliest phases of star formation is important as the presence of grain growth might affect the future formation of protoplanetary disks and their physical and chemical evolution. In the future, we plan to use ALMA and the Karl G. Jansky Very Large Array (JVLA) data to test our prediction and to extend our study to other dense cores embedded in different environments.

Chapter 3

Mapping deuterated methanol toward L1544: I. Deuterium fraction and comparison with modeling

This Chapter is based on: Chacón-Tanarro, A., Caselli, P., Bizzocchi, L., Pineda, J. E., Sipilä, O., Vasyunin, A., Spezzano, S., Punanova, A., Giuliano, B. M., and Lattanzi, V., re-submitted to A&A on the 10th of April, 2018.

3.1 Abstract

Context. The study of deuteration in pre-stellar cores is important to understand the physical and chemical initial conditions in the process of star formation. In particular, observations toward pre-stellar cores of methanol and deuterated methanol, solely formed on the surface of dust grains, may provide useful insights on surface processes at low temperatures.

Aims. Here we analyze maps of CO, methanol, formaldehyde and their deuterated isotopologues toward a well-known pre-stellar core. This study allows us to test current gas-dust chemical models.

Methods. Single-dish observations of CH_3OH, CH_2DOH, H_2CO, $H_2\,^{13}CO$, HDCO, D_2CO and $C^{17}O$ toward the prototypical pre-stellar core L1544 were performed at the IRAM 30 m telescope. We analyze their column densities, distributions, and compare these observations with gas-grain chemical models.

Results. The maximum deuterium fraction derived for methanol is $[CH_2DOH]/[CH_3OH] \sim 0.08\pm0.02$, while the measured deuterium fractions of formaldehyde at the dust peak are $[HDCO]/[H_2CO] \sim 0.03\pm0.02$, $[D_2CO]/[H_2CO] \sim 0.04\pm0.03$ and $[D_2CO]/[HDCO] \sim 1.2\pm0.3$. Observations differ significantly from the predictions of models, finding discrepancies between a factor of 10 and a factor of 100 in most cases. It is clear though that to efficiently produce methanol on the surface of dust grains, quantum tunneling diffusion of H atoms must be switched on. It also appears that the currently adopted reactive des-

orption efficiency of methanol is overestimated and/or that abstraction reactions play an important role. More laboratory work is needed to shed light on the chemistry of methanol, an important precursor of complex organic molecules in space.

3.2 Introduction

Pre-stellar cores form in molecular clouds, due to the influence of gravity, magnetic fields and turbulence. They are dense ($n_{\rm H_2} > 10^5\,{\rm cm^{-3}}$) and cold ($T$ <10 K) toward their center (Keto & Caselli 2010). They are the starting point in the process of star formation (Bergin & Tafalla 2007; Caselli & Ceccarelli 2012), as they are self-gravitating dense cores which present signs of contraction motions and chemical evolution (Crapsi et al. 2005). Hence, they represent ideal laboratories to study the early evolutionary stages of low-mass star formation.

Methanol (CH_3OH) is one of the most widespread organic molecules in the ISM and a major precursor of chemical complexity in space. Methanol is believed to form on dust grain surfaces by sequential addition of hydrogen atoms to adsorbed CO molecules (Tielens & Hagen 1982; Watanabe & Kouchi 2002). This process should take place in cold dense cores at densities above $10^4\,{\rm cm^{-3}}$, where large amounts of gas-phase CO molecules start to freeze-out onto dust grain surfaces (Willacy et al. 1998; Caselli et al. 1999; Tafalla et al. 2002).

In L1544, the CH_3OH emission has an asymmetric ring-like shape surrounding the dust peak (Bizzocchi et al. 2014; Vastel et al. 2014). The methanol peak is about 4000 au away from the core center and its distribution can be reproduced by the recent gas-grain chemical model (applied to L1544) by Vasyunin et al. (2017). This can be understood by the fact that the CH_3OH molecule can more easily desorb from the grain surface when a significant fraction of surface ice is in CO, and CO-rich dust surfaces are present around 4000-5000 au away from the core center because of the fast CO freeze-out at that location and the different CO and H_2O photodesorption rates (Vasyunin et al. 2017).

Deuterated methanol should follow the methanol distribution, as they are both formed on the surface of dust grains. However, as already found by previous authors (Caselli et al. 2002b), the deuterium fraction increases toward the densest and coldest parts of the core, where CO is mainly in solid form. Toward the center, due to the dissociative recombination of the abundant deuterated forms of H_3^+, the D/H atomic ratio increases from the cosmic value ($\sim 1.5\times10^{-5}$; Linsky et al. 2006) to values larger than 0.1 (e.g. Roberts et al. 2003). Thus, toward the core center, D atoms compete with H atoms in the saturation of CO molecules, efficiently producing deuterated methanol (Aikawa et al. 2012; Taquet et al. 2012; Ceccarelli et al. 2014). Observations toward L1544 showed that the centroid velocity (V_{LSR}) of CH_2DOH is about 0.2 km/s lower than that of CH_3OH (Bizzocchi et al. 2014); this shift is the same as the one found when comparing the V_{LSR} of $C^{17}O$ (1-0), which traces the outer parts of the core, with the V_{LSR} of N_2D^+ (2-1), mainly tracing the dense central regions where CO is frozen out (Caselli et al. 2002a), thus suggesting that CH_2DOH is tracing denser regions compared to CH_3OH, in agreement

with the theoretical expectations. However, this hypothesis is based on the results of single pointing observations, so no information on the spatial distribution of CH_2DOH in the core can be inferred.

Formaldehyde (H_2CO) can be formed both via grain–surface chemistry (in an intermediate step of the formation of methanol) and gas-phase chemistry (e.g. through reactions of hydrocarbons with oxygen atoms; Yamamoto 2017). Which route actually dominates is still a matter of debate (Parise et al. 2006). In fact, Parise et al. (2009) suggested that pure gas-phase chemistry can account for the abundances of formaldehyde and its deuterated species observed toward the Orion Bar PDR. On the other hand, Bergman et al. (2011) had to invoke grain–surface chemistry to explain the high deuteration found in the ρ Oph A cloud. Interestingly, these authors found D_2CO to be more abundant than HDCO.

The deuterium fraction measured in N_2H^+, NH_3, H_2CO and CH_3OH (Emprechtinger et al. 2009; Bianchi et al. 2017) reaches the largest values in dynamically evolved starless cores (pre-stellar cores) and toward the youngest protostellar objects, while it decreases in more evolved phases in the low-mass star formation process. The study of different evolutionary stages is thus important to be able to understand how the deuterium budget builds up in molecules formed preferentially in the gas phase and on dust grain surfaces, and to follow these processes during the dynamical evolution of star forming clouds. We focus our investigation on L1544, a nearby well-known pre-stellar core in the Taurus Molecular Cloud. Here, we study the spatial features of the methanol and formaldehyde deuteration, together with the CO distribution, as CO is thought to be the parent molecule of methanol. The objective is to gain insights on the surface chemistry and the early history of deuteration during the formation of low-mass stars, which is still unknown.

The structure of the Chapter is the following: in Section 3.3 we describe the observations, followed by the results in Section 3.4. The analysis, comparison with models, and discussion are presented in Sections 3.5, 3.6 and 3.7, respectively. Our findings are finally summarized in Section 3.8.

3.3 Observations

The data presented here were observed using the IRAM 30 m telescope, located at Pico Veleta (Spain), during 4 observing sessions in 2014 and 2015. We obtained On-The-Fly (OTF) maps for 3 and 2 mm emission lines of the molecules: CH_2DOH, CH_3OH, H_2CO, $H_2{}^{13}CO$, HDCO, D_2CO, and $C^{17}O$ (see Table 3.1). A region of $2.5' \times 2.5'$ was mapped in all the lines, except $C^{17}O$, for which a $4' \times 4'$ OTF map was performed. We applied beam switching for these maps. Various E090/E150 EMIR (Eight MIxer Receiver, heterodyne receiver) setups were adopted, and VESPA (VErsatile SPectrometer Assembly) was used as backend for CH_3OH, CH_2DOH, and $C^{17}O$, with a spectral resolution of 20 kHz. The data for formaldehyde and its deuterated species were collected using the FTS backend with a spectral resolution of 50 kHz. All the maps were finally convolved to a common angular resolution of $30''$, in order to facilitate the comparison between different molecules.

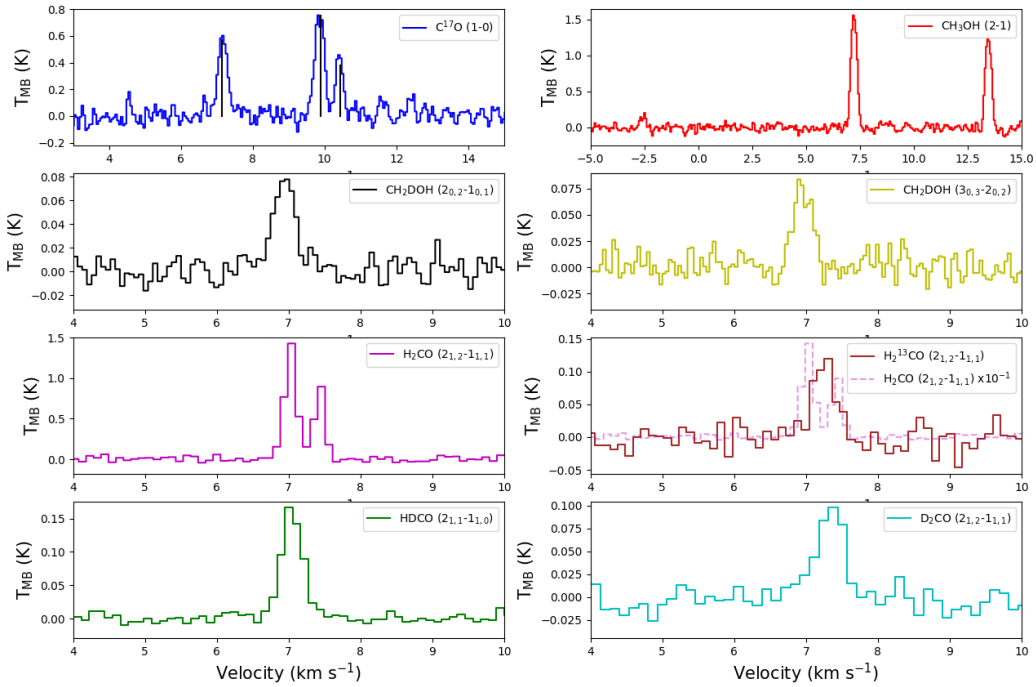

Figure 3.1: Averaged spectra of all lines in the central ∼30×30 arcsec^2. The specifications of the lines and the spectra are shown in Table 3.1. The H_2CO ($2_{1,2}$-$1_{1,1}$) spectrum is superposed on the H_2 ^{13}CO ($2_{1,2}$-$1_{1,1}$) spectrum to show that the H_2CO ($2_{1,2}$-$1_{1,1}$) line is self-absorbed. Superposed on the $C^{17}O$ spectrum there are three lines that indicate the relative intensities of the hyperfine components.

The initial data reduction was done with GILDAS[1].

The observations were done under average good weather conditions ($\tau_{225\,\mathrm{GHz}} \sim 0.1-0.5$, i.e. $pwv \sim 2-8$mm), and with T_{sys} ranging from ∼100 to ∼150 K for the 3 mm band, and from ∼100 K to ∼160 K for the 2 mm band. All spectra were converted from T_A^* to T_{mb} using the forward and main beam efficiency ratios shown in Table 3.1. The spectra obtained averaging the central 30×30 arcsec^2 of each map are shown in Fig. 3.1.

[1]https://www.iram.fr/IRAMFR/GILDAS/

Table 3.1: Lines observed, their rest frequency, noise level, velocity resolution, map pixel size, forward and beam efficiency ratio, and the references for the spectroscopic information for each line.

Line	Rest frequency (MHz)	rms (mK)	Velocity resolution ($km\,s^{-1}$)	Pixel size (arcsec)	F_{eff}/B_{eff}	References
CH_3OH ($2_{0,2}$-$1_{0,1}$, A^+)	96 741.375 ± 0.003	62	0.06	5	1.18	1
CH_3OH ($2_{1,2}$-$1_{1,1}$, E_2)	96 739.362 ± 0.003	62	0.06	5	1.18	1
CH_3OH ($2_{0,2}$-$1_{0,1}$, E_1)	96 744.550 ± 0.003	62	0.06	5	1.18	1
CH_2DOH ($2_{0,2}$-$1_{0,1}$, e_0)	89 407.817 ± 0.002	15	0.07	5	1.18	2
CH_2DOH ($3_{0,3}$-$2_{0,2}$, e_0)	134 065.381 ± 0.002	15	0.04	5	1.25	2
H_2CO ($2_{1,2}$-$1_{1,1}$)	140 839.502 ± 0.010	40	0.10	5	1.26	3, 4
$H_2\,^{13}CO$ ($2_{1,2}$-$1_{1,1}$)	137 449.950 ± 0.004	30	0.11	5	1.26	5
HDCO ($2_{1,1}$-$1_{1,0}$)	134 284.830 ± 0.100	10	0.11	5	1.20	6
D_2CO ($2_{1,2}$-$1_{1,1}$)	110 837.830 ± 0.100	17	0.13	5	1.25	6
$C^{17}O$ (1-0)	112 360.007 ± 0.015	75	0.05	4	1.20	7

References: (1) Xu & Lovas (1997); (2) Pearson et al. (2012); (3) Müller & Lewen (2017); (4) Cornet & Winnewisser (1980); (5) Muller et al. (2000); (6) Bocquet et al. (1999); (7) Klapper et al. (2003). The references and values from (3) to (7) were found using the CDMS (Cologne Database for Molecular Spectroscopy; Müller et al. 2001, 2005).

3.4 Results

The integrated intensities were derived calculating the zeroth moment of the maps using a custom code written in Python, making use of Astropy (Astropy Collaboration et al. 2013), SciPy and NumPy (van der Walt et al. 2011). In this section only part of the maps is presented. For the rest of the integrated intensity maps, see Appendix B.1. The kinematic analysis will be presented in an upcoming paper (Chacón-Tanarro et al., in prep., Paper II).

- CH_3OH and CH_2DOH

  In Fig. 3.2, the integrated intensity map of the transitions A^+ ($2_{0,2}$-$1_{0,1}$) of methanol and ($2_{0,2}$-$1_{0,1}$) and ($3_{0,3}$-$2_{0,2}$) of deuterated methanol are shown. Methanol, as previously reported, shows an asymmetric ring-like structure around the center of the core peaking toward the north-east at a distance of 4000 au.The asymmetric distribution and the faint emission towards the South was already noticed by Spezzano et al. (2016), who showed that the H_2 column density has a sharp drop toward the Southern part of the core, where in fact photoprocesses dominate. The peak of CH_2DOH map extends toward the dust peak, suggesting that deuterated methanol may trace a higher density zone compared to the main isotopologue. We note that the clumpiness seen in the CH_2DOH ($2_{0,2}$-$1_{0,1}$) map is due to noise (the noise in the integrated intensity is 0.005 $\mathrm{K\,km\,s^{-1}}$), and that the distribution of CH_2DOH is better seen with the map of the ($3_{0,3}$-$2_{0,2}$) line.

- H_2CO, $H_2\,^{13}CO$, HDCO and D_2CO

  The integrated intensity maps of $H_2\,^{13}CO$ ($2_{1,2}$-$1_{1,1}$), HDCO ($2_{1,1}$-$1_{1,0}$) and D_2CO ($2_{1,2}$-$1_{1,1}$) are shown in Fig. 3.3, and the integrated intensity map of H_2CO ($2_{1,2}$-$1_{1,1}$) is shown in Fig. B.2. The H_2CO line is asymmetric and double-peaked, with the blue peak stronger than the red peak (see Fig. 3.1), suggestive of contraction motions, as already seen by Tafalla et al. (1998) and Bacmann et al. (2003). The $H_2\,^{13}CO$ ($2_{1,2}$-$1_{1,1}$) line matches with the absorption dip from the H_2CO ($2_{1,2}$-$1_{1,1}$) line, indicating that this feature is indeed due to self-absorption (see Fig. 3.1). Thus, the distribution of formaldehyde is better traced by $H_2\,^{13}CO$, which also presents a ring-like structure around the core center, with a peak close to the methanol peak and, unlike CH_3OH, a secondary maximum toward the South. However, HDCO and D_2CO show centrally concentrated emission, differing from CH_3OH, CH_2DOH and H_2CO.

- $C^{17}O$

  The integrated intensity of $C^{17}O$ (1-0) is shown in Fig. 3.4. For the integrated intensity and the column density of $C^{17}O$, only the isolated component of the hyperfine structure ($F=\frac{5}{2}$-$\frac{5}{2}$) is used. The distribution of $C^{17}O$ looks similar to the previous map presented by Caselli et al. (1999), although here the emission peak is more pronounced and the distribution is clumpier. These differences are caused by the different mapping methods, as Caselli et al. (1999) only observed selected points while

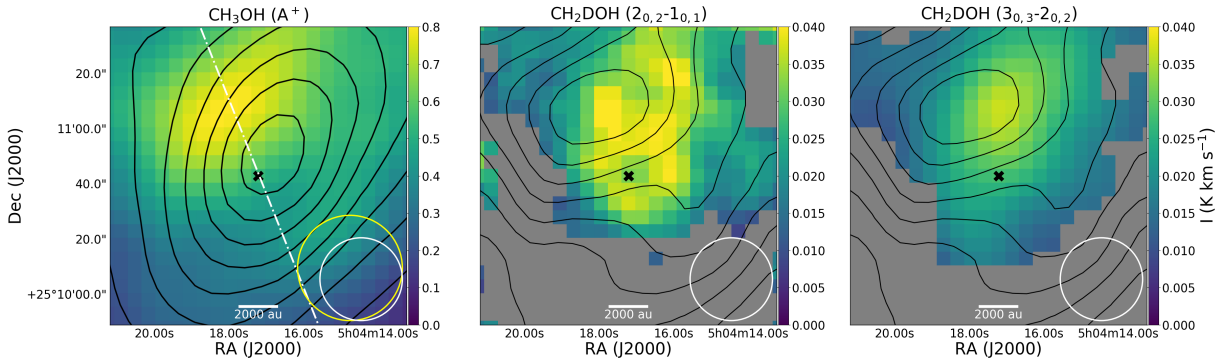

Figure 3.2: *Left panel:* integrated intensity map of the strongest methanol transition observed ($2_{0,2}$-$1_{0,1}$, A^+). The black contours represent increasing 10% steps of the N_{H_2} column density map, derived by Spezzano et al. (2016) using Herschel/SPIRE data. The noise in the integrated intensity is 0.02 K km s^{-1}. The white dashed-dotted line indicates the cut used for comparison with the models (see Section 3.6). *Middle panel:* integrated intensity map of the deuterated methanol ($2_{0,2}$-$1_{0,1}$) transition. The black contours represent increasing 10% steps of the CH_3OH column density map, derived as explained in Section 3.5.1. The error in the integrated intensity is 0.005 K km s^{-1}. *Right panel:* integrated intensity map of the deuterated methanol ($3_{0,3}$-$2_{0,2}$) transition. The black contours represent increasing 10% steps of the CH_3OH column density map, derived as explained in Section 3.5.1. The error in the integrated intensity is 0.004 K km s^{-1}. In all panels the HPBWs are shown in the bottom right corner of the figure, in yellow for *Herschel*/SPIRE and in white for the 30 m telescope, the black cross marks the dust continuum peak and only pixels with detection level above 3σ are included.

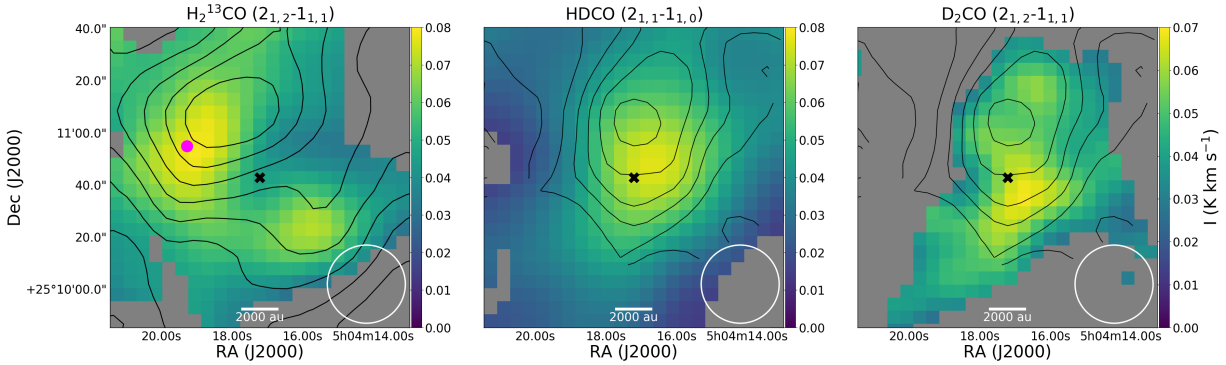

Figure 3.3: *Left panel:* integrated intensity map of $H_2\,^{13}CO$ ($2_{2,1}$-$1_{1,1}$). The error in the integrated intensity is 0.01 K km s^{-1}. The black contours represent increasing 10% steps of the CH_3OH column density map, derived as explained in Section 3.5.1. The pink circle marks the $C^{17}O$ peak (see also Fig. 3.4). *Middle panel:* integrated intensity maps of HDCO ($2_{1,1}$-$1_{1,0}$). The error in the integrated intensity is 0.005 K km s^{-1}. The black contours represent 10% steps with respect to the deuterated methanol column density peak. *Right panel:* integrated intensity map of D_2CO ($2_{1,2}$-$1_{1,1}$). The error in the integrated intensity is 0.01 K km s^{-1}. The black contours represent 10% steps with respect to the deuterated methanol column density peak. In all panels, the HPBW is shown in the bottom right corners, and the black cross marks the dust continuum peak. Only pixels with detection level above 3σ are included.

we carried out on-the-fly mapping of a more extended region. Interestingly, the emission peak coincides with the peak seen in $H_2\,^{13}CO$, as shown in Fig. 3.3. We point out that the $C^{17}O$ (1-0) transition is optically thin across the core, as already found by Caselli et al. (1999); this can also be seen from Fig. 3.1, where the relative intensities of the hyperfine components have been indicated below the observed spectrum.

3.5 Analysis

3.5.1 Column densities

All the column densities (see Section 3.6.1 for H_2CO) were derived assuming optically thin emission, so the following equation was used (Caselli et al. 2002b):

$$N = \frac{8\pi\nu^3}{c^3}\frac{Q(T_{ex})}{g_u A_{ul}}\left[J_\nu(T_{ex}) - J_\nu(T_{bg})\right]^{-1}\frac{e^{\frac{E_u}{kT_{ex}}}}{e^{\frac{h\nu}{kT_{ex}}}-1}\int T_{mb}\mathrm{d}v, \tag{3.1}$$

$Q(T_{ex})$ being the partition function of the molecule at an excitation temperature T_{ex}, g_u the rotational degeneracy of the upper level, $J_\nu(T)$ the Rayleigh-Jeans Equivalent Temperature at the frequency ν and temperature T, and T_{bg} the temperature of the background, here the cosmic background (2.7 K).

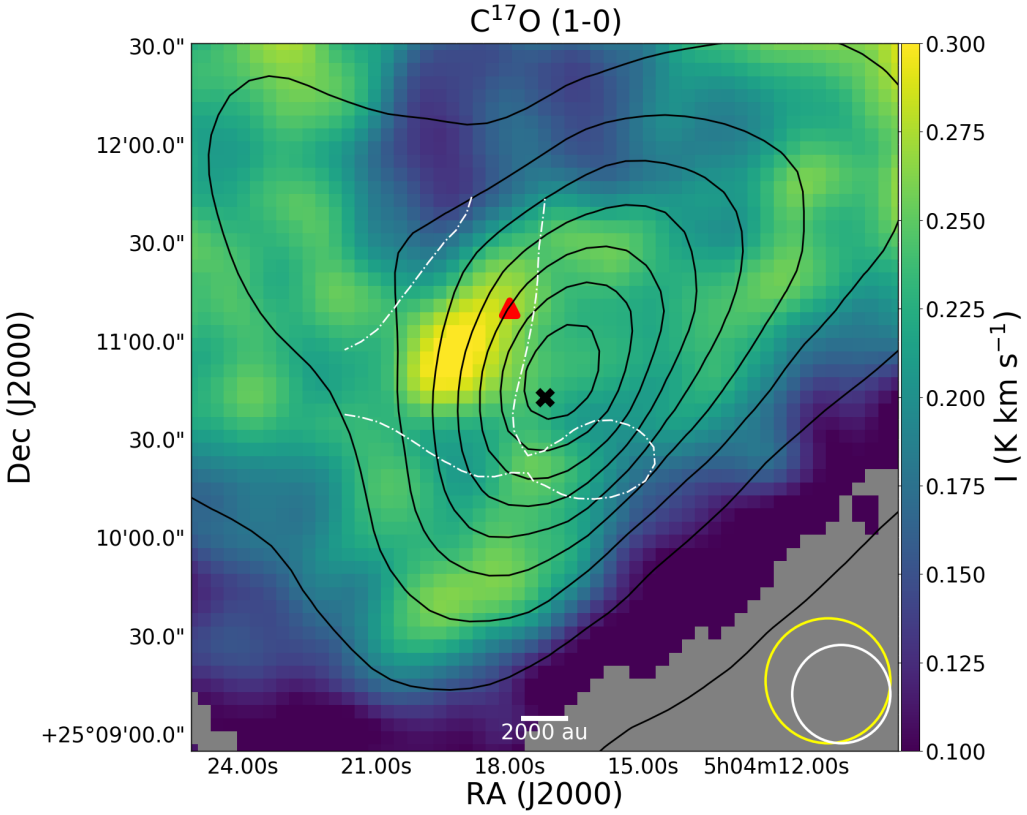

Figure 3.4: Integrated intensity map of the $C^{17}O$ (1-0) line. The error in the integrated intensity is 0.02 K km s^{-1}. The black contours represent increasing 10% steps of the peak of the Herschel $N(H_2)$ map, presented by Spezzano et al. (2016) and the white dash-dotted contour shows the 70% level of the H_2 ^{13}CO ($2_{2,1}$-$1_{1,1}$) column density map, derived as explained in Section 3.5.1. The HPBWs are shown in the bottom right corner, in yellow for *Herschel*/SPIRE and in white for the 30 m telescope. The black cross marks the dust continuum peak and the red triangle marks the methanol peak.

Bizzocchi et al. (2014) obtained an excitation temperature for methanol of $T_{ex} = 6 \pm 3$ K, and derived the column density of deuterated methanol averaging the results for three different excitation temperatures within the same temperature range: 5, 6.5 and 8 K. The excitation temperature of CH_2DOH cannot be derived because only two transitions were observed. Therefore, they calculated three column densities for CH_2DOH using the three excitation temperatures to have an estimate of the uncertainty. Similarly, we derive the column density for both deuterated methanol lines assuming those three different excitation temperatures and averaging all the resulting column densities for the two lines. For methanol, the column density was derived in the same way using the two strongest lines observed (A^+ and E_2). Bizzocchi et al. (2014) derived an optical depth of $\tau<0.4$, and already demonstrated that considering optical depth effects does not vary significantly the resulting column density; thus, the assumption of optically thin emission is justified.

The values found for the column densities of CH_2DOH and CH_3OH are slightly higher than those found by Bizzocchi et al. (2014), but are within a factor of 2. The maps of CH_3OH presented here are a factor of 3-20 noisier than the observations presented by Bizzocchi et al. (2014), due to the higher spectral resolution of these new maps. This can cause the difference seen in column densities. Nevertheless, the signal-to-noise ratio in these new maps is above 3σ in the whole map for the two lines studied here, being $>20\sigma$ towards the methanol peak.

For $C^{17}O$, the column density was derived assuming optically thin emission and a constant temperature of 10 K across the core. This temperature is based on Caselli et al. (1999), who obtained an excitation temperature of 10 K combining the emission of $C^{17}O$ (1-0) and (2-1). The hyperfine structure was fitted to check possible optical-depth effects, finding a good match with the optically thin emission assumption, as previously reported by Caselli et al. (1999).

In the case of $H_2\,^{13}CO$, HDCO and D_2CO, a constant temperature of 7 K was used. This temperature comes from the modeling done for H_2CO (see Section 3.6.1), and is in agreement with that used by Bacmann et al. (2003). The line D_2CO ($2_{1,2}$-$1_{1,1}$) is due to para species, so to obtain the total column density of D_2CO, the corresponding energies, degeneracy and the total partition function were used assuming an ortho-to-para ratio of 2:1. This same procedure was applied to $H_2\,^{13}CO$ ($2_{1,2}$-$1_{1,1}$), which is due to ortho species, assuming and ortho-to-para ratio of 3:1. The column density map of $H_2\,^{13}CO$ is used to derive a column density map of H_2CO assuming $[^{12}C]/[^{13}C] = 77$ (Wilson & Rood 1994).

All this information, together with the spectroscopic parameters used in the column density derivations, are summarized in Table 3.2. The resulting column density maps can be found in Appendix B.2. Here we only present the values at the dust and methanol peaks shown in Table 3.3. We remark that in this table the value for the column density of H_2CO is the one derived in Section 3.6.1.

We note that the excitation conditions of the different molecules are similar, and therefore, the errors associated with the assumptions of the above excitation temperatures are within the errors associated with the noise of the data. This can also be seen from the error of the column densities of CH_2DOH and CH_3OH (see Table 3.3). These errors have been derived from the maximum spread of values found for the three different excitation

Table 3.2: Parameters used in the derivation of the column densities: excitation temperature and the corresponding partition function, the energy of the upper levels of the transitions relative to the ground states, the Einstein coefficients and the degeneracy of the upper levels. For the case of $C^{17}O$, these parameters correspond to the isolated hyperfine component. The references for these spectroscopic parameters can be found in Table 3.1.

Line	T_{ex} (K)	$Q(T_{ex})$	E_u/k_b (K)	A (10^{-5} s^{-1})	g_u
CH_3OH (A^+)	5, 6.5, 8	5.46, 10.09, 15.37	6.96	0.34	5
CH_3OH (E_2)	5, 6.5, 8	5.46, 10.09, 15.37	12.53	0.256	5
CH_2DOH ($2_{0,2}$-$1_{0,1}$)	5, 6.5, 8	9.60, 15.25, 22.45	6.40	0.202	5
CH_2DOH ($3_{0,3}$-$2_{0,2}$)	5, 6.5, 8	9.60, 15.25, 22.45	12.83	0.730	7
$H_2\,^{13}CO$ ($2_{1,2}$-$1_{1,1}$)	7	8.95	21.72	4.931	15
HDCO ($2_{1,1}$-$1_{1,0}$)	7	7.67	12.23	4.591	5
D_2CO ($2_{1,2}$-$1_{1,1}$)	7	15.64	13.37	2.583	5
$C^{17}O$ (1-0)	10	24.37	5.39	0.0067	6

temperatures and the two lines used for each species. The adopted assumption on the excitation temperature does not bias significantly our results, because said errors are $\lesssim$25% of the column density values.

3.5.2 Deuterium fraction

CH_2DOH/CH_3OH

The deuterium fraction map of methanol was obtained by taking the ratio between the column density of CH_2DOH and that of CH_3OH. As seen in Fig. 3.5, it shows a non symmetric distribution peaking toward the south but close to the dust peak, especially when the beam size is taken into account. The peak value, $\sim$0.08$\pm$0.02, is consistent with that found by Bizzocchi et al. (2014) toward the core center.

H_2CO, HDCO and D_2CO

The deuterium fraction maps of formaldehyde are shown in Fig. 3.6. They are derived using the column density maps of HDCO, D_2CO and H_2CO. The H_2CO, as commented previously, is derived from the map of the optically thin emission of $H_2\,^{13}CO$. The maps show that the deuteration of formaldehyde also occurs in the central regions of the core. However, this needs more sensitive observations because of the large uncertainties, which can be seen in Fig. B.10. Thus, no information regarding the distribution can be obtained. The values at the dust peak are: [HDCO]/[H_2CO]$\simeq$0.03$\pm$0.02 and [D_2CO]/[H_2CO]$\simeq$0.04$\pm$0.03.

The map of the [D_2CO]/[HDCO] ratio shows a very high level of deuteration, with a mean value of $\sim$1.2$\pm$0.3. As previously mentioned, any variation of the deuteration across the map is not significant due to the high errors in its determination (see Fig. B.10).

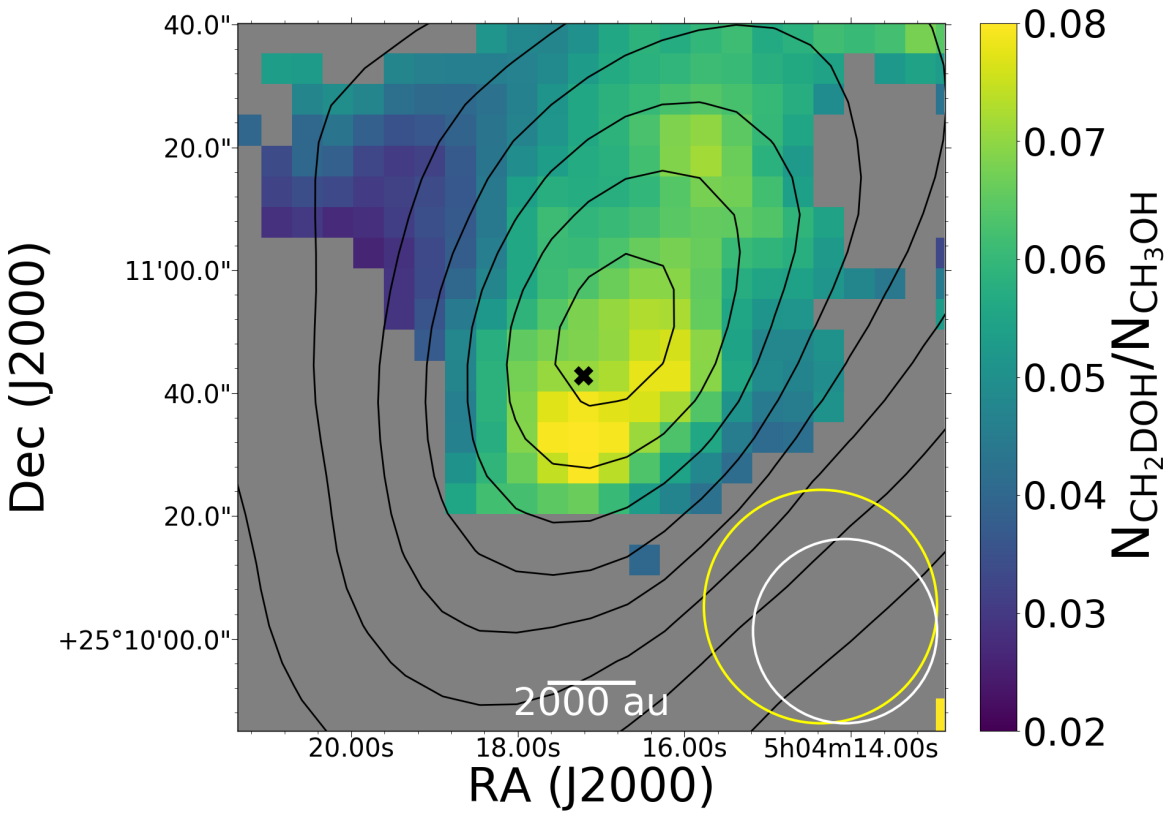

Figure 3.5: Deuterium fraction map of methanol using the column density maps of CH_2DOH and CH_3OH derived as described in Section 3.5.1. The black contours represent increasing 10% steps of the peak of the Herschel $N(H_2)$ map, presented by Spezzano et al. (2016). The HPBWs are shown in the bottom right corners of the figures, in yellow for *Herschel*/SPIRE and in white for the 30m telescope. The black cross marks the dust continuum peak, and only values above the 3σ detection level are considered.

Table 3.3: Column densities of the molecules observed. The value derived for H_2CO comes from the average between the results of two radiative transfer models, as described in Section 3.6.1, and the error is the difference between both values.

Line	$N_{\text{Dust peak}}$ (10^{12} cm^{-2})	$N_{\text{Methanol peak}}$ (10^{12} cm^{-2})
CH_3OH	39 ± 4	59 ± 6
CH_2DOH	2.8 ± 0.7	3.3 ± 0.8
H_2CO	9 ± 2	7 ± 3
$H_2\,^{13}CO$	0.54 ± 0.35	0.78 ± 0.35
HDCO	1.30 ± 0.09	0.96 ± 0.09
D_2CO	1.5 ± 0.3	1.1 ± 0.3
$C^{17}O$	680 ± 60	810 ± 60

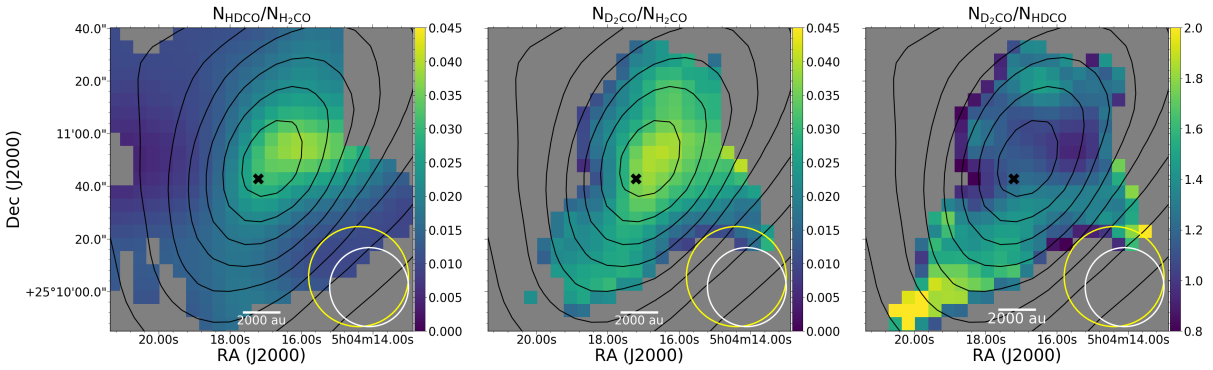

Figure 3.6: *Left panel*, [HDCO]/[H_2CO] map using the column density maps of HDCO and H_2CO derived as described in Section 3.5.1. *Middle panel*, map of the ratio [D_2CO]/[H_2CO], using the column density maps of D_2CO and H_2CO derived as described in Section 3.5.1. *Right panel*, map of the ratio [D_2CO]/[HDCO], using the column density maps of HDCO and D_2CO derived as described in Section 3.5.1. In all panels, the black contours represent increasing 10% steps of the peak of the Herschel N(H_2) map, presented by Spezzano et al. (2016). The HPBWs are shown in the bottom right corners of the figures, in yellow for *Herschel*/SPIRE and in white for the 30m telescope. The black cross marks the dust continuum peak, and only values above the 3σ detection level are considered.

3.6 Comparison with models

In this section, observational and theoretical results are compared. Here we present two different chemical models applied to L1544, and use them to compare the modeled column densities with the observed ones and to estimate the H_2CO column density. The two chemical models used are:

- **S16:** In this case the abundances of $C^{17}O$, CH_3OH, CH_2DOH, H_2CO, HDCO, and D_2CO were calculated using the chemical model presented in Sipilä et al. (2015a,b), which includes extensive descriptions of deuterium and spin-state chemistry. The modeling process was similar to that discussed in Sipilä et al. (2016), i.e. we divided the L1544 core model presented by Keto & Caselli (2010; see also Keto et al. 2014) into concentric shells, calculated the chemistry separately in each shell, and extracted the abundance gradients of the various species at several time steps. The model uses a bulk ice model, and it includes a fixed reactive desorption efficiency. The results shown in Figs. 3.7, 3.8, 3.9, 3.10 and 3.11 correspond to the time when the CO column density is comparable to the observed value in L1544 (Caselli et al. 1999).

- **V17:** The model of the pre-stellar core L1544 by Vasyunin et al. (2017) utilized static 1D distributions of gas density, gas and dust temperatures from Keto et al. (2014). The model includes time-dependent description of gas and grain chemistry based on Vasyunin & Herbst (2013) with several major updates concerning new gas-phase reactions important for the formation of complex organic molecules in the cold gas, as well as the detailed treatment of the efficiency of reactive desorption based on experimental works by Minissale et al. (2016). Treatment of chemistry on interstellar grains is based on a multilayer approach to the structure of icy mantles, which allows to discriminate between the reactive surface of ice and more chemically inert ice bulk. Since the temperature in L1544 is $\sim$10 K, the only important source of mobility of species on ice surfaces is quantum tunneling, which is enabled for H and H_2.

Both H_2CO and CH_3OH in the models are produced on the surface in the hydrogenation sequence of CO:

$$CO \rightarrow HCO \rightarrow H_2CO \rightarrow CH_2OH \rightarrow CH_3OH$$

However, while surface route is the only efficient way of formation for CH_3OH, H_2CO is also formed efficiently in the gas-phase reaction

$$O + CH_3 \rightarrow H_2CO + H.$$

In summary, both models use the same physical cloud structure, do not follow the evolution of the density and temperature of the cloud with time (here called static models), and adopt the same chemical reactions. However, the S16 model uses a bulk ice model with a fixed reactive desorption efficiency, it includes deuterated species, allows diffusion of light species via thermal hopping, and starts its chemistry from atomic initial abundances.

Meanwhile, V17 does not include deuterated isotopologues, but uses a multilayer approach for the ices with an updated treatment of the reactive desorption efficiency, and also allows hydrogen atoms and molecules to quantum tunnel on the grain surfaces, which facilitates the formation of methanol and other complex organic molecules (COMs). Moreover, this model assumes the evolved chemistry of diffuse clouds as initial conditions. However, different initial conditions do not play a role in the different results concerning methanol; the differences here can solely be ascribed to the different diffusion mechanisms of H on the surface, with V17 allowing quantum tunneling and S16 allowing the significantly slower thermal hopping. The comparison between models is important to check the dominant processes in the formation of COMs.

3.6.1 Deriving the column density of H_2CO

As already stated, H_2CO presents signatures of self-absorption, so one cannot apply the Equation (3.1) and the assumption of optical thinness to this molecule. Thus, we intended to model the emission at the center of the core via radiative transfer modeling using MOLLIE (Keto & Rybicki 2010), the physical model for L1544 from Keto et al. (2015), and the abundances profiles obtained from S16 and V17. The resulting column densities from MOLLIE are smoothed with a 30″ beam to match the resolution of the observations. This procedure was only used for comparing the column density derived from modeling with that observed, derived from the $H_2\,^{13}CO$ line.

We found that both abundance profiles overestimated the emission by a factor of ∼3 (see Fig. 3.7). Thus, we scaled the abundance profiles to reproduce the observed peak emission. The scaling factor applied to the abundance profile of V17 was 166, while the abundance profile from S16 needed to be reduced by a factor 220. The fact that the abundances had to be reduced by such large factors is due to the high optical depth of the line. The resulting modeled column densities can be found in Table 3.3. The excitation temperature obtained in both cases was of ∼7 K in the central 0.1 pc, and this value has been adopted as the temperature used for the derivation of the HDCO, D_2CO and $H_2\,^{13}CO$ column densities. At the center of the core, the column density of H_2CO derived from $H_2\,^{13}CO$ is a factor of 5 higher than the column density derived here using MOLLIE. This difference is below 2σ, once the uncertainties are taken into account.

The abundance reduction produces a change in the line profile, which now does not show the observed double peaked asymmetry any longer (see Fig. 3.7). One explanation is that the models do not take into account the presence of a lower density molecular material surrounding the core, where H_2CO can be present and participate in the line absorption. The ones presented here are therefore only approximate estimates of the column density, and although they are not far from the observations, more detailed work (i.e. larger scale mapping of H_2CO) is needed to fully understand from which layer of the cloud the formaldehyde emission is coming from.

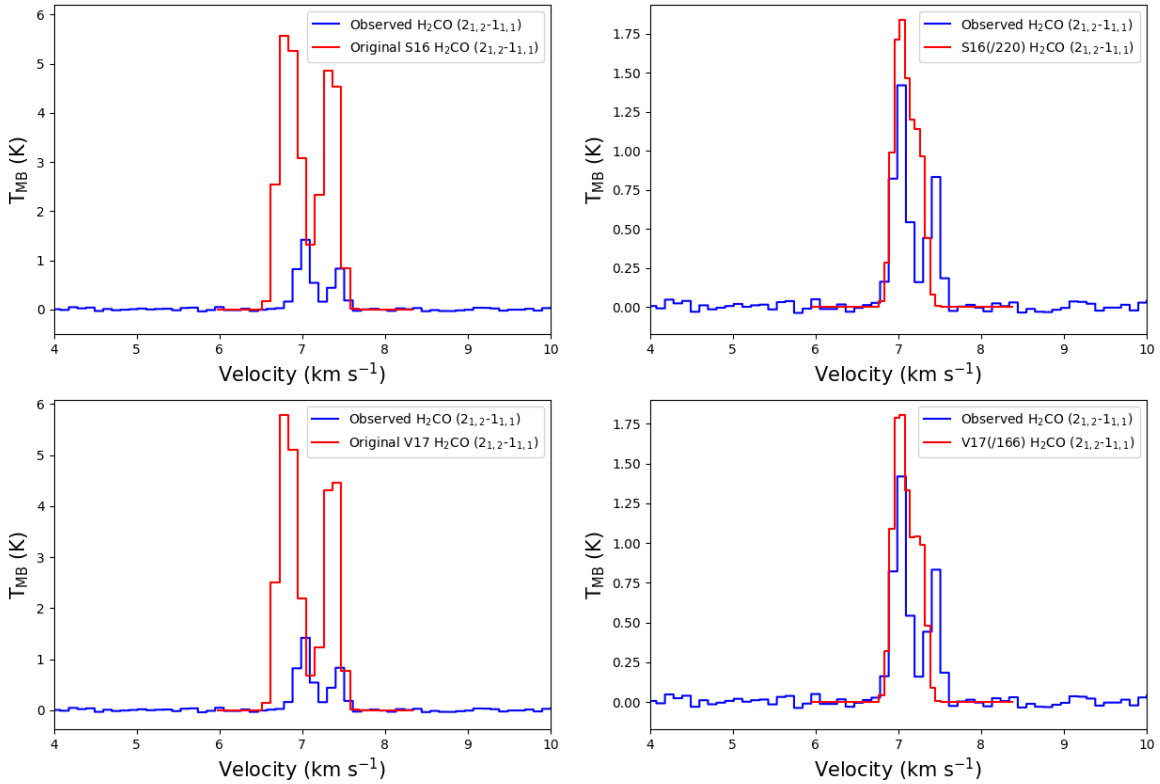

Figure 3.7: Comparison of the emission modeled by MOLLIE (in red, see Section 3.6.1) and the observed emission (in blue) of the H_2CO transition observed at the center of the core. *Top panels:* results using S16 abundance profile (*left panel*), and the same scaled by a factor of 220 (*right panel*). *Bottom panels:* results using V17 abundance profile (*left panel*), and the same scaled by a factor of 166 (*right panel*). The original abundance profiles overestimate the emission of the line by a factor of ∼3, and the scaled abundance profiles do not reproduce the shape of the line.

3.6.2 Modeled vs. observed column densities

In this section, the column densities observed are compared with the results from the V17 and S16 models. The V17 model does not include deuterated species so, in this case, the modeled column densities of deuterated species were derived using the column density of their corresponding isotopologue and the deuteration ratio from S16.

The results can be found in Fig. 3.8 for methanol and deuterated methanol and in Fig. 3.9 for single and doubly deuterated formaldehyde (we note the scaling factor applied to the models in some figures, indicated in the legend). The observed column densities are those corresponding to a cut done in the maps, which follows the white dashed line showed in Fig. 3.2. This cut is the same as the one studied by Spezzano et al. (2016) who considered the variation of the methanol column density from the methanol peak to the dust peak.

We point out that the same conclusions are reached if the cut orientation is changed, as the methanol column density changes by a factor of a few around the asymmetric ring, while the difference with the model prediction is larger than one order of magnitude.

Methanol and deuterated methanol are overestimated in the model from V17, and underestimated by S16. The overproduction of CH_3OH in V17, which was already noticed by the authors, can be due to an overestimation of the efficiency of reactive desorption. Moreover, as explained in V17, this model does not efficiently form CO_2 because of the activation energy of the CO+OH reaction (Ruffle & Herbst 2001), which does not proceed at T<20 K (Vasyunin et al. 2017), so in warmer environments, one would expect to have a significant fraction of CO producing CO_2 instead of methanol. CO_2 is also abundant and ubiquitous in quiescent dense clouds (Whittet et al. 1998; Boogert et al. 2015); however, in these cold regions, CO_2 is expected to form via energetic processing of water ice mantles onto carbonaceous grains (see e.g. Mennella et al. 2004, 2006), and this process has not been included in any gas-grain chemical model yet. In any case, we note that a factor of 10 difference between model and observations can be considered to be in fair agreement, due to the large uncertainties of gas-grain models, which can go up to one order of magnitude (Vasyunin et al. 2004, 2008). The underproduction in S16 is most likely caused by the fact that hydrogen atoms are not allowed to quantum tunnel across the grain surface, thus significantly reducing surface hydrogenation and the consequent production of CH_3OH.

The measured column density of methanol is closer to the V17 predictions, whereas deuterated methanol is closer to S16. One has to take into account that for the models, the deuterium fraction was taken from S16, which overestimates the deuteration of methanol by a factor of 10 (see Fig. 3.10). If the observed deuterium fraction ($\sim$0.1) is applied to the models, the difference between observations and both models is similar.

In the case of formaldehyde, both models overproduce H_2CO. For its deuteration, S16 model predicts [HDCO]/[H_2CO] $\sim$0.013, and [D_2CO]/[H_2CO] a factor of 100 smaller (see Fig. 3.11). However, observationally, we found a value of $\sim$0.03$\pm$0.02 for [HDCO]/[H_2CO] and $\sim$0.04$\pm$0.03 for [D_2CO]/[H_2CO]. This means that while [HDCO]/[H_2CO] is well reproduced by the model, there is a difference of a factor of 100 between the observed [D_2CO]/[H_2CO] and the modeled ratio. Applying this observed factor to the modeled abundances of H_2CO would imply an overproduction of all the formaldehyde family (see Fig. 3.9).

Our results show that the production of these molecules is still uncertain in this core, and more work has to be done to better constrain the chemistry in pre-stellar cores.

3.7 Discussion

3.7.1 Distribution

The fact that deuterated methanol peaks closer to the core center compared to methanol can be simply explained by the larger D/H abundance, so that D atoms compete with H atoms in saturating solid CO. This central region is in fact characterized by large amount of

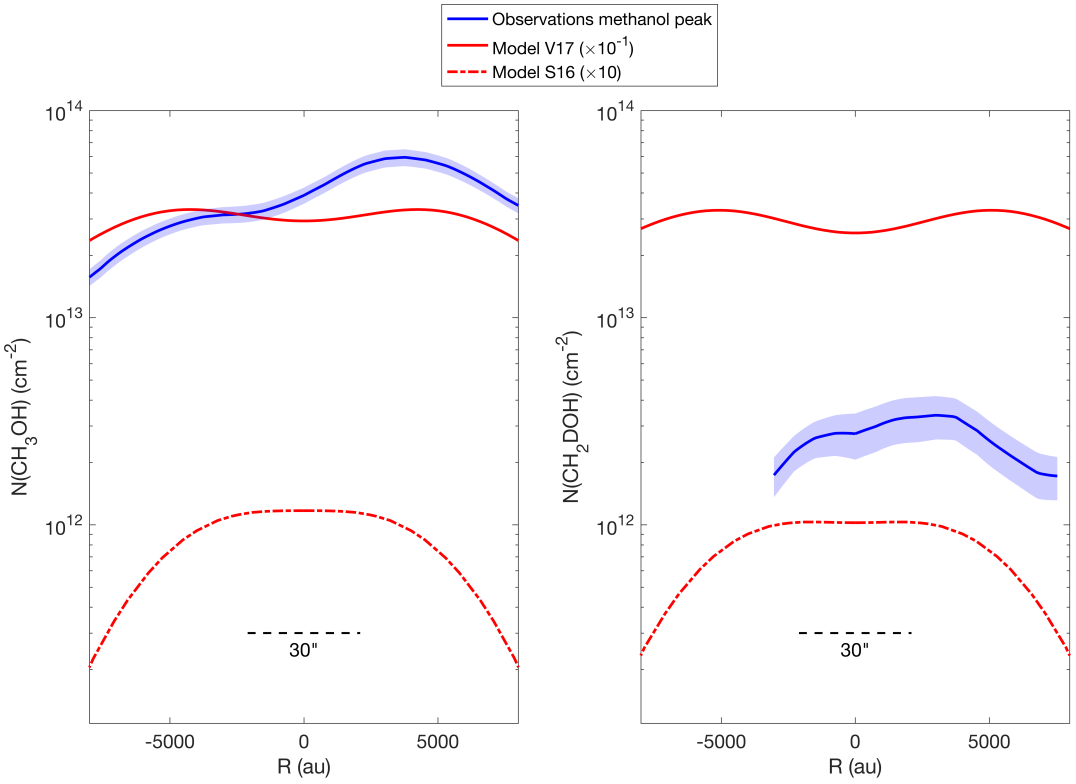

Figure 3.8: Comparison of the observed column densities (blue line) with the modeled column densities by V17 (red line) and S16 (red dashed line) of CH_3OH (*left panel*) and CH_2DOH (*right panel*). The observed column density profiles are taken along the white dashed line shown in Fig. 3.2, being R=0 au the dust peak, R>0 au the direction from dust peak to methanol peak, and R<0 au is the direction from the dust peak toward the south–west. The shaded blue regions indicate the error bars of the column densities. The resolution is 30″, shown at the bottom of the figure. Note the scaling factor applied to the models.

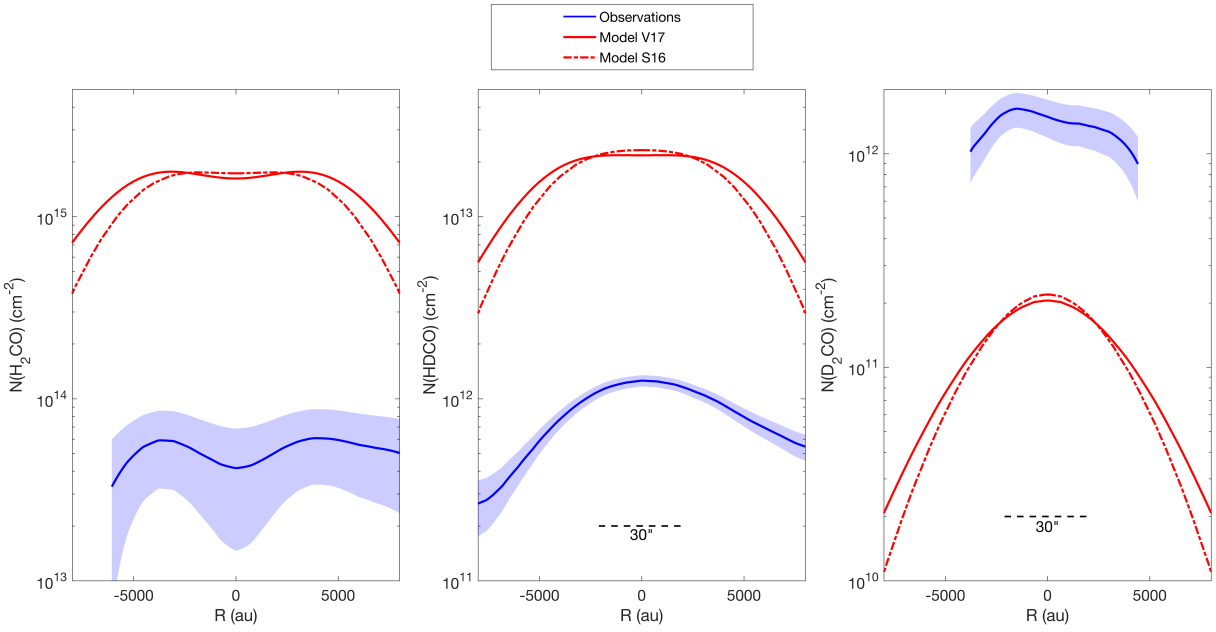

Figure 3.9: Comparison of the observed column densities (blue line) with the modeled column densities by V17 (red line) and S16 (red dashed line) of H_2CO (*left panel*), HDCO (*middle panel*) and D_2CO (*right panel*). The observed column density profiles are taken along the white dashed line shown in Fig. 3.2, being R=0 au the dust peak, R>0 au the direction from dust peak to methanol peak, and R<0 au is the direction from the dust peak toward the south–west. The shaded blue regions indicate the error bars of the column densities. The resolution is 30″, shown at the bottom of the figure.

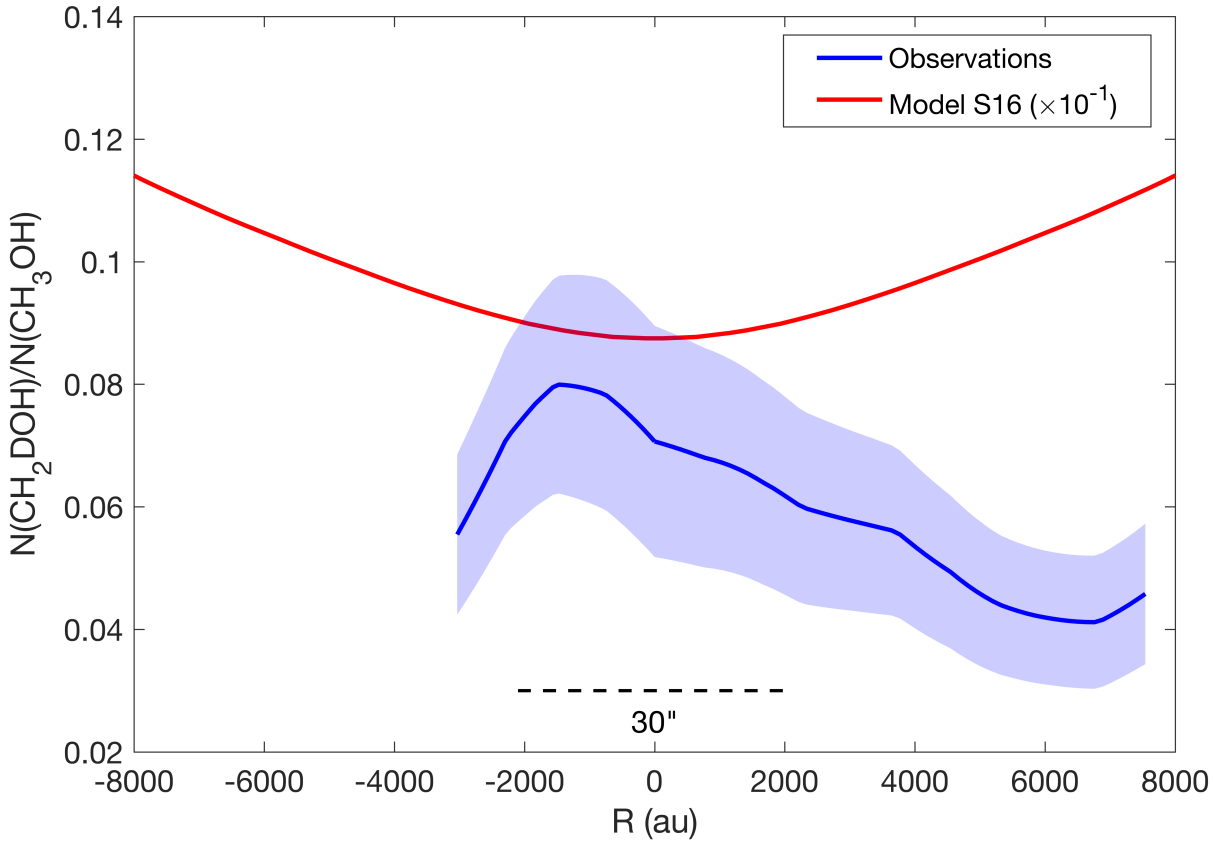

Figure 3.10: Comparison of the observed methanol deuterium fraction (blue line) with the modeled deuterium fraction by S16 (red line). The observed deuteration profile is taken along the white dashed line in Fig. 3.2, being R=0 au the dust peak, R>0 au the direction from dust peak to methanol peak, and R<0 au is the direction from the dust peak toward the south–west. The shaded blue region shows the error bars in the deuterium fractions. The resolution is 30″, shown at the bottom of the figure. Note the scaling factor applied to the model.

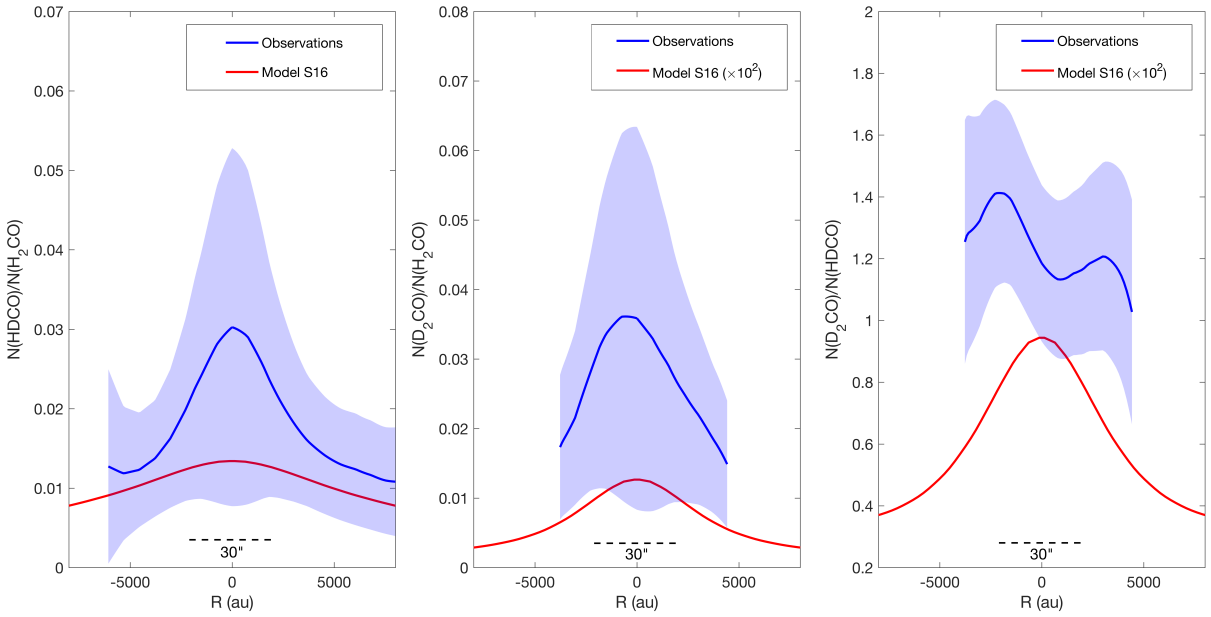

Figure 3.11: Comparison of the observed [HDCO]/[H_2CO] (*left panel*), [D_2CO]/[H_2CO] (*middle panel*) and [D_2CO]/[HDCO] (*right panel*) ratios (blue line) with the modeled deuterium fractions by S16 (red line). The observed deuteration profile is taken along the white dashed line in Fig. 3.2, being R=0 au the dust peak, R>0 au the direction from dust peak to methanol peak, and R<0 au is the direction from the dust peak toward the south–west. The shaded blue regions indicate the error bars in the deuterium fractions. The resolution is 30″, shown at the bottom of the figure. Note the scaling factor applied to the models.

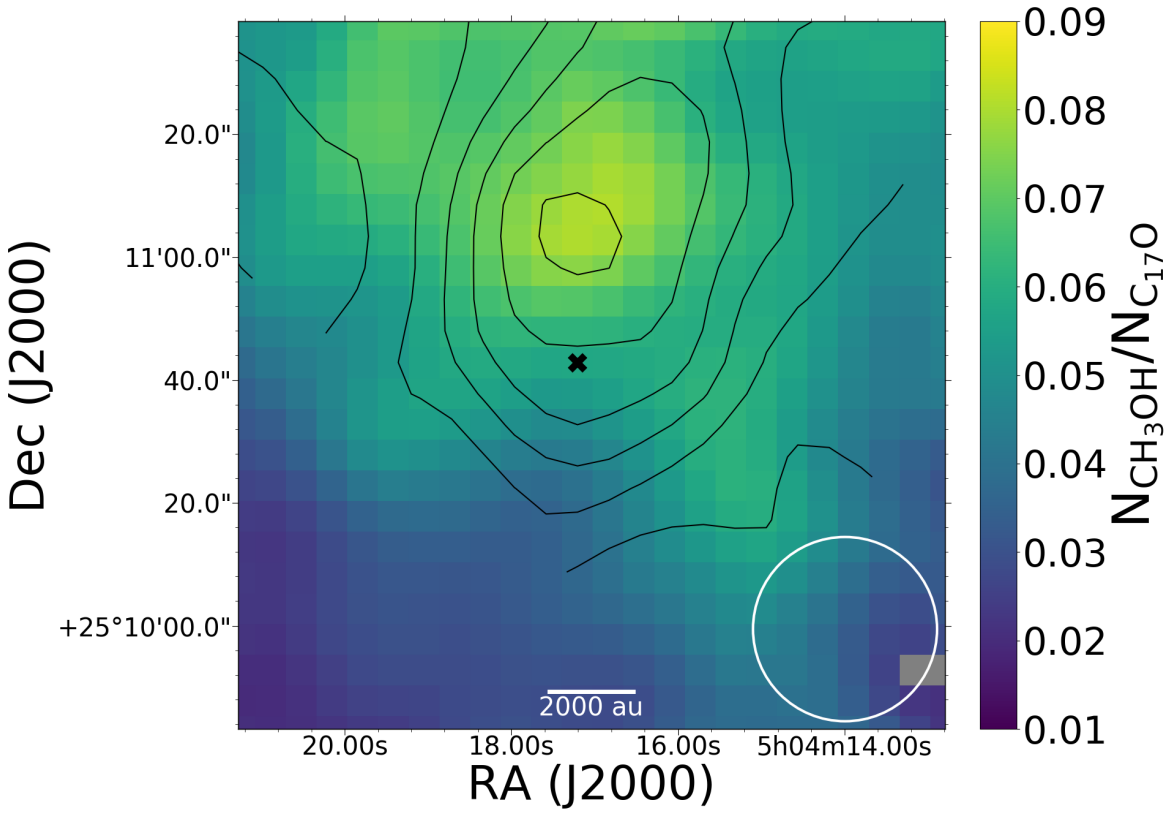

Figure 3.12: Ratio of the column densities of methanol and $C^{17}O$. The black contours represent 10% steps with respect to the deuterated methanol column density peak. The black cross marks the dust peak. The HPBW is shown in the bottom right corner. The black cross marks the dust continuum peak.

CO freeze-out (Caselli et al. 1999) and consequently large deuterium fractions (Caselli et al. 2002b, 2003; Crapsi et al. 2007), as predicted by theory (Dalgarno & Lepp 1984; Walmsley et al. 2004). This scenario is supported by the fact that deuterated methanol peaks exactly where the $N(CH_3OH)/N(CO)$ ratio is higher (see Fig. 3.12), and the deuterium fraction is enhanced where the CO is more depleted (see Fig. B.8). However, we note that the CH_2DOH/CH_3OH column density ratio never reaches values larger than 0.1, unlike $[N_2D^+]/[H_2H^+]$ and $[NH_2D]/[NH_3]$ (Crapsi et al. 2005, 2007). This suggests that deuterated methanol is probably tracing a more external layer than N_2D^+ and NH_3. This is analogous to the conclusion reached by Caselli et al. (2002b) to explain the $[DCO^+]/[HCO^+]$, since both DCO^+ and HCO^+ require gas-phase CO to form and CO are mainly frozen onto dust grains toward the core center, as already mentioned.

For formaldehyde, we find that it follows a slightly different distribution compared to

CH_3OH, interestingly peaking at the same place as $C^{17}O$ and showing a secondary peak toward the south–west part of the core, where the emission of $C^{17}O$ also shows a decrease. This can be explained by the fact that, unlike CH_3OH, H_2CO can also form via gas phase routes involving hydrocarbons (e.g. CH_2 and CH_3; Yamamoto 2017), which are expected to be abundant toward the southern part of the core, where the extinction abruptly drops to relatively low values and where carbon chains are in fact abundant (Spezzano et al. 2016; Ohashi et al. 1999).

The deuterated species of H_2CO both peak at the center of the core, which is not the case for deuterated methanol, as seen in Fig. 3.3. Their distributions follow that of other deuterated species as N_2D+ and NH_2D (Caselli et al. 2002b; Crapsi et al. 2007).

Interferometric observations are needed to make more detailed conclusions on possible differences in the distributions of the deuterated forms of methanol and formaldehyde, as the resolution and sensitivity of these observations do not allow us to discuss them in locations further than where their emission is enhanced.

3.7.2 Deuteration

Previous results for the deuterium fractions measured in L1544 show a wide range of values: $[N_2D^+]/[N_2H^+] = 0.2$, $[NH_2D]/[NH_3] = 0.5$, $[DCO^+]/[HCO^+] = 0.04$ and [c-C_3HD]/[c-C_3H_2] = 0.12-0.17 (Caselli et al. 2002b; Crapsi et al. 2007; Spezzano et al. 2013). The deuterium fraction of methanol (with a peak value of $\sim$0.08$\pm$0.02) is within this range, and lower than values found for more evolved Class 0 objects. This difference with more evolved objects can be due to the presence of a major reservoir of CH_2DOH in the ices in pre-stellar cores, which is released to the gas phase during the Class 0 phase (e.g. Parise et al. 2002, 2004). As already mentioned, the fact that the fractionation in N_2H^+ is larger just reflects that N_2D^+ and NH_2D trace regions closer to the center than those traced by CH_2DOH.

Similarly, we find that $[HDCO]/[H_2CO] \simeq 0.03 \pm 0.02$ and $[D_2CO]/[H_2CO] \simeq 0.04 \pm 0.03$ at the dust peak, which is consistent with previous values reported in pre-stellar cores and Class 0 objects (Bacmann et al. 2003; Parise et al. 2006). The value for $[D_2CO]/[H_2CO]$ is also consistent with that found by Bacmann et al. (2003). One thing to note is that, as in Bergman et al. (2011), we find a higher abundance of D_2CO than HDCO. Bergman et al. (2011) claimed that this can only be explained if grain chemistry is ongoing, although their results are applied to the region of Ophiuchus, and the chemistry can differ from cloud to cloud. However, these molecules can suffer from depletion, which can be the source of discrepancy in the deuterium fractionations between different species, more importantly when compared with those that do not suffer from depletion, like N_2D^+ and NH_3.

As seen in Section 3.6, the model predictions for the deuteration of methanol in L1544 is higher than those observed, while the opposite happens with D_2CO. The deuteration of formaldehyde is close to that of methanol if the uncertainties are taken into account. Thus, more theoretical work needs to be done to fully understand deuteration processes in pre-stellar cores.

3.8 Conclusions

We have presented our maps of methanol, formaldehyde and their deuterated species toward the well known pre-stellar core L1544. These two molecules can help us to gain understanding about the chemical processes taking place on the dust grain surfaces and the formation of more complex organic molecules, as well as the deuterium history in the process of star formation.

The highest level of deuteration of methanol occurs close to the dust peak, reaching $[CH_2DOH]/[CH_3OH] = 0.8$. This indicates that a more external layer is traced by CH_2DOH compared to N_2H^+ (Caselli et al. 2002a) and NH_3 (Crapsi et al. 2007). CH_2DOH also shows a higher abundance at a distance of ∼3000 au from the dust peak, exactly where more methanol is present in the gas phase with respect to CO. This suggests that deuterated methanol is formed and released the same way CH_3OH is.

HDCO and D_2CO, however, peak toward the center of the core, and present a high deuterium fraction, only found previously in ρ Oph A (Bergman et al. 2011). Interestingly, H_2CO shows a ring like structure, depleting towards the center, and showing two maxima, one coinciding with $C^{17}O$, and a secondary peak toward the South-West, unlike methanol, which coincides with a region where $C^{17}O$ shows less emission. This suggests that gas phase production via reactions involving hydrocarbons efficiently takes place in regions where C is not completely locked in CO.

Finally, we compared two different chemical models with our observational results, and did not find an agreement. On the one hand, the model from Vasyunin et al. (2017) is overproducing methanol and formaldehyde, probably caused by the overestimation of the efficiency of reactive desorption. On the other hand, the model from Sipilä et al. (2015a,b) does not produce enough methanol because of the slow diffusion of hydrogen atoms on the surfaces (which are not allowed to quantum tunnel) and it overproduces formaldehyde. Both models are static and the inclusion of dynamical evolution could change the results, although not by orders of magnitude, needed to reconcile models with observations. Our results suggest that quantum tunnelling for H diffusion on icy dust mantles should be considered, while reactive desorption still needs more detailed experimental work.

Higher sensitivity and angular resolution observations of the lines presented here are needed, together with a parameter-space exploration within current chemical models and laboratory work, to shed light on important chemical processes happening at the dawn of star formation.

Chapter 4

Dust opacity variations in the pre-stellar core L1544

This Chapter is based on: Chacón-Tanarro, A., Pineda, J. E., Caselli, P., Bizzocchi, L., Gutermuth, R. A., Mason, B. S., Gómez-Ruiz, A. I., Harju, J., Devlin, M., Dicker, S. R., Mroczkowski, T., Romero, C. E., Sievers, J., Stanchfield, S., and Offner, S., submitted to A&A on the 7th of May, 2018.

4.1 Abstract

Context. The study of dust emission at millimeter wavelengths is important to shed light on the dust properties and physical structure of pre-stellar cores, the initial conditions in the process of star and planet formation.

Aims. Using two new continuum facilities, AzTEC at the LMT and MUSTANG-2 at the GBO, we aim to detect changes in the optical properties of dust grains as a function of radius for the well-known pre-stellar core L1544.

Methods. We determine the emission profiles at 1.1 and 3.3 mm and examine whether they can be reproduced in terms of the current best physical models for L1544. We also make use of various tools to determine the radial distributions of the density, temperature, and the dust opacity in a self-consistent manner.

Results. We find that our observations cannot be reproduced without invoking opacity variations. With the new data, new temperature and density profiles, as well as opacity variations across the core, have been derived. The opacity changes are consistent with the expected variations between uncoagulated bare grains toward the outer regions of the core, and grains with thick ice mantles toward the core center. A simple analytical grain growth model predicts the presence of grains of ∼3-4 μm within the central 2 000 au for the new density profile.

4.2 Introduction

Pre-stellar cores are starless dense ($n_{\mathrm{H_2}} > 10^5$ cm^{-3}) and cold ($T < 10K$) self-gravitating cloud cores. They are formed from molecular cloud material, and present clear signs of contraction and chemical evolution (Crapsi et al. 2005). Since they are considered the initial conditions of star formation (Bergin & Tafalla 2007; Caselli & Ceccarelli 2012), these cores are important to understand the future evolution of protostars and protoplanetary disks (e.g. Zhao et al. 2016).

In this work we focus on the pre-stellar core L1544, which is placed in the Taurus Molecular Cloud, 140 pc away. It is a proto-typical example of a pre-stellar core, whose physical structure has been studied in the past. First, Tafalla et al. (2002) determined a density profile for the source using continuum emission at 1.3 mm, and a constant temperature of 8.75 K across the core. Later, Crapsi et al. (2007), using high resolution ammonia interferometric observations, found a drop in temperature towards the center of the core. This implied that the density profile found by Tafalla et al. (2002) needed to be modified. Finally, Keto et al. (2015) were able to reproduce molecular line and continuum observations of L1544 by describing it as a Bonnor-Ebert sphere (Bonnor 1956) in quasi-equilibrium contraction. However, Keto et al. (2015) found that to reproduce the temperature drop measured by Crapsi et al. (2007), they needed to increase the dust opacity. This could be an indication of the presence of fluffy grains, and therefore these results suggested that L1544 was the perfect target to study dust grain coagulation in pre-stellar cores.

The opacity, κ_ν, is a measurement of the dust absorption cross sections weighted by the mass of the gas and dust. It depends on the frequency, ν, and physical properties of the dust grains, such as composition, mass and size: if dust grains are much smaller than the wavelength at which they are observed, κ_ν depends on the mass of the grains; if they are larger than the observing wavelength, κ_ν decreases with the grain size. However, dust grains with size similar to the wavelength become very efficient radiators, increasing the opacity up to 10 times its typical value (Kruegel & Siebenmorgen 1994). Usually, matching the data with models requires an assumption regarding the opacity, and this translates into an assumption regarding the dust grain distribution and properties across the cloud.

Usually, in pre-stellar cores the values used for the opacities are taken from grain coagulation models from Ossenkopf & Henning (1994). Deviations from these values, as well as their dependence on temperature, are a matter of current debate. Recent laboratory work from Demyk et al. (2017) showed that for the temperature range typical for pre-stellar cores (10-30 K), the opacity does not depend on the temperature, although Agladze et al. (1996) detected an inverse relation for very low temperatures (<20 K). The opacity can be approximated by a power law at millimeter wavelengths, $\kappa_\nu \propto \nu^\beta$, where β is the spectral index of the dust. As shown by Demyk et al. (2017), for example, the power law slope (or β) seems to vary depending on the frequency range. Together with the possibility of grain coagulation in dense cores, these results indicate that many factors can modify the emission observed.

Observationally, previous studies have found variations in the opacity and the spectral index from molecular clouds to clumps and cores (see e.g., Sadavoy et al. 2016; Chen et al.

2016; Juvela et al. 2015a,b; Foster et al. 2013). Going to smaller scales, Forbrich et al. (2015) found opacity variations when studying the extinction map of the starless core FeSt 1-457, while Bracco et al. (2017) and Chacón-Tanarro et al. (2017) found no evidence of opacity and spectral index variations towards pre-stellar cores using the NIKA camera at the IRAM 30 m telescope. The observed variations can be attributed to grain growth towards dense clumps and cores, although other factors, such as the noise of the data or temperature dependence should be taken into account (Shetty et al. 2009a,b). In these dense regions, ice mantle growth and grain coagulation is expected to affect the emission of dust grains at submillimeter and milimeter wavelengths (Ormel et al. 2009, 2011). Thus, the opacity behavior in dense, cold pre-stellar cores remains debated and highly uncertain.

Here we present sensitive continuum maps observed with two new facilities for millimeter observations: AzTEC at the Large Millimeter Telescope Alfonso Serrano (LMT), observing at 1.1 mm, and MUSTANG-2 at the Green Bank Observatory (GBO), observing at 3.3 mm. These maps help us to understand the physical structure of the core, including new information on the behavior of the opacity towards L1544. This work presents the first continuum map of L1544 at 3.3 mm, and it improves the work done in Chacón-Tanarro et al. (2017), where data at 1.2 and 2 mm were available. This improvement is due to a better angular resolution and to the study of a wider wavelength range, which can better constrain the spectral index of the dust.

The Chapter is divided as follows: in Section 4.3 we describe the observations and data processing; the two new millimeter maps are presented in Section 4.4; in Section 4.5 we make a first attempt of checking opacity and spectral index variations following the ratio between both bands and trying to model the emission seen using constant spectral index and opacity values towards the core; in Section 4.6 we present a new model for the physical structure of L1544 using the observed opacity variations and discuss these new findings. We summarize our results in Section 4.7.

4.3 Observations

4.3.1 AzTEC

The data at 1.1 mm were obtained during the nights of February 22$^{\rm nd}$ and March 22$^{\rm nd}$ of 2016, at the Large Millimeter Telescope (LMT) Alfonso Serrano, placed at the volcano Sierra Negra, Mexico. The observations were carried out during the early science phase, when LMT had a diameter of 32 m. The opacity at 220 GHz at zenith ranged from 0.06-0.08, and the total integration time was 1.6 hours. L1544 was observed with the continuum camera AzTEC and using Rastajous Map Mode (Calzetti et al. 2018), with a field of view larger than $5'$ of diameter in size. The data reduction was done using the standard pipeline of AzTEC (Scott et al. 2008), with the implementation of the Cottingham method (Cottingham 1987) to better recover the large scale structure of the core (see Calzetti et al. 2018). The Cottingham method helps to remove the contamination from the atmosphere by modeling the temporal variations of the atmosphere signal using B-splines, and this is

done for each detector. This method is a maximum likelihood estimator for the emission coming from the atmosphere and the astronomical sources (Hincks et al. 2010).

The resulting map has a resolution of 12.6″ and an rms of 3 mJy/beam. The estimated calibration uncertainty is 10%.

4.3.2 MUSTANG-2

L1544 was observed at 3.3 mm during the nights of the 30$^{\text{th}}$ of December 2017, 3$^{\text{rd}}$ and 7$^{\text{th}}$ of January 2018, at the Green Bank Observatory (GBO; project GBT17B-174). The observations were carried out with the bolometer camera MUSTANG-2 (Dicker et al. 2014; Stanchfield et al. 2016), which has a field of view of 4.25′. The total on source integration time was 3.25 hours. The observations were done with the On-The-Fly (OTF) mapping mode (Mangum et al. 2007), using a daisy-petal scan pattern. This method allows frequent crossings to subtract the atmosphere and other systematics. To accomplish this subtraction, a median common mode and slowly varying per-detector polynomial (30 seconds timescale) is subtracted from the data, excluding the central region of the map from the polynomial fit.

The final map has an rms of 0.15 mJy/beam, with a beam size of 9.7″. The calibration uncertainty is 12%.

4.3.3 Matching PSF

The beam shape from MUSTANG-2 cannot be considered as Gaussian, in contrast to the beam of AzTEC. Therefore, in order to compare the two maps at the same resolution, we need to find a convolution kernel which transforms the PSF (Point Spread Function) of MUSTANG-2 to that of AzTEC. For this purpose, we made use of the Python library *photutils.psf.matching*. We modified the shape of the window and the parameter for tapering (to remove the high frequency noise) until the convolved MUSTANG-2 beam matched the AzTEC PSF.

4.3.4 *Herschel*/SPIRE

In Section 4.5.2, the *Herschel*/SPIRE maps of L1544 are used. They were presented by Spezzano et al. (2016) and are part of the *Herschel* Gould Belt Survey (André et al. 2010). As these SPIRE 250, 250 and 500 μm maps are used together with ground-based telescope maps, they are artificially filtered in order to account for the missing flux coming from the large scale structure of the cloud. For more details on these maps and the filtering process, see Chacón-Tanarro et al. (2017).

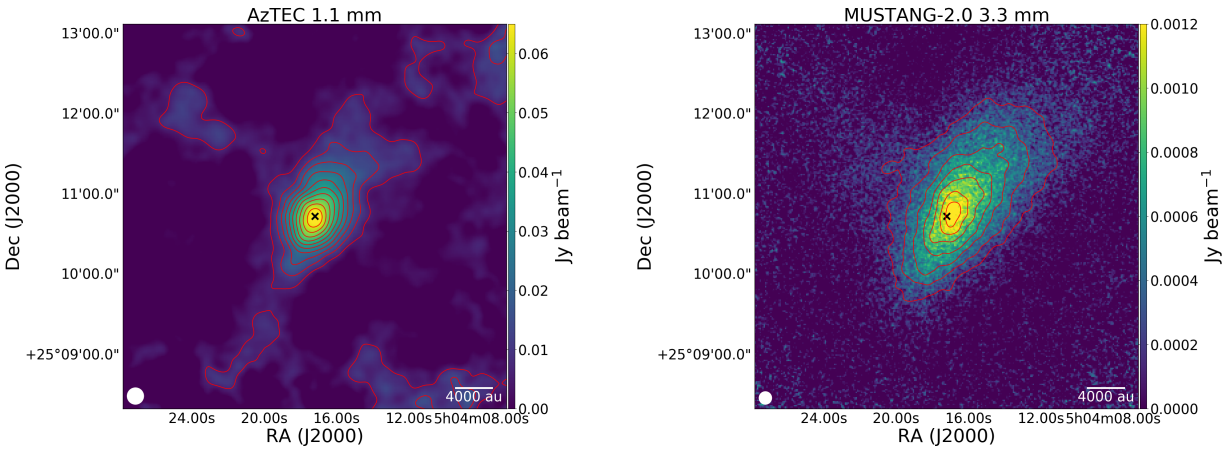

Figure 4.1: *Left panel:* AzTEC map at 1.1 mm. The contours represent steps of 2σ, starting from 2σ, with $\sigma = 3$ mJy/beam. The HPBW is shown in the bottom left corner, and the 1.3 mm dust continuum peak is shown with a black cross (Ward-Thompson et al. 1999). *Right panel:* MUSTANG-2 map at 3.3 mm. The contours represent steps of 2σ, starting from 2σ, with $\sigma = 0.15$ mJy/beam. The HPBW is shown in the bottom letf corner, and the 1.3 mm dust continuum peak is shown with a black cross (Ward-Thompson et al. 1999).

4.4 Results

Fig. 4.1 shows the final maps, at their intrinsic resolution. This is the first time that ground-based continuum observations hint at the detection of a filamentary structure or extended emission towards the north-east, which are clearly seen by *Herschel*/SPIRE (see Spezzano et al. 2016) and $C^{18}O$ maps (Tafalla et al. 1998).

4.5 Analysis

4.5.1 Spectral index and opacity maps

In pre-stellar cores the emission of the dust can be assumed to be optically thin at millimeter wavelengths, and it can be described by a modified black body function:

$$I_\nu = \mu_{\mathrm{H}_2} m_{\mathrm{H}} \int_{s_{los}} B_\nu[T_d(s)] n_{\mathrm{H}_2}(s) \kappa_\nu(s) \mathrm{d}s, \tag{4.1}$$

where I_ν is the intensity, $B_\nu[T_d(s)]$ the blackbody function at a temperature $T_d(s)$, $\kappa_\nu(s)$ the dust opacity at frequency ν, $\mu_{\mathrm{H}_2} = 2.8$ the molecular weight per hydrogen molecule (Kauffmann et al. 2008), m_{H} the mass of the hydrogen atom, $n_{\mathrm{H}_2}(s)$ the molecular hydrogen density, and s the line of sight depth. The dust opacity can be approximated by a power law at millimeter wavelengths (Hildebrand 1983): $\kappa_\nu = \kappa_{\nu_0} \left(\frac{\nu}{\nu_0}\right)^\beta$, where β is the spectral

index of the dust. Although laboratory studies have shown that this power law changes depending on the frequency range (e.g. Demyk et al. 2017), the study of the dependency of β with frequency is beyond the scope of this work.

If the density and the temperature profiles are known, the derivation of the spectral index and the opacity is straightforward with only data at two different frequencies. From Eq. (4.1), the spectral index can be derived from the ratio of the emission at both wavelengths, following:

$$\beta = \frac{\log(I_{1\mathrm{mm}}/I_{3\mathrm{mm}}) - \log(B_{1\mathrm{mm}}[T_\mathrm{d}]/B_{3\mathrm{mm}}[T_\mathrm{d}])}{\log(\nu_{1\mathrm{mm}}/\nu_{3\mathrm{mm}})}, \tag{4.2}$$

where the sub-indexes 1 mm and 3 mm denote the band at which the intensity, black body emission and frequency are being evaluated. The opacity can be derived from any of the wavelengths observed using Eq. (4.1). A dust-to-gas ratio of 0.01 is assumed here. Although this ratio shows variations between different regions of our galaxy (Draine 2011), we do not expect them to be significant within the same cloud.

Our first analysis of the new data follows the methodology presented by Chacón-Tanarro et al. (2017), where the temperature and density profiles from Keto et al. (2015) were used to derive the spectral index and the opacity following Eqs. (4.1) and (4.2). Keto et al. (2015) deduced the physical model of L1544 by following the evolution of an unstable Bonnor-Ebert sphere in quasi-equilibrium contraction and comparing, via radiative transfer modeling, modeled and observed molecular line emission of low and high density tracers.

The resulting maps of the dust spectral index and opacity at 1.1 mm are shown in Fig. 4.2. We find very similar results to those seen previously in Chacón-Tanarro et al. (2017): while the spectral index increases towards the center, the opacity decreases. The emission at the two bands peak at slightly different places, and this may cause the displacement of the spectral index peak from the 1.1 mm peak. The increase of the spectral index towards the center could be an indication of the presence of dust grains large enough to affect the emission at 1.1 mm, but not so much that it affects the emission at 3.3 mm. However, this would imply an increase in the opacity at 1.1 mm, and Fig. 4.2 shows a circular region around the center within which the opacity decreases. This is caused by the fact that the model is centrally concentrated. Moreover, as noted previously by Chacón-Tanarro et al. (2017), the emission of the core is clearly not following a sphere (see Fig. 4.1), and the model is spherical. Chacón-Tanarro et al. (2017) solved this problem by comparing the model with the emission of the core averaged in concentric ellipses. We therefore follow this same procedure in the following sections.

4.5.2 New spectral index and opacity

The emission of the core is averaged in concentric ellipses separated by 1.5″. The ratio of the major to minor axes of these ellipses is 1.5, and the major axis is inclined with respect to the declination by 65 degrees. The radial emission profiles are obtained by taking the

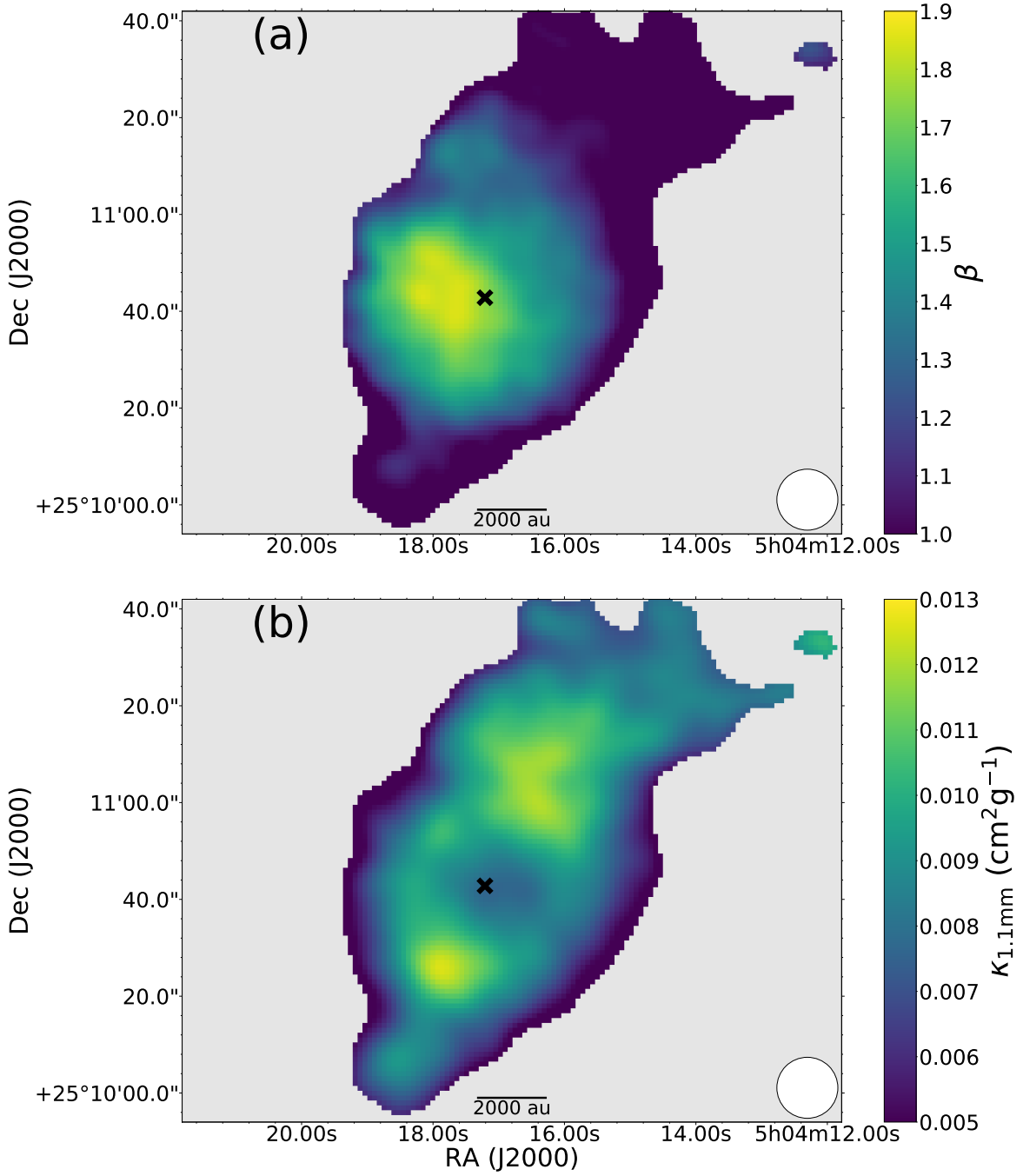

Figure 4.2: *Panel a)* shows the spectral index map, while *panel b)* shows the dust opacity map. Both maps have been derived as described in Section 4.5.1. The error in the spectral index is ∼0.2 and in the opacity is ∼10%.

geometric mean of the major and minor axes of the ellipses; the corresponding radius is labeled r_m.

We now include in our analysis the model for L1544 that Crapsi et al. (2007) presented, which is an improvement of the one presented by Tafalla et al. (2002). The temperature profile of this model was computed via excitation and radiative transfer modeling of their interferometric ammonia observations, while the density profile was constrained by fitting the emission seen in the 1.3 mm continuum map (Ward-Thompson et al. 1999). Therefore, while Keto et al. (2015) is purely theoretical, although constrained by observations, Crapsi et al. (2007) is based on observational results. Fig 4.3 shows the differences between the two models.

Modeling the core emission first requires a choice of spectral index and opacity. Following Chacón-Tanarro et al. (2017), we fit the spectral energy distribution (SED) of the core toward the center using the emission obtained with AzTEC, MUSTANG-2 and *Herschel*/SPIRE, after smoothing all the data to the resolution of the 500 μm band ($\sim$38.5″). This fit takes into account the temperature and density distributions in the core predicted by the physical models from Crapsi et al. (2007) and Keto et al. (2015). For a detailed description of this procedure, see Chacón-Tanarro et al. (2017).

The resulting spectral indexes and opacities from the SED fits are: $\beta = 1.6 \pm 0.4$ and $\kappa_{250\mu\mathrm{m}} = 0.03 \pm 0.01$ cm^{2}g^{-1} for the model of Crapsi et al. (2007); and $\beta = 2.0 \pm 0.4$ and $\kappa_{250\mu\mathrm{m}} = 0.16 \pm 0.07$ cm^{2}g^{-1} for the model of Keto et al. (2015). There is a difference of a factor of $\sim$5 between the opacities of the two models. This difference will be discussed at the end of this section. Comparing these values with the ones from Chacón-Tanarro et al. (2017), which are $\kappa_{250\mu\mathrm{m}} = 0.2 \pm 0.1$ cm^{2}g^{-1} and $\beta = 2.3 \pm 0.4$, we find that the spectral index is lower, although consistent within the errors. The slight difference is caused by the different filtering process applied during the data reduction process to the millimeter maps. In Chacón-Tanarro et al. (2017), the NIKA maps at 1.2 and 2 mm suffered from substantial filtering, which implied that, when smoothing the data to bigger beams, the emission was reduced due to the inclusion of negative flux values in the dust peak. Moreover, Chacón-Tanarro et al. (2017) expected to be recovering the emission from spatial scales smaller than 2′; while in these new maps we estimate to be recovering the emission from spatial scales up to 5′. This produces a higher spectral index.

With these new spectral indexes and opacities we proceed to check whether the models can reproduce the observations. We adopt a constant spectral index and opacity. Fig. 4.4 shows the ratio between the observations and the modeled emission. The first thing to notice is that the model of Keto et al. (2015) does not reproduce the data, showing discrepancies between the model and the observations of a factor of 2 for the 1.1 mm band and a factor of 2.5 in the 3.3 mm band within the inner 36″(region where the emission of the core is detected above 3σ). Changing the absolute values of the opacity and spectral index, for example, using the ones from Chacón-Tanarro et al. (2017), does not solve the situation (see Appendix C). The comparison between the model of Crapsi et al. (2007) and the observations shows that the 1.1 mm band is badly reproduced, with differences of a factor of 2 in the outer parts of the core; nonetheless, the model can reproduce the emission at 3.3 mm within 20%. These results therefore indicate that either the models

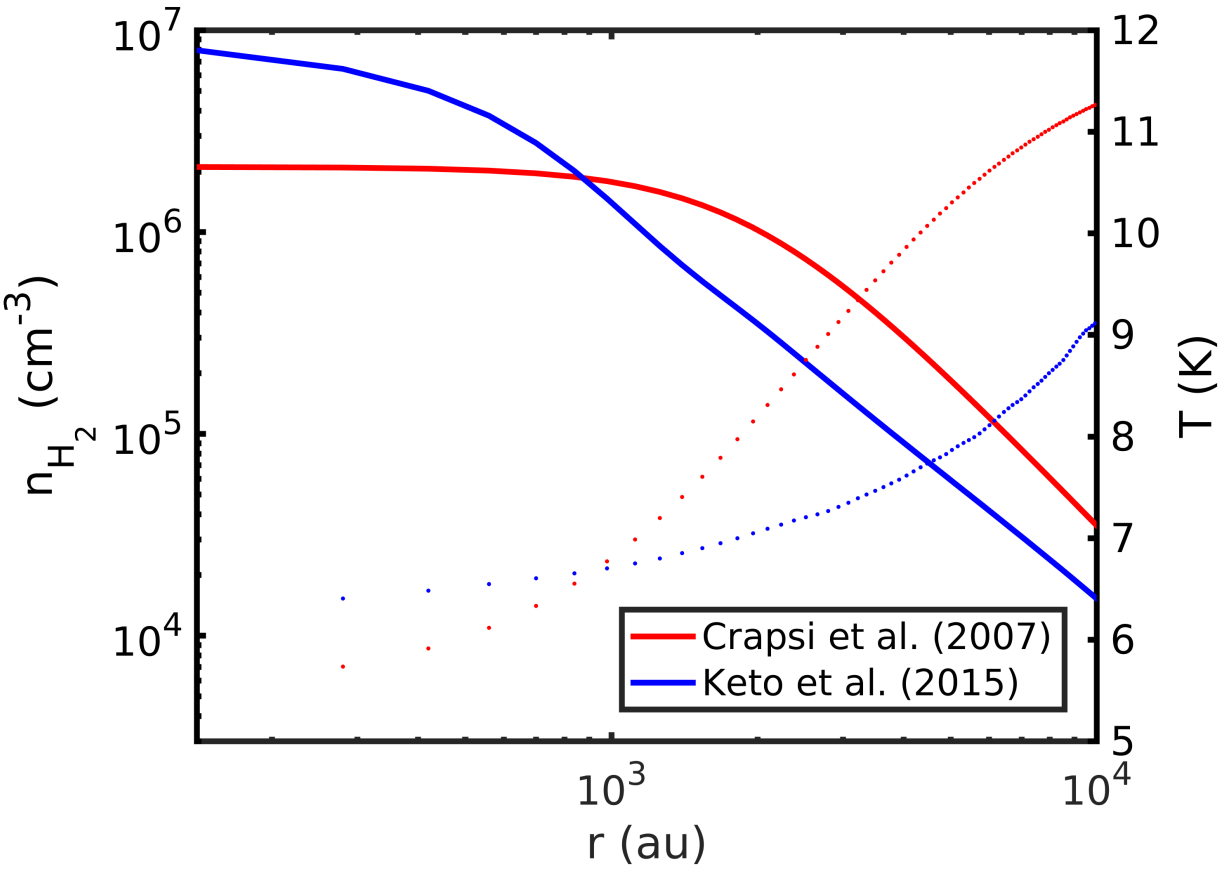

Figure 4.3: Density (solid line) and temperature (dotted line) profiles describing the physical properties of L1544 by Crapsi et al. (2007) in red and by Keto et al. (2015) in blue.

are wrong or that our assumption of constant spectral index and opacity across the cloud is not valid.

If the models are correct, then the required variations in the opacity, when considered constant along the line of sight, can be obtained from Eq. (4.1). This opacity can be considered the averaged opacity along the line of sight ($\overline{\kappa}_\nu$), as it is the opacity weighted by the temperature and density. Then, $\overline{\kappa}_\nu$ can be derived following the ratio for both wavelengths:

$$\overline{\kappa}_\nu = \frac{I_\nu}{\mu_{\mathrm{H_2}} m_{\mathrm{H}} \int_{s_{\mathrm{los}}} B_\nu[T_{\mathrm{d}}(s)] n_{\mathrm{H_2}}(s) ds}. \tag{4.3}$$

Fig. 4.5 shows the variations of the opacities. The gradients in $\overline{\kappa}_\nu$ imply variations in the spectral index, averaged along the line of sight (see Fig. 4.6). Figs. 4.5 and 4.6 show that there are substantial changes in the opacity and the spectral index averaged along the line of sight.

To obtain radial variations of κ_ν and β, we follow the method described in Roy et al. (2014). Using the Abel transform (see e.g. Bracewell 1986) we can write Eq. (4.1) in the

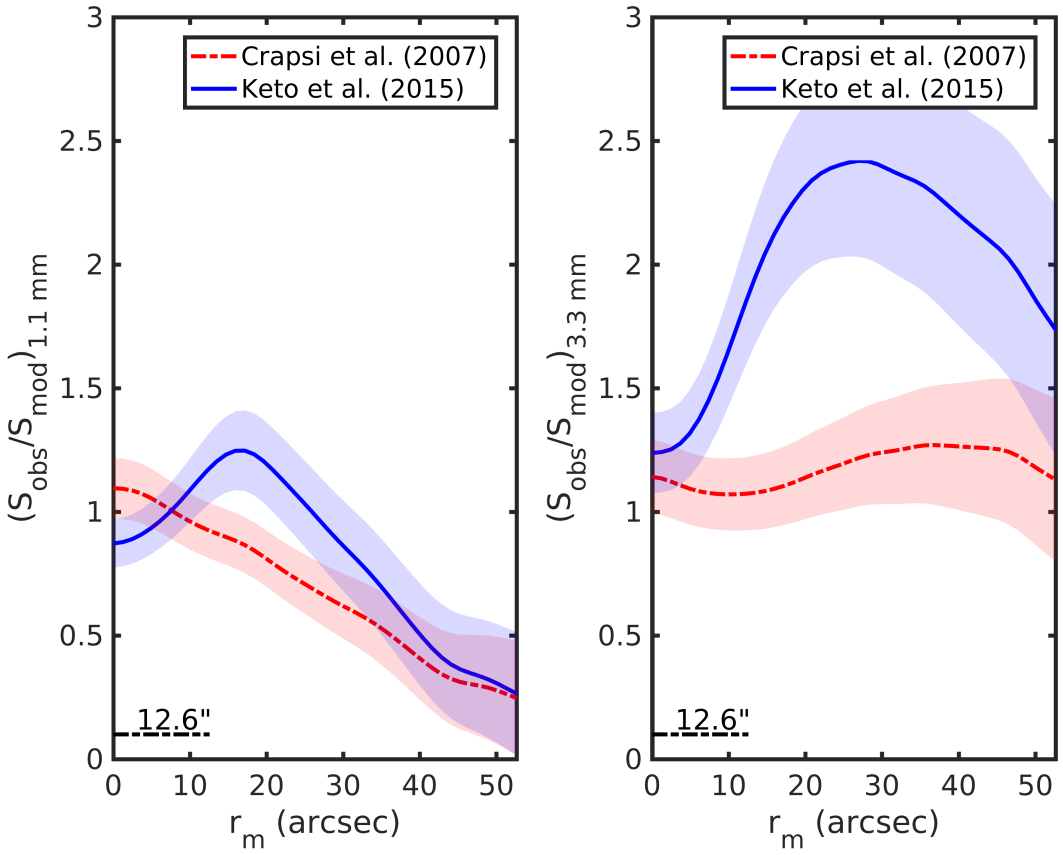

Figure 4.4: Ratio between the observed emission and the modeled emission derived as described in Section 4.5.2, as a function of projected radius r_m. The shaded regions show the error associated with the data. The resolution of the maps is indicated with a bar of length 12.6″in the bottom left corner of both panels.

following way:

$$\mu_{\mathrm{H_2}} m_{\mathrm{H}} B_\nu[T_d(r)] n_{\mathrm{H_2}}(r) \kappa_\nu(r) = -\pi^{-1} \int_r^\infty \frac{\mathrm{d}I_\nu}{\mathrm{d}b} \frac{\mathrm{d}b}{\sqrt{b^2 - r^2}}, \tag{4.4}$$

where b is the projected distance to the center. This way, we are able to obtain opacity radial profiles once the temperature and the density are well defined.

The procedure is very sensitive to noise, so we fit the emission profiles with an analytic function. In this manner, abrupt changes in the derivatives of the emission profiles are avoided. We used a combination of 3 Gaussian functions, which provides continuous derivatives and good fits to the emission profiles. We note that this process gives radial profiles smoothed to the resolution of the data (Roy et al. 2014), so the temperature and density profiles are smoothed to the resolution of 12.6″for consistency. To evaluate the error associated with this process, we first create 1000 maps for each wavelength, which are the result of adding in each map random noise from a Gaussian distribution of σ equal to the rms of the data. Then, we derive the opacity variations for all the maps and assume the standard deviation of all the samples as the error.

Figs. 4.7 and 4.8 show the resulting radial distributions of the opacities and the spectral index, respectively. The 1.1 mm opacities are in the range of values predicted by Ossenkopf & Henning (1994) for different grain size distributions and conditions. The radial opacity profile for the model of Keto et al. (2015), which is consistent with dense clouds and thick ice mantels, follows a shape that indicates that the model produces too much emission in the center. On the other hand, the opacities at 1.1 mm for the model of Crapsi et al. (2007) are consistent with bare grains and no coagulation, although one has to take into account that a factor of 2 is within the uncertainties (Ossenkopf & Henning 1994). The shape of the opacity at 3.3 mm is due to the presence of the emission towards the north-east, which is better seen in MUSTANG-2. This emission can only be recovered by increasing the opacity at ∼7000 au, as the density profile does not take it into account. Thus, this increase of opacity is due to an excess of material which is not being considered in the model. Deeper 1.1 mm observations should show this feature as well. The spectral indexes show very similar behavior, which indicates that they mainly depend on the relative variation of the emission seen between both wavelengths.

To examine the validity of the derived opacities, we generate synthetic maps and compare their emission profiles with the observed ones. The models reproduce the observations fairly well (see Fig. 4.9). In this process, the resolution of the models and the opacities were considered to be the same. Although the resolution of our observations does not allow us to resolve the inner 1 000 au, where the difference between the two models is higher, the emission produced by them at a resolution of 12.6″ is very different (as seen in Fig. 4.4), with the Crapsi et al. (2007) profile matching the data better than the Keto et al. (2015) model. The Crapsi et al. (2007) model was derived from observations so it also has a limited resolution of 7″, which is close to the resolution of the maps presented. Nevertheless, a discrepancy of 10-20% is reasonable due to beam effects (Roy et al. 2014).

We emphasize here that the opacity and spectral index variations found in this analysis depend on the particular density and temperature profiles assumed, and that inaccurate

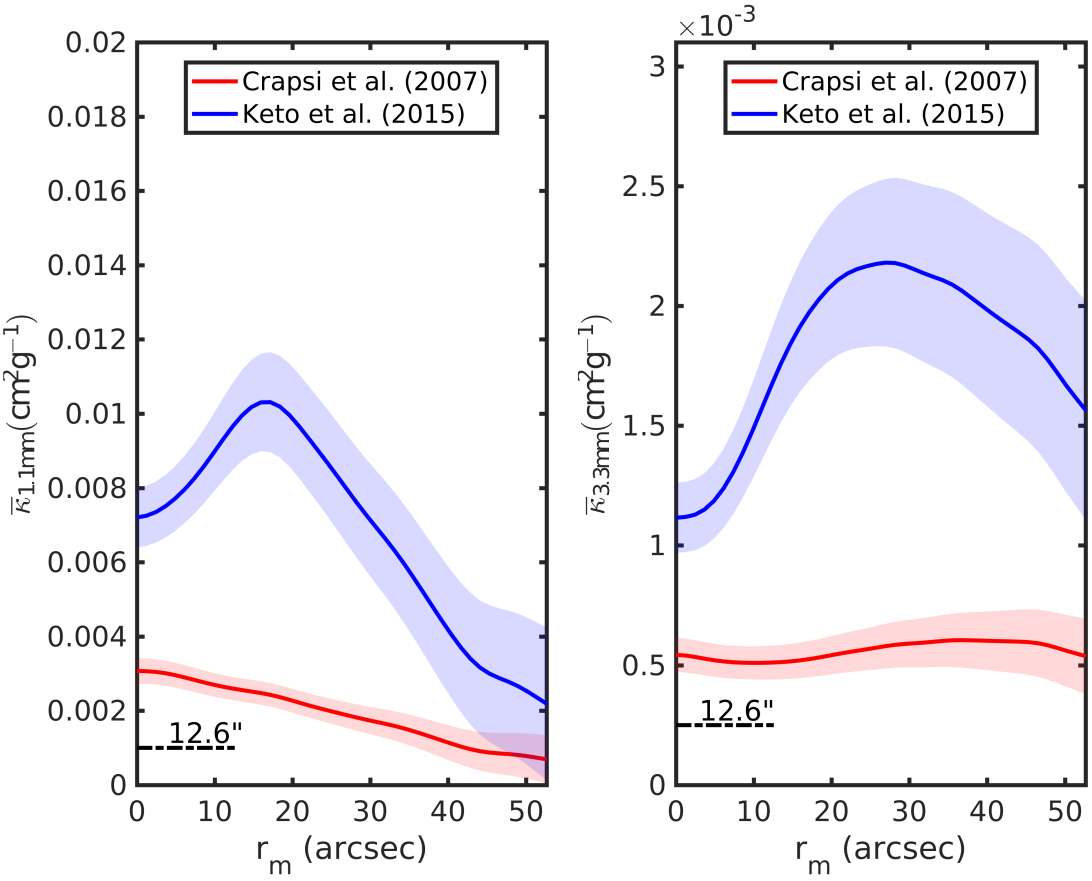

Figure 4.5: Opacities at 1.1 mm (*left*) and at 3.3 mm (*right*), averaged along the line of sight, as a function of the projected radius r_m. The blue curve is obtained when using the core physical structure derived by Keto et al. (2015); the red curve is obtained when using the physical structure from Crapsi et al. (2007). The shaded regions show the error associated with the data. The resolution of the maps is indicated with a bar of length 12.6″in the bottom left corner of both panels.

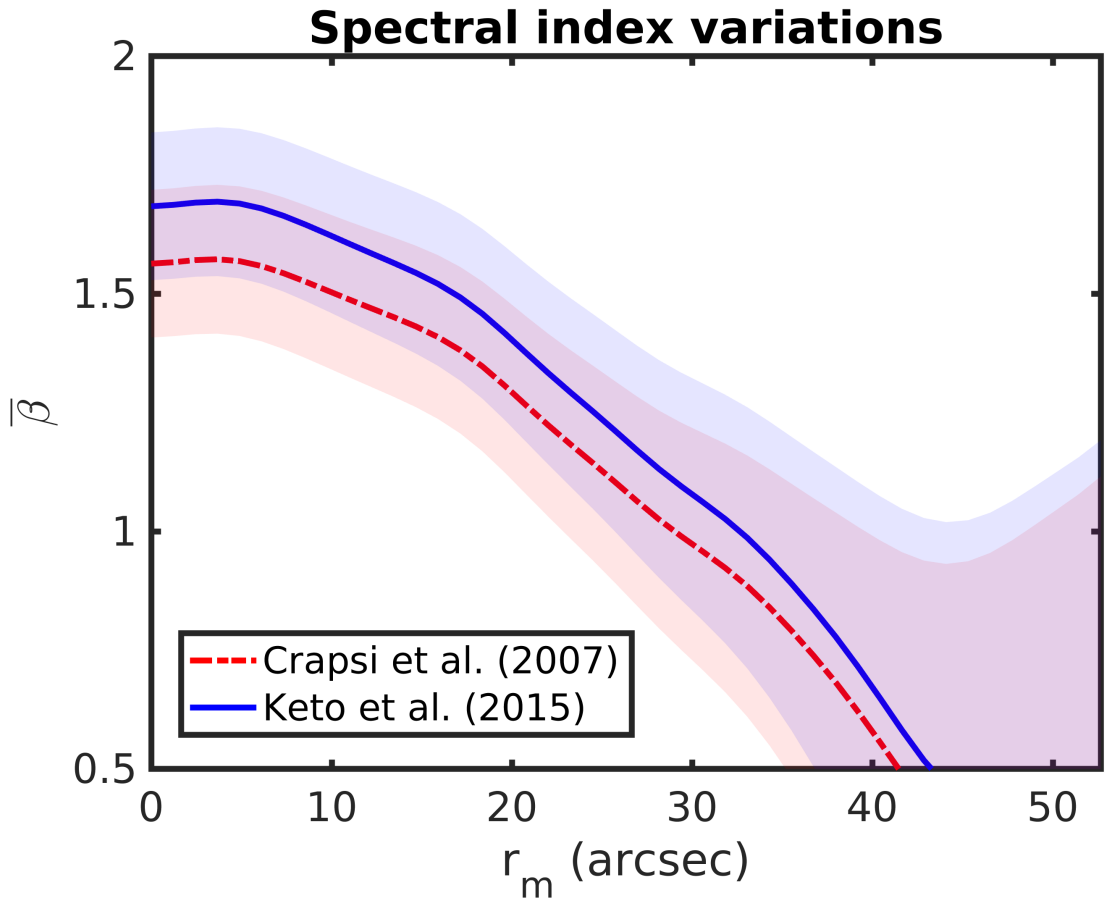

Figure 4.6: Spectral index variation, averaged along the line of sight, as a function of the projected radius r_m, caused by the variation on $\overline{\kappa}_\nu$ shown in Fig. 4.5. The different colors refer to the different physical structure adopted (blue for Keto et al. 2015 and red for Crapsi et al. 2007). The shaded regions show the error associated with the data.

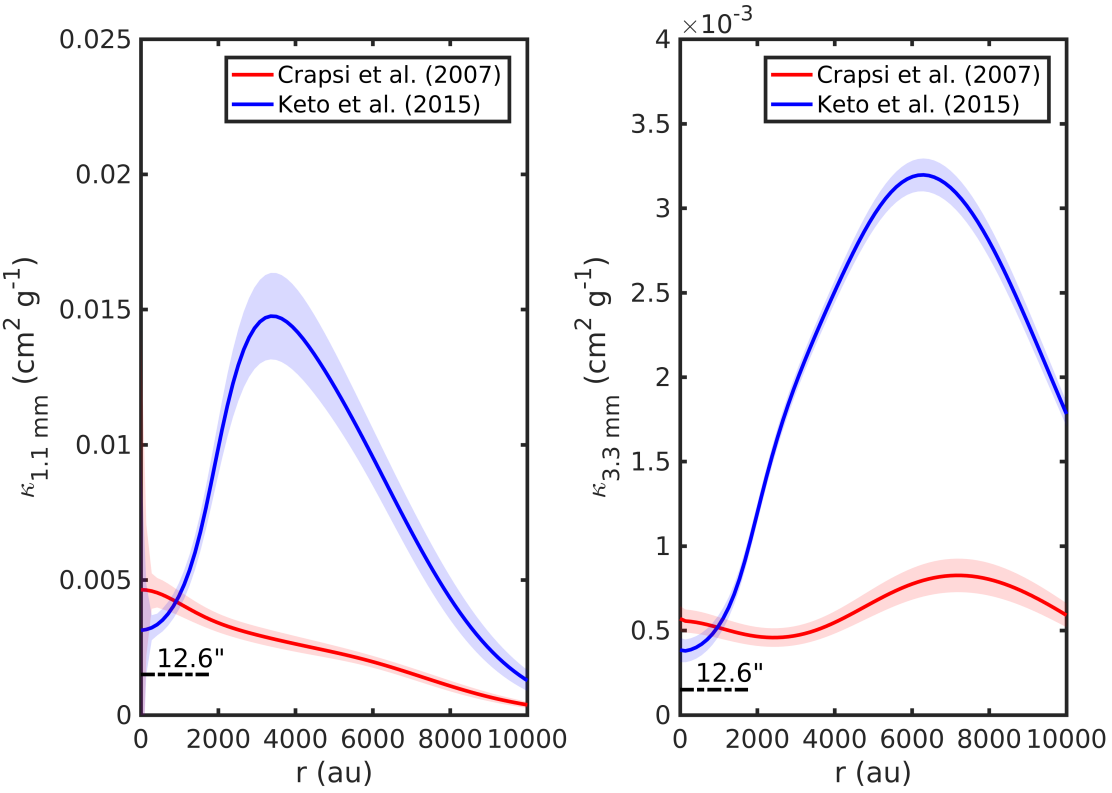

Figure 4.7: Opacity radial variations obtained as explained in Section 4.5.2. This figure shows $\kappa_\nu(r)$, while Fig. 4.5 shows $\kappa_\nu(r)$ averaged along the line of sight, i.e., $\overline{\kappa}_\nu(r_m)$. The different colors refer to the different physical structures adopted (blue for Keto et al. 2015 and red for Crapsi et al. 2007). The shaded regions show the error associated with the process.

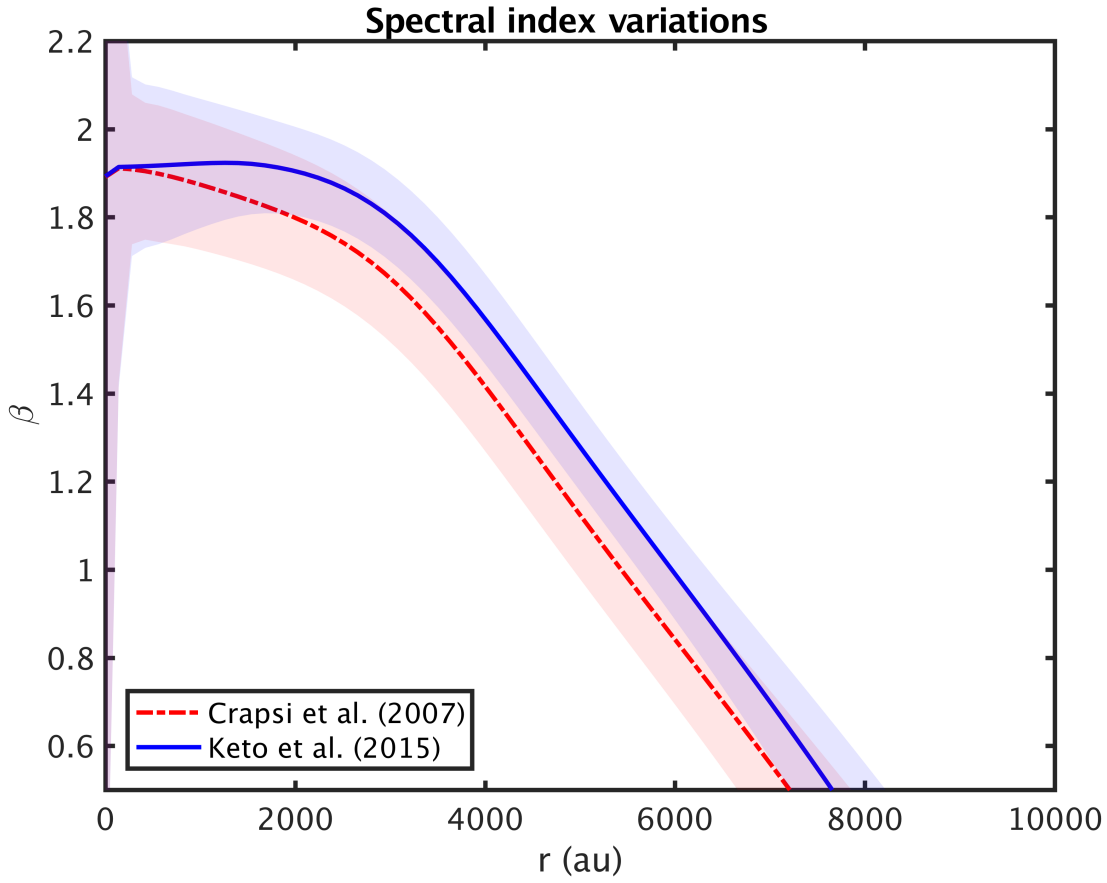

Figure 4.8: Spectral index radial variations obtained as explained in Section 4.5.2. This figure shows $\beta(r)$, while Fig. 4.6 shows $\beta(r)$ averaged along the line of sight, i.e., $\overline{\beta}(r_m)$. The different colors refer to the different physical structure adopted (blue for Keto et al. 2015 and red for Crapsi et al. 2007). The shaded regions show the error associated with the process.

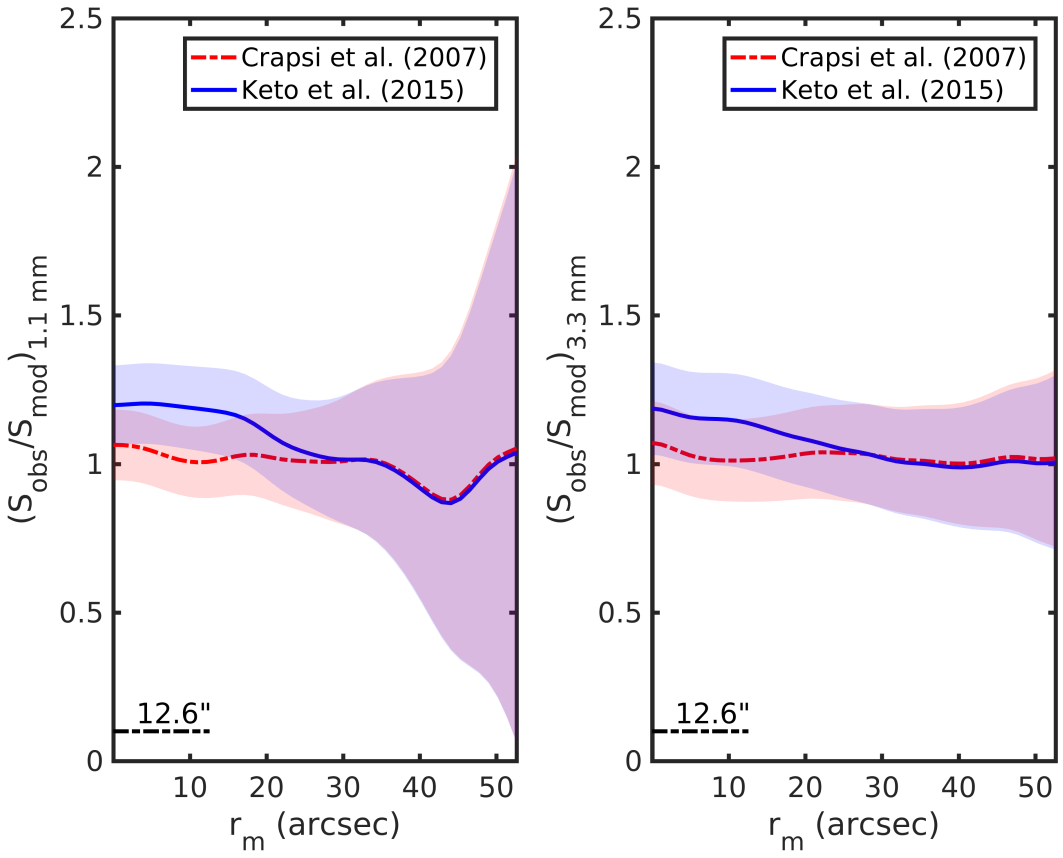

Figure 4.9: Ratio between the observed emission profiles and the modeled emission profiles taking into account the radial opacity variations shown in Fig. 4.7. The shaded regions show the noise associated with the data.

profiles will provide inaccurate and artificial variations in κ_ν and β. For example, as already said, Keto et al. (2015) artificially increased the dust opacity by a factor of 4 to reproduce the temperature drop measured by Crapsi et al. (2007), as their model is dynamic and the gravitational compression toward the center produced extra heating; this dust opacity enhancement was applied throughout the core, affecting the overall structure. It is therefore natural that their physical model results, on average, in higher opacities than the model of Crapsi et al. (2007). This shows that the initial assumption made for the opacity biases our results. In addition, opacity variations would indicate that any previous derivation of the temperature and density of the cloud which did not take this into account might also need modifications. In what follows, we use the model from Crapsi et al. (2007), which does not consider dynamics and only aims at reproducing the observed temperature structure, as the starting point in our efforts to determine the radial distributions of the density, temperature, and the dust opacity in L1544.

4.6 New physical structure

4.6.1 Method

To obtain density, temperature and opacity profiles consistently, we apply an iterative method. Starting from the radial opacity variations shown in Fig. 4.7 and the density distribution derived by Crapsi et al. (2007), the following steps are taken:

1. First, the optical depth is derived by taking the radial profile of the opacity and the density[1]. From the optical depth we follow the equations given by Zucconi et al. (2001) to derive $A_V(r)$ and $T(r)$. These authors derived analytical equations that can be used to obtain the temperature profile for clouds externally illuminated by the standard interstellar radiation field (which includes an optical and near infra-red component coming from the emission of disk dwarf and giant stars, a far infra-red component from dust grains, a mid-infrared component from non-thermally heated grains and a millimeter component from the cosmic background radiation, following the work of Black 1994 and Mathis et al. 1983).

2. With this new temperature profile and the opacity variations we derived a new density profile using the Abel transform (see Eq. (4.4)).

3. A new opacity profile is obtained from the new temperature and density profiles, again using the Abel transform.

From point 3, we return to point 1 until $\kappa_{1\mathrm{mm}}$ varies less than 0.001%. In points 1 and 2 we need to take one band as reference, which we choose to be the one at 1.1 mm. However, these results are independent of the chosen band. In point 1 an extra factor in

[1]The optical depth at 1.1 mm, τ_{1mm}, always satisfies $\tau_{1mm} \ll 1$, justifying the assumption of optical thinness throughout this study.

A_V is included that comes from the fact that the cloud is surrounded by an external layer of low density material that increments the value of A_V by 2 magnitudes (see Appendix C). Unfortunately, Zucconi et al. (2001) do not provide a value for the temperature at extinctions lower than 10 magnitudes. Thus, we assume that the temperature follows a similar parametrization than that used by Crapsi et al. (2007) and use their external temperature as a constraint in our temperature profile. Thus, the temperature follows this formula:

$$T(r) = T_{out} - \frac{T_{out} - T_{in}}{1 + \left(\frac{r}{r_{t0}}\right)^{\alpha_t}}, \tag{4.5}$$

where T_{out}=12 K, the temperature of the outer part of the core as measured by Crapsi et al. (2007). We thus fix this value and fit the rest of the parameters to our data in each iteration.

Beam effects are not considered here. However, as already mentioned, the resulting profiles from this process will be smoothed with the beam of our observations.

Only a few iterations are needed to find a convergence. The density profile is parametrized in the following way:

$$n_{\mathrm{H_2}}(r) = \frac{n_0}{1 + \left(\frac{r}{r_0}\right)^{\alpha}}. \tag{4.6}$$

The obtained temperature and density profiles are:

$$T(r) = 12(\mathrm{K}) - \frac{6.9(\mathrm{K})}{1 + \left(\frac{r('')}{28.07''}\right)^{1.7}} \tag{4.7}$$

and

$$n_{\mathrm{H_2}}(r) = \frac{1.6 \times 10^6(\mathrm{cm^{-3}})}{1 + \left(\frac{r('')}{17.3''}\right)^{2.6}} \tag{4.8}$$

We note that this method is biased by the initial parameters used. A lower initial density leads to higher opacities, and vice versa. This issue is discussed in Appendix C.3. The emission at only two wavelengths is fitted with three parameters, density, temperature and dust opacity, and therefore, the solution is not unique. Thus, further modeling efforts utilizing all the available continuum data are needed.

Fig. 4.10 shows these new profiles, together with the profiles obtained by Crapsi et al. (2007) and the temperature profile obtained by Crapsi et al. (2007) using the method from Zucconi et al. (2001) for comparison. On the one hand, there is a difference between the temperature derived by Crapsi et al. (2007) and the new temperature. This is because they obtained the temperature profile from gas temperature measurements, while here it is purely dust temperature. If our temperature profile is compared to their dust temperature profile, which was derived in a similar way to ours, there is better agreement. The difference is less than 1 K, and it is due to the lower values in the opacities used here (compared to

those commonly used), which result in lower values of A_V towards the central regions (with a maximum of 52 magnitudes). The fact that the iteration did not lead us very far from the physical model of Crapsi et al. (2007) makes the solution plausible.

Fig. 4.11 shows the obtained radial distributions of the opacity and spectral index. The first thing to note is that the opacities go to 0 at large radii because of the method used. The Abel transform forces the left hand part of Eq. (4.4) to be zero when the derivative of the emission with respect to the impact parameter is 0. This is satisfied as soon as the emission is below 1σ. As $n_{\mathrm{H_2}}$ and $B[T_{\mathrm{d}}(r)]$ cannot be 0 due to their parametrization, the only parameter which can go to 0 is the opacity. Nevertheless, this is artificial, and we know that the cloud still emits at larger scales thanks to *Herschel* observations. However, although the filtering does not seem to be a problem in these maps, the extended emission is very difficult to recover with ground based telescopes (we estimate to be recovering the emission of scales up to $\sim 5'$), and this effect should be taken into account (by, for example, applying the same data reduction process to the synthesized maps). In any case, the variations derived for $r < 5\,000$ au, where the emission is above the 3σ level, are significant.

We derive the opacity at 3.3 mm also at its intrinsic resolution. This can be done because when we derive the opacity both wavelengths are treated independently, and the resolution of the map at 3.3 mm is only 23% lower than that of the map at 1.1 mm, otherwise the density and temperature should change. Fig. C.6 shows the resulting opacity.

Fig. 4.12 shows that the new density, temperature and opacity profiles can reproduce the observations. Although, as already discussed, these profiles are at the resolution of $12.6''$, the model was considered at infinite (or intrinsic) resolution. We also check the results at the MUSTANG-2 resolution and find good agreement between the model and the observations (see Fig. C.7).

4.6.2 New density and temperature profiles: comparison with previous profiles

Fig. 4.10 shows that the new density profile is flatter in the inner regions of the cloud when compared to that deduced by Crapsi et al. (2007). It also has a lower central density than the models from Crapsi et al. (2007) (by 25%) and Keto et al. (2015) (by a factor of $\sim$5, see Fig. 4.13). Nevertheless, this profile, as well as the one from Crapsi et al. (2007), gives a mass in the central $\sim$10 000 au of 4 $\mathrm{M}_\odot$, while the model from Keto et al. (2015), with a steep density gradient, gives a mass of 1.4 $\mathrm{M}_\odot$.

The obtained dust temperature in the cloud center is approximately 1 K higher than that derived by Crapsi et al. (2007) using the same method. The agreement with the model of Keto et al. (2015) is fairly good.

4.6.3 Implication of opacity variations

Any variation of the opacity can arise from, for example, changes in the ice composition, grain coagulation or changes in the shape of the grains. In view of the fact that CO

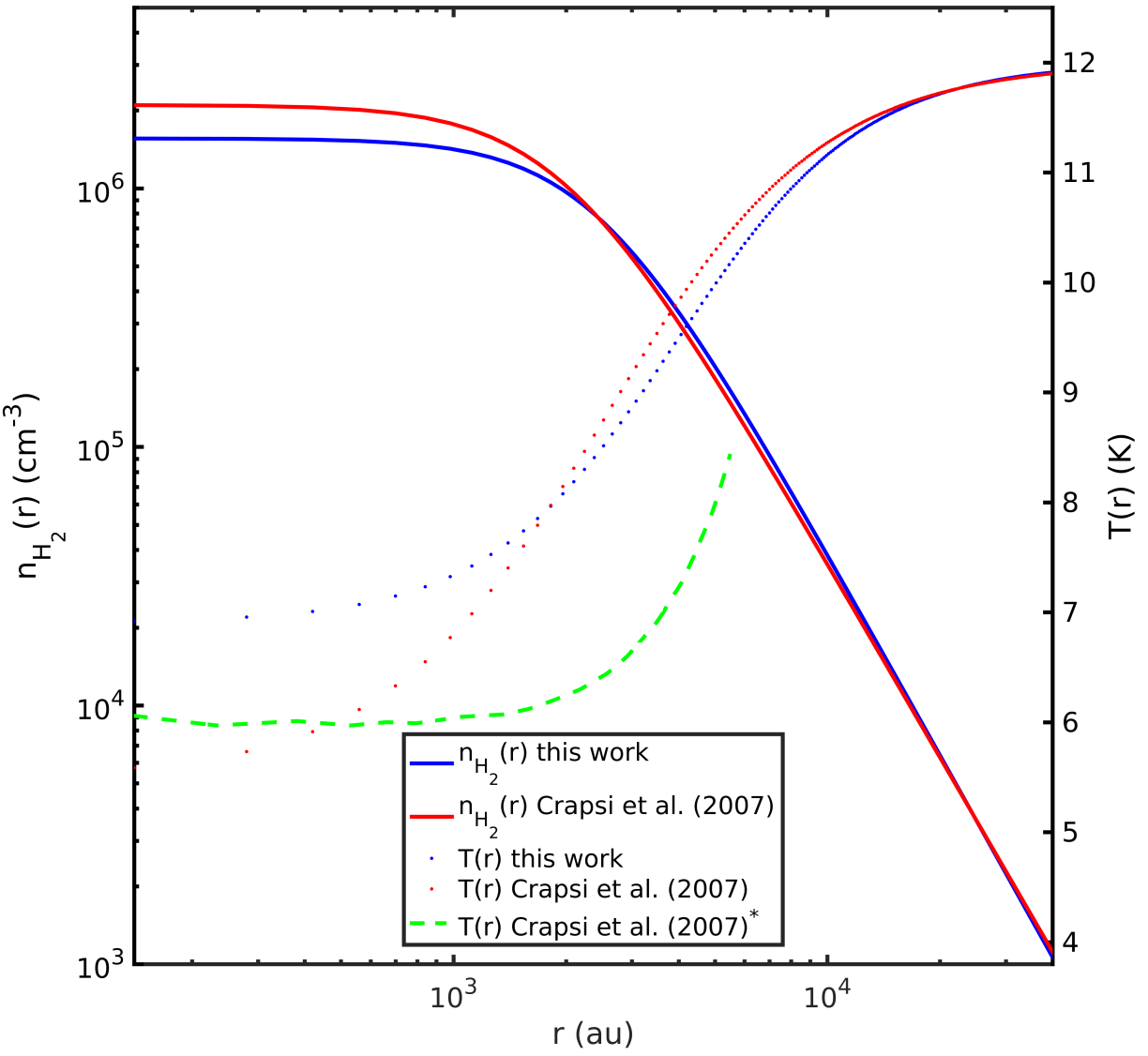

Figure 4.10: New density (blue solid line) and temperature (blue dotted line) profiles derived as described in Section 4.6.1. In red, density (solid line) and temperature (dotted line) profiles from Crapsi et al. (2007). In green, temperature profile from Crapsi et al. (2007) derived using the formulae from Zucconi et al. (2001), here Crapsi et al. (2007)*.

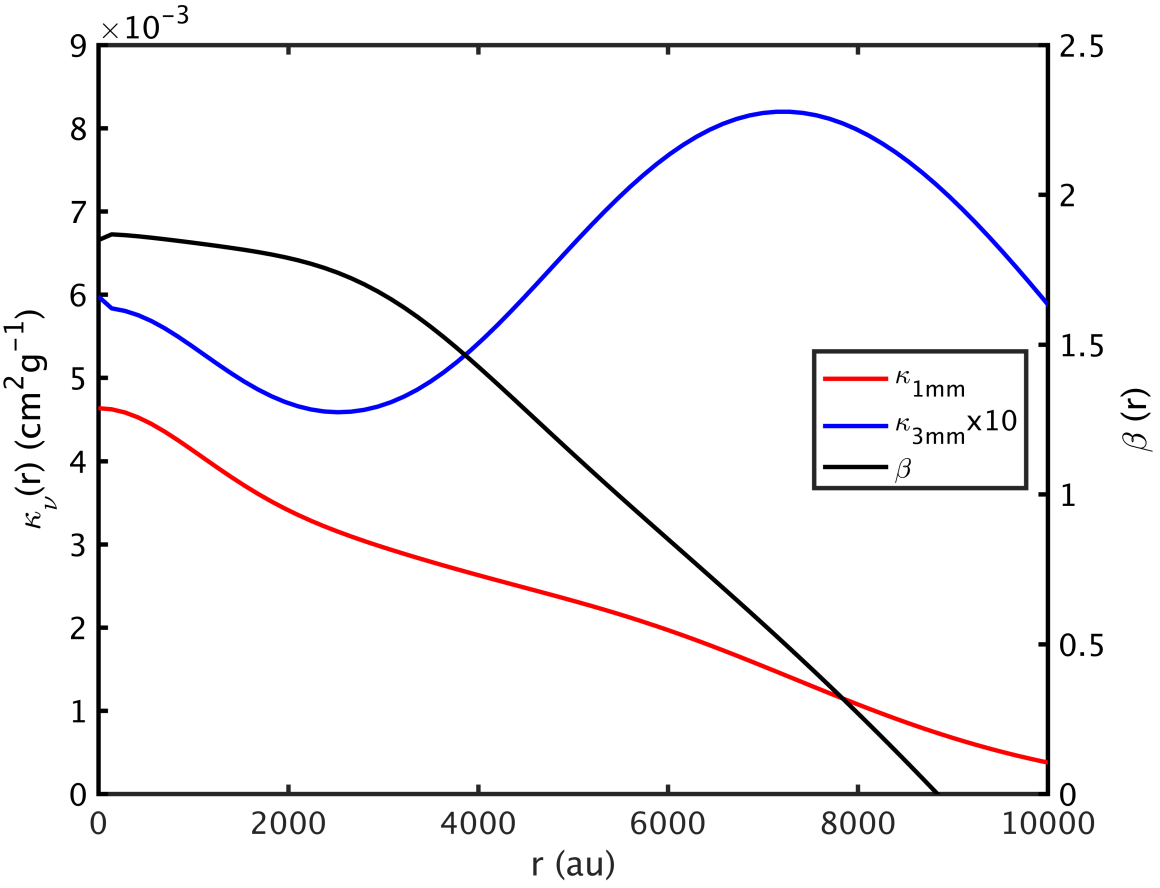

Figure 4.11: Radial opacity and spectral index variations derived as described in Section 4.6.1.

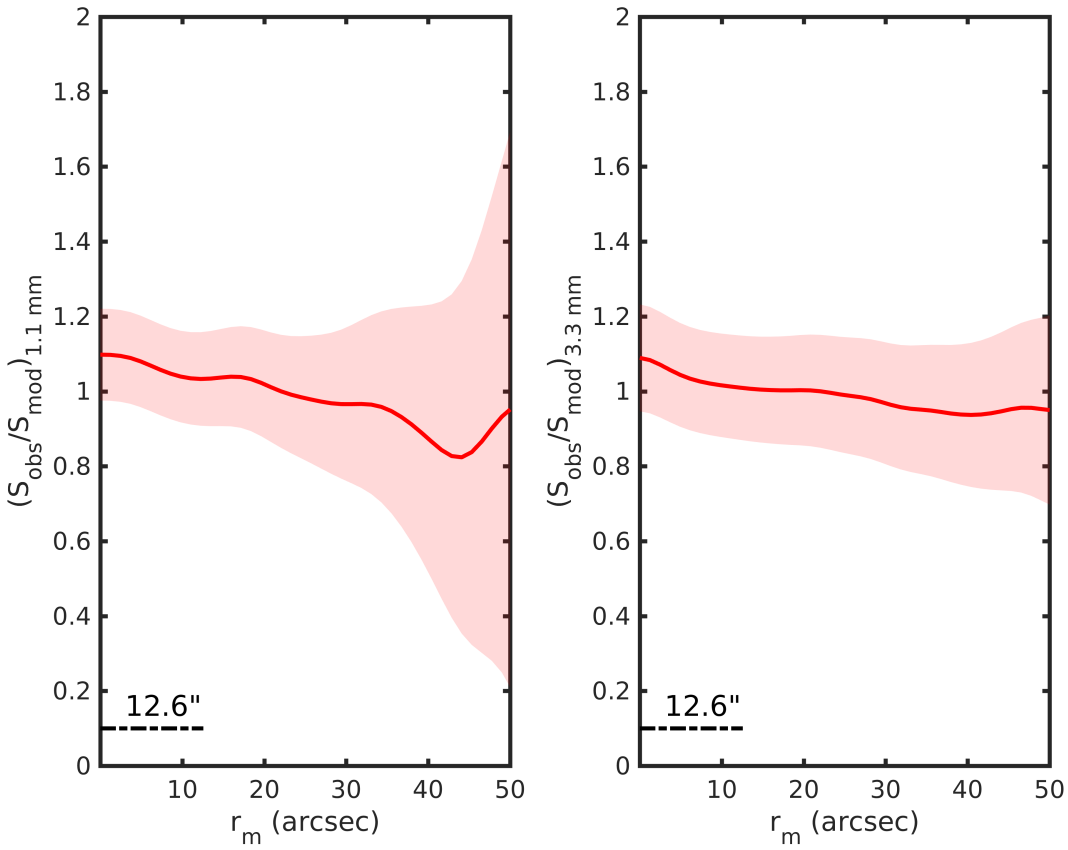

Figure 4.12: Ratio between the observed emission profiles and the modeled emission profiles taking into account the radial opacity variations and new density and temperature profiles, as explained in Section 4.6.1. The shaded regions show the noise associated with the data.

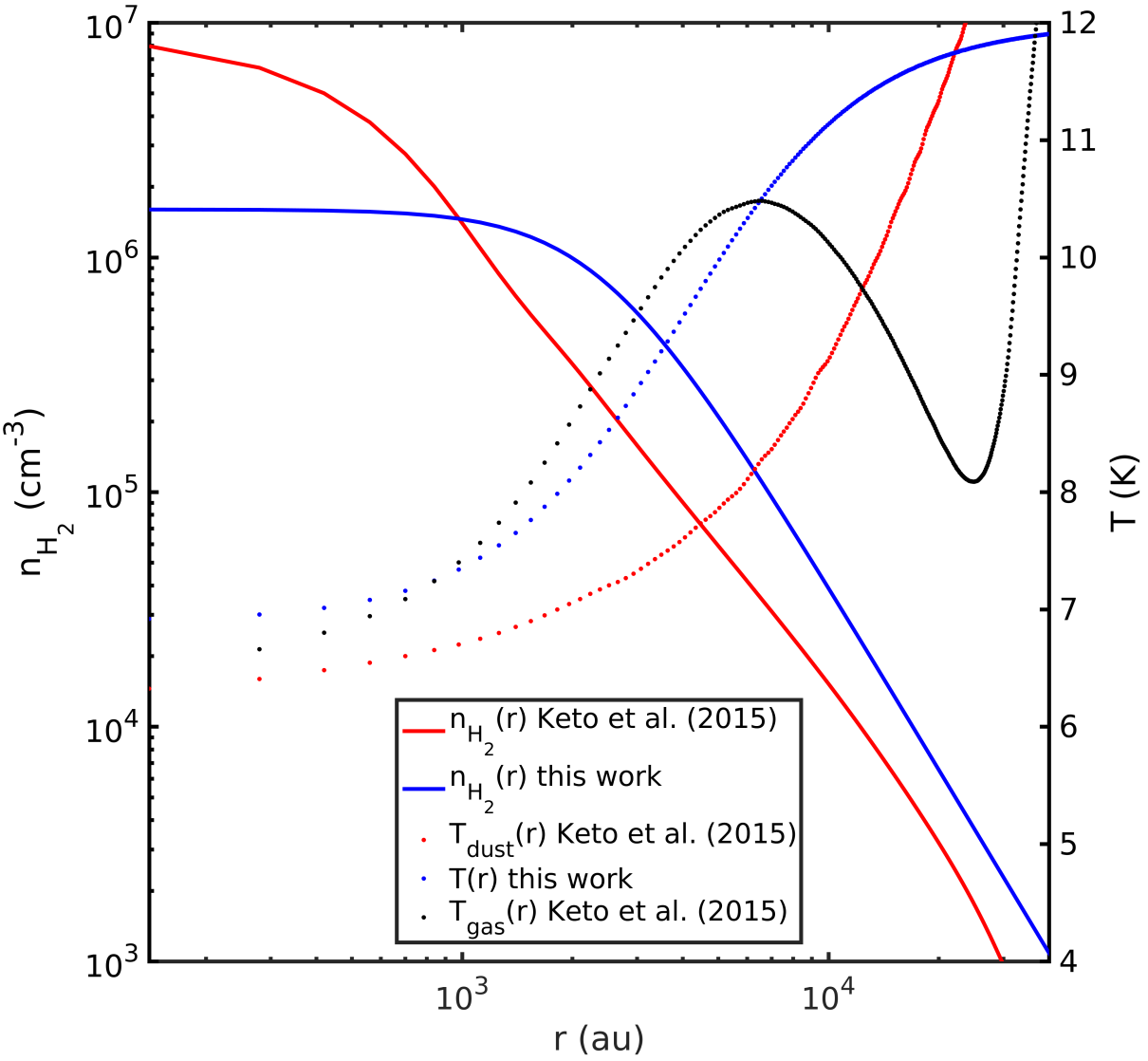

Figure 4.13: New density (blue solid line) and temperature (blue dotted line) profiles derived as described in Section 4.6.1. In red, density (solid line) and dust temperature (dotted line) profiles from Keto et al. (2015). In black, gas temperature profile from Keto et al. (2015).

molecules are known to be frozen onto dust grains in the central parts of dense cores (Caselli et al. 1999), the dust grains are expected both to increase in size and to change in composition, following the growth of icy mantles.

The study from Ossenkopf & Henning (1994) already predicted changes between the diffuse Interstellar Medium (ISM) and the densest parts of the core, including the effect of ice mantle growth. For example, at 1 mm, the change in opacity from the initial conditions, with no coagulation, to the dense regions with thick ice mantles is a factor of ∼3. Here, we find that from regions of density $\sim 10^5\,\mathrm{cm}^{-3}$ to the central dense regions ($n_{\mathrm{H_2}} > 10^6\,\mathrm{cm}^{-3}$), the opacity changes by a factor of ∼4. The opacity variations are consistent with the results from Ossenkopf & Henning (1994) when ice mantle growth and coagulation are taken into account, but the values found here are systematically lower by a factor of 2. However, this difference is within the uncertainties (Ossenkopf & Henning 1994), in addition to the effects of the beam, which dilutes the centrally concentrated structure and its emission, thus mimicking an opacity decrease. For example, if one compares the opacity at 3.3 mm at the resolution of 12.6″ (Fig. 4.11) with the opacity obtained at 9.7″ resolution (Fig. C.6), there are differences up to 20%, so bigger differences are expected between the actual structure and the one we observe. Nevertheless, the values of these opacities depend strongly on the initial density profile assumed, and they may vary as well if the external low density cloud and the filtering are considered. In fact, this also explains the fact that the opacity at the center of the core is very close to $\kappa_{1.2\mathrm{mm}} = 0.005\,\mathrm{cm}^2\mathrm{g}^{-1}$, which is the value used by Crapsi et al. (2007) to derive the density profile through the 1.3 mm continuum observations of Ward-Thompson et al. (1999).

The variation at 3.3 mm, as already noted above, may be due to the extended emission toward the north-east part of the core. Although the emission from this region is below 3σ, when doing the averaging in ellipses, an opacity increase is needed to obtain the observed emission. However, as this is faint emission, if one considers a constant opacity at 3.3 mm with a value of $\sim 5\times10^{-4}\,\mathrm{cm}^2\mathrm{g}^{-1}$ the emission is well modeled within ∼20% accuracy. Therefore, the variations at 3.3 mm may not be real or attributed to dust grains, but show that this extended emission should be considered when modeling the density with more sensitive observations.

Comparing the observations with a simple grain growth model applied to L1544 as done by Chacón-Tanarro et al. (2017), updating the density profile, we find that grain coagulation produces grains of ∼3-4 μm size within the central 2 000 au (see Appendix C). The method used to obtain the corresponding opacities does not give any detectable opacity variations. On the other hand, this method does not take into account the ice mantles. Therefore, we are not able to test quantitatively this prediction via comparison with our data. Updated dust opacities and higher angular resolution observations, e.g. with ALMA, are needed.

4.7 Conclusions

We have used two new millimeter facilities, AzTEC at the LMT and MUSTANG-2 at the GBO, to study the physical structure and dust emission properties of the pre-stellar core L1544. Their sensitivity and resolution have allowed us to study the inner ∼1700 au of the core with a beam of 12.6″. The results show that previous density profiles deduced by Keto et al. (2015) and Crapsi et al. (2007) are not able to explain the emission of the core at 1.1 and 3.3 mm without invoking dust opacity variations, which in turn implies a need to re-determine the physical structure of the core, as these models did not consider opacity variations.

Although future work including the emission at different wavelengths is needed, we modified self-consistently the model from Crapsi et al. (2007) making use of the Abel transform and the analytical formulae from Zucconi et al. (2001). We thus obtained a new density and temperature profile, together with the radial opacity variations seen towards the core. These opacity gradients show increasing opacities toward the core center, where thick icy mantles are expected. However, the measured opacities are about a factor of 2 lower than those of coagulated dust grains (Ossenkopf & Henning 1994). Our model predicts dust grains of 3-4 μm in size within the central 2 000 au of L1544, which indicates that dust coagulation may not be affecting the emission at millimeter wavelengths yet.

This study needs to be expanded to a sample of cores, in order to test the general validity of these conclusions. Furthermore, interferometric observations are needed to study the yet unresolved center of the core. These will allow a quantitative comparison between observations and grain growth models, which predict relatively large (3-4 μm) dust grains in the central 2 000 au of L1544.

Chapter 5

Conclusions and future prospects

5.1 Summary

This thesis has been focused on the pre-stellar core L1544, which is a nearby pre-stellar core presenting clear signs of evolution (Crapsi et al. 2005). Very dense pre-stellar cores have very short lifetimes (Könyves et al. 2015), which means that an object like L1544 is very difficult to find. Being very dense (Keto & Caselli 2010) and showing very high deuteration (Caselli et al. 2002b), it is therefore the perfect source to search for signatures of grain coagulation, and to study the emission of complex deuterated molecules. This helps us to understand the very initial conditions in the process of star formation, which are of importance for the future evolution of a Solar-like system.

5.1.1 Dust emission

Dust continuum emission at millimeter wavelengths is highly affected by the presence of large dust grains. This emission depends on two optical properties of dust grains, the opacity and the spectral index. Any variation of these from the low external layers of the core to the denser parts can be an indication of dust coagulation.

The study of the emission of the dust in this thesis has shown the following:

- The second Chapter is focused on the study of the continuum emission seen with NIKA at the 30 m IRAM telescope, at 1.2 and 2 mm. These new maps, in combination with those from *Herschel*/SPIRE at 250, 350 and 500 μm, showed us that L1544 is well represented by an opacity of $\kappa_{250\mu\mathrm{m}} = 0.2 \pm 0.1$ cm^{2}g^{-1} and $\beta = 2.3 \pm 0.4$. From these values, the emission from L1544 was modeled using the physical structure found by Keto et al. (2015), who modeled L1544 following the evolution of an unstable Bonnor-Ebert sphere. The modeled emission perfectly matched the observed emission, with no need to invoke opacity changes from the outskirts to the center of the core. These results therefore suggested that no grain coagulation is taking place in this pre-stellar core. However, a simple grain growth model shows that a structure like the one from Keto et al. (2015) would allow dust grains to grow up

to ∼230 μm. Dust grains of ∼230 μm would imply dust opacity changes of a factor of 2.5 at ALMA's resolution, and only 15% at NIKA's resolution. Unfortunately, while the resolution and sensitivity of the new observations of NIKA were not able to detect these opacity variations, our results suggest that it should be detectable with interferometric observations.

- The fourth Chapter of this thesis was focused on the emission seen at 1.1 and 3.3 mm. These maps were obtained with the cameras AzTEC at the LMT and MUSTANG-2.0 at the GBO, respectively. For the first time, millimeter ground-base telescopes showed a hint of detection of a larger scale structure, which could only be seen previously in the CO emission and *Herschel*/SPIRE maps. This study follows the same steps as in Chapter 2, with the exception of considering two physical descriptions of the cloud, the one from Keto et al. (2015) and the one from Crapsi et al. (2007), who obtained a physical model of the core through ammonia and dust continuum emission. These two new maps, together with *Herschel*/SPIRE, gave a representative spectral index and opacity of $\beta = 1.6 \pm 0.4$ and $\kappa_{250\mu m} = 0.03 \pm 0.01$ cm^{2}g^{-1} for Crapsi et al. (2007); and $\beta = 2.0 \pm 0.4$ and $\kappa_{250\mu m} = 0.16 \pm 0.07$ cm^{2}g^{-1} for Keto et al. (2015). However, contrary to what was seen in the case of the NIKA maps, these new maps could not be reproduced maintaining the opacity and spectral index constant. A method that uses the Abel transform allowed us to obtain radial opacity variations at 1.1 and 3.3 mm, with their respective spectral index variations, and to modify consistently the density and temperature profiles obtained by Crapsi et al. (2007). These results show that the opacity variations are in agreement with ice mantles growth, but are consistently lower than the expected theoretical values.

5.1.2 Gas emission, studying deuterated methanol

The third Chapter of this thesis is focused on the study of the first map of deuterated methanol towards a pre-stellar core. This map was simultaneously studied with those of methanol, formaldehyde, single and doubly deuterated formaldehyde and carbon monoxide, as all of these molecules are connected with deuterated methanol in its formation pathway.

The emission of deuterated methanol is consistent with the theoretical predictions of CH_2DOH being formed on the dust surfaces, i.e. similarly to CH_3OH. Its emission is enhanced closer to the center of the core compared to methanol, where the D/H ratio increases due to the depletion of CO onto the dust grains. The deuterium fractionation also shows its maximum value towards the center, with a value of 0.08±0.02. This indicates that deuterated methanol is tracing an outer layer compared to molecules like N_2D^+ and NH_2D (Caselli et al. 2002b; Crapsi et al. 2007). D_2CO and HDCO show more centrally concentrated emission than deuterated methanol, showing a high degree of deuteration of HDCO. But unfortunately, the observations presented here need to improve in sensitivity and resolution to be able to shed light on how its distribution is seen. Interestingly, H_2CO shows a ring-like structure, depleting towards the center and showing two maxima, one coinciding with that of $C^{17}O$, and another one towards the south-west. This second maxima

is interesting, as it is a region where carbon chains are abundant (Spezzano et al. 2016), and this suggests that gas phase production of H_2CO via reactions involving hydrocarbons efficiently take place in regions where C is not completely locked in CO. All these results, when compared with the abundances given by two chemical models applied to the physical structure of L1544, tell us that more theoretical and laboratory work is needed, and that the inclusion of quantum tunneling and reactive desorption is needed.

5.2 Future work

The study of the dust emission led us to the important conclusion that interferometric observations are needed to really understand the central few hundred au, as the density and the opacity there are still not known. Keto & Caselli (2010) showed that they needed very high density in the center of the core in order to model the emission seen in different tracers. However, this inner structure has not been studied yet. In this context, two proposals were accepted during the period of this thesis, in order to study the continuum emission of L1544 at 9 mm (with the VLA) and at 3 mm (with NOEMA).

In addition, the spectra obtained for the emission of CH_2DOH, CH_3OH, and $C^{17}O$ presented in Chapter 3 were observed with high spectral resolution, allowing us to study the centroid velocities and the line widths of these tracers. Punanova et al. (2018) showed that complex kinematics may be playing a role in L1544, with possible slow shocks or gentle accretion of material towards the center of the core. The kinematic study will be presented in the second part of the paper on deuterated methanol. In the following section I will present some preliminary results.

5.2.1 Kinematics

Results

The centroid velocities and line widths have been derived for the lines CH_3OH ($2_{0,2}$-$1_{0,1}$, A^+), CH_3OH ($2_{1,2}$-$1_{1,1}$, E_2), CH_2DOH ($2_{0,2}$-$1_{0,1}$), CH_2DOH ($3_{0,3}$-$2_{0,2}$), and $C^{17}O$ (1-0), by performing a Gaussian fit of the spectral profile, pixel by pixel. In the case of $C^{17}O$ (1-0), the whole hyperfine structure was considered. The maps for the centroid velocities can be found in Figs. 5.1, 5.2, and 5.3 for CH_3OH, CH_2DOH, and $C^{17}O$, respectively. The maps for the line widths can be found in Figs. 5.4, 5.5, and 5.6. As a summary, in Table 5.1, the values of the V_{LSR} and σ_v at the dust and methanol peaks are presented.

CH_2DOH presents bluer velocities by $\sim$0.3 km s^{-1} than methanol or $C^{17}O$. Given the spectral resolution ($\sim$0.04-0.07 km s^{-1}), the uncertainties in the rest frequencies and the error in the fit ($\lesssim$0.02 km s^{-1}), this discrepancy for CH_2DOH is significant, as already discussed in Bizzocchi et al. (2014).

All molecular lines present redder velocities toward the center compared to the methanol peak. This trend is clearer in the centroid velocity map of $C^{17}O$ (see Fig. 5.3), which shows a clear gradient in velocity from the north-east to south-west. This shows however a different general trend than that of methanol and deuterated methanol (see Figs. 5.1

Table 5.1: Results of the centroid velocity and line widths from the Gaussian fit to the spectra at the dust and methanol peaks.

Line	Dust peak		Methanol peak	
	$V_{\rm LSR}$ ($\rm km\,s^{-1}$)	σ ($\rm km\,s^{-1}$)	$V_{\rm LSR}$ ($\rm km\,s^{-1}$)	σ ($\rm km\,s^{-1}$)
CH_3OH ($2_{0,2}$-$1_{0,1}$, A^+)	7.204±0.004	0.135±0.004	7.176±0.003	0.130±0.003
CH_3OH ($2_{1,2}$-$1_{1,1}$, E_2)	7.195±0.005	0.135±0.005	7.171±0.003	0.123±0.003
CH_2DOH ($2_{0,2}$-$1_{0,1}$)	6.93±0.02	0.13±0.02	6.85±0.02	0.11±0.02
CH_2DOH ($3_{0,3}$-$2_{0,2}$)	6.94±0.02	0.13±0.02	6.92±0.02	0.12±0.02
$C^{17}O$ (1-0)	7.15±0.02	0.13±0.02	7.13±0.02	0.15±0.02

and 5.2), which present a velocity gradient from south-east to north-west. The map of the centroid velocity of the $C^{17}O$ (1-0) (see Fig. 5.3) provides a large scale picture of the kinematics, while CH_2DOH and CH_3OH are tracing a smaller scale picture, as they become abundant in dense core regions where CO is already significantly frozen. This indicates the presence of complex motions within the dense core, which will be explored with ALMA.

There is not a significant difference between the velocity dispersion at the center and the methanol peak, probably due to the fact that methanol indeed traces a shell around the dust peak (with size of approximately the radius of the CO depletion zone; Bizzocchi et al. 2014). Nevertheless, looking at the velocity dispersion map of CH_2DOH in Fig. 5.5 one can clearly see that CH_2DOH shows a gradient in velocity dispersion which peaks toward the south and the south-west.

Discussion

Deuterated methanol line widths show a peculiar behavior toward the south-west (see Fig. 5.5). There is a region that shows wider line widths parallel to the major axis of the core. Clemens et al. (2016) found a steep gradient in the polarization angle which coincides with the major axis of the core. This could be caused by collision or helical pitching of the magnetic field. If it is connected to the cloud dynamics, they expected to find a similar gradient in the gas velocity. However, the kinematic information available at that time did not follow this trend. Now, we see this change in velocity dispersion parallel to this ridge. Moreover, we also see that the centroid velocity map seen in $C^{17}O$ is consistent with the large scale structure rotating in the direction south-west to north-east (see Fig. 5.3); such direction coincides with the major axis of L1544. Unlike the large scale gas traced by CO, the gas toward the central zones of L1544, traced by CH_3OH and CH_2DOH, rotates mostly south-east to north-west (see Fig. 5.1). The major axis of L1544 is also a region which separates two different chemical regions (Spezzano et al. 2016). Punanova et al. (2018) found even larger line widths in the methanol peak, only observable with high resolution interferometers, which could perhaps indicate slow shocks in the cloud possibly due to

material accretion onto the core. These observations were done only toward the methanol peak, so they do not cover the region where deuterated methanol shows large line widths. Nevertheless, Punanova et al. (2018) found these large line widths in the southermost part of the observed region, thus closer to the dust peak and in the same direction as the gradient found in deuterated methanol. This scenario shows that complex dynamics are present in the cloud, and a deeper study is needed to understand what is causing the observed velocity patterns and whether magnetic fields play an important role in shaping the internal motions.

Methanol and CO line widths show a less clear gradient, although they are consistent with CH_2DOH; also, CH_2DOH present wider lines compared to CH_3OH, consistent with the fact that CH_2DOH is tracing a more central part of the core, where the contraction velocity is higher (see e.g. Keto & Caselli 2010).

Nevertheless, the kinematics seem to increase in complexity when the spectra is examined carefully at those regions where the line widths of CH_3OH and $C^{17}O$ are wider. In these regions the wide line widths are due to the presence of a second velocity component. Unfortunately, the maps of CH_2DOH are not sensitive enough to double check this, but this second velocity component is perfectly seen towards the western parts of the core in CH_3OH and $C^{17}O$. As an example, we show in Fig. 5.7 the spectra at the center and at the region where CH_3OH shows the greater line widths (see Fig. 5.4).

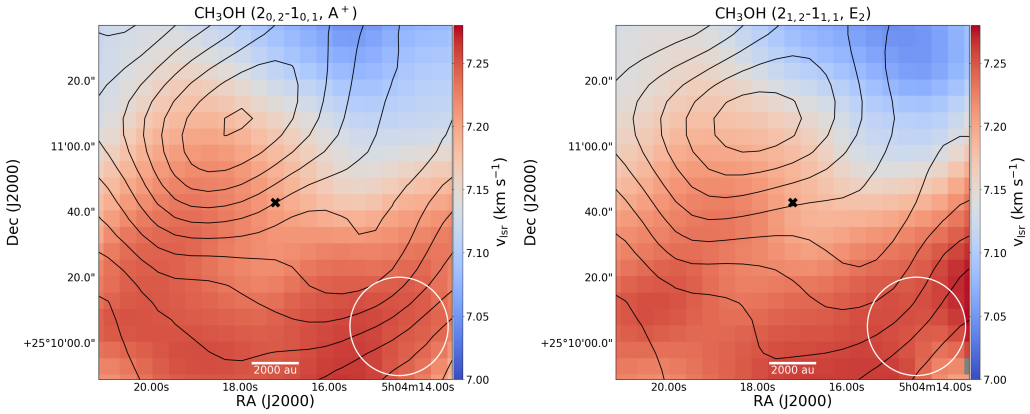

Figure 5.1: Central velocity maps derived from fitting the methanol lines A^+ (*left panel*) and E_2 (*right panel*) to Gaussian profiles. The contours represent 3σ steps of the integrated intensity maps above the 3σ detection level, with σ=0.02 K km s^{-1}. The HPBW is shown in the bottom right corner of the figure. The black cross marks the dust continuum peak.

Therefore, a deep study of the kinematics, exploring this second velocity component, is needed.

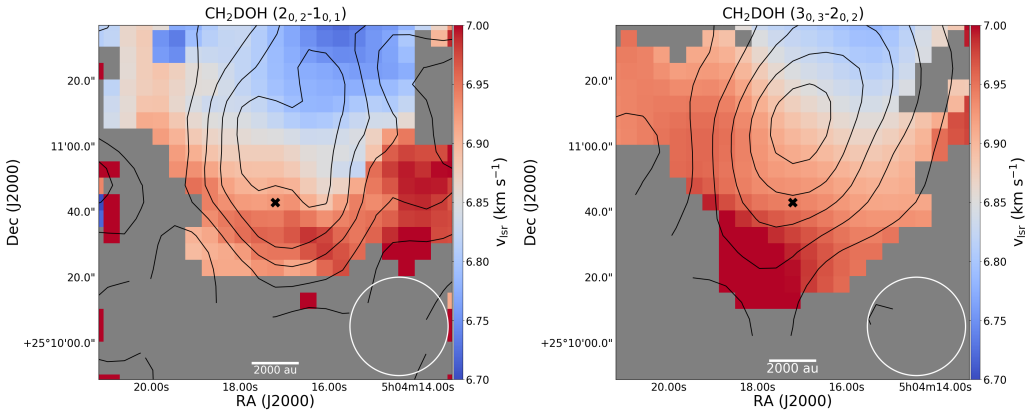

Figure 5.2: V_{LSR} map of the deuterated methanol ($2_{0,2}$-$1_{0,1}$) transition (*left panel*), and ($3_{0,3}$-$2_{0,2}$) transition (*right panel*) derived from the Gaussian fit to the data. The black contours represent increasing σ steps of the CH_2DOH integrated intensity maps above the 3σ detection level, with σ=0.005 K km s^{-1} for CH_2DOH ($2_{0,2}$-$1_{0,1}$) and σ=0.004 K km s^{-1} for CH_2DOH ($3_{0,3}$-$2_{0,2}$). The HPBW is shown in the bottom right corner of both figures. The black cross marks the dust continuum peak.

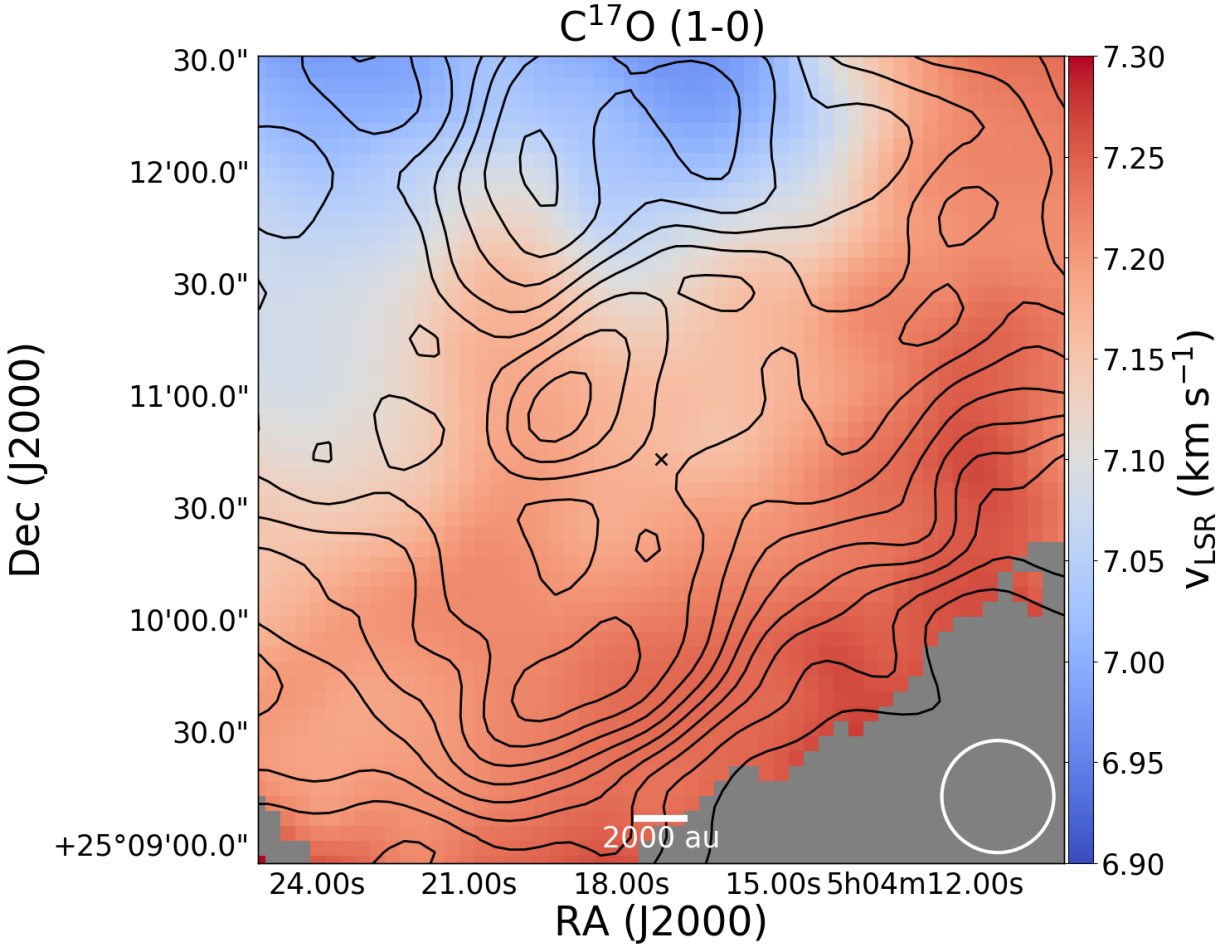

Figure 5.3: $V_{\rm LSR}$ map of $C^{17}O$ (1-0) line. The black contours represent increasing σ steps of the integrated intensity above the 3σ detection level, with σ=0.014 K km s^{-1}. The HPBW is shown in the bottom right corner of the figure. The black cross marks the dust continuum peak.

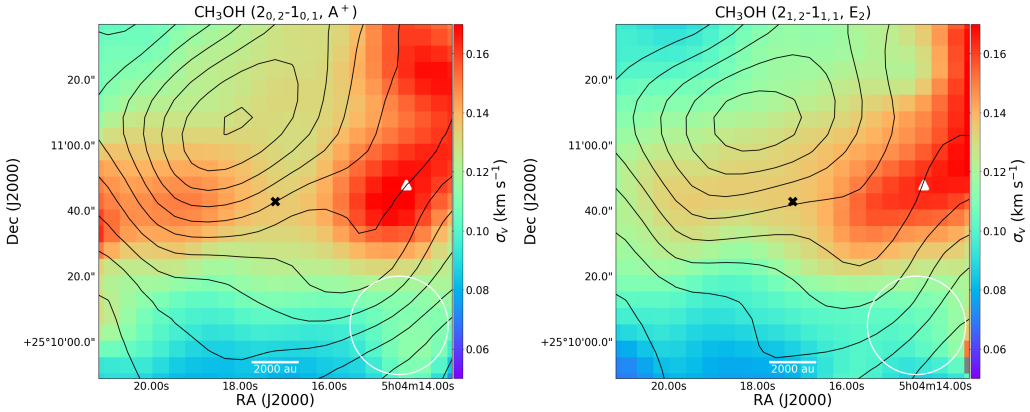

Figure 5.4: Line width maps derived from fitting the methanol lines A^+ (*left panel*) and E_2 (*right panel*) to Gaussian profiles. The contours represent 3σ steps of the integrated intensity maps above the 3σ detection level, with σ=0.02 K km s^{-1}. The HPBW is shown in the bottom right corner of the figure. The black cross marks the dust continuum peak, and the white triangle marks the offset position chosen for Fig. 5.7.

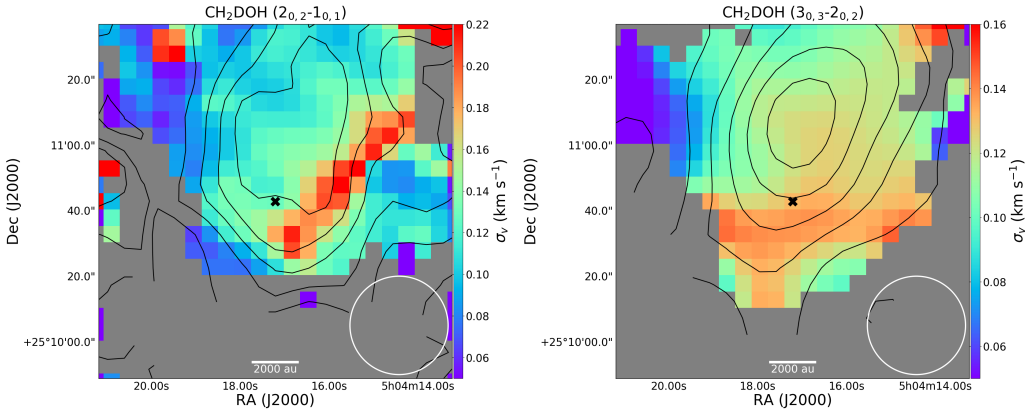

Figure 5.5: Line width maps of the deuterated methanol (2-1) transition (*left panel*), and (3-2) transition (*right panel*) derived from the Gaussian fit to the data. The black contours represent increasing σ steps of the CH_2DOH integrated intensity maps above the 3σ detection level, with σ=0.005 K km s^{-1} for CH_2DOH ($2_{0,2}$-$1_{0,1}$) and σ=0.004 K km s^{-1} for CH_2DOH ($3_{0,3}$-$2_{0,2}$). The HPBW is shown in the bottom right corner of both figures. The black cross marks the dust continuum peak.

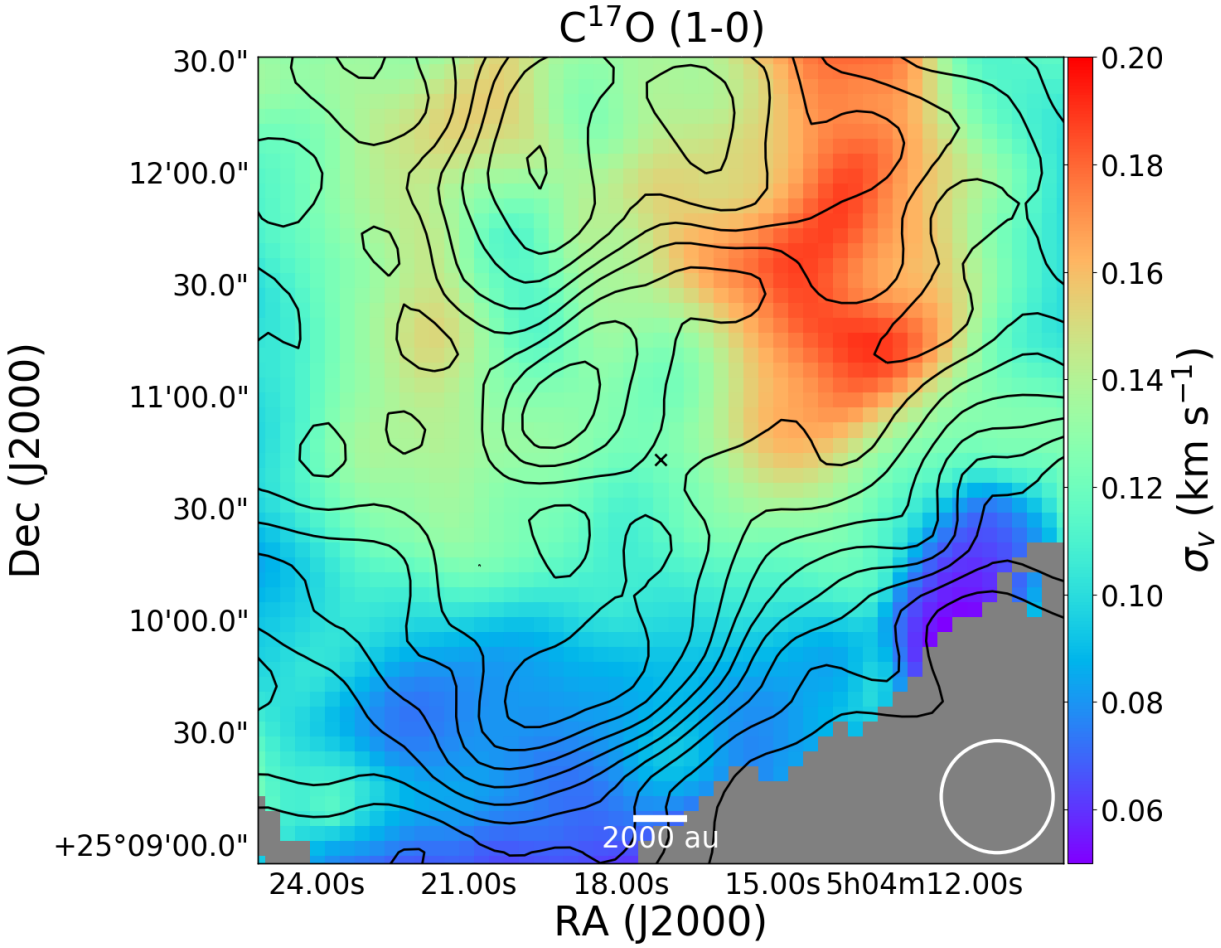

Figure 5.6: Line width map of $C^{17}O$ (1-0) line. The black contours represent increasing σ steps of the integrated intensity above the 3σ detection level, with σ=0.014 K km s^{-1}. The HPBW is shown in the bottom right corner of the figure. The black cross marks the dust continuum peak.

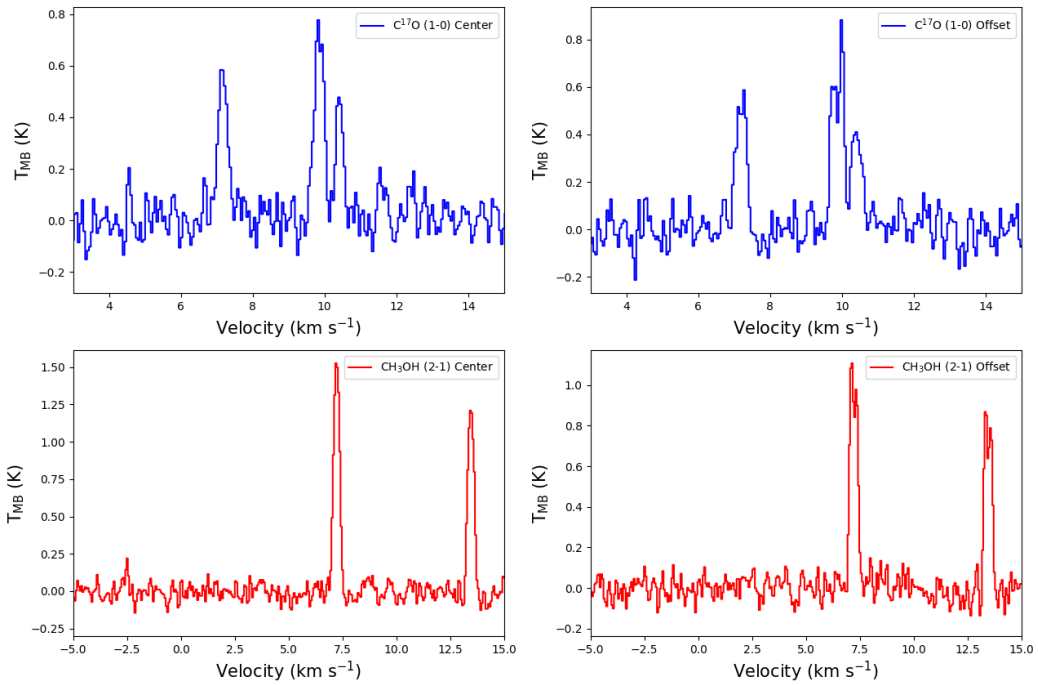

Figure 5.7: Spectra found at the center of the core (*left panels*) and at an offset position from the center (*right panels*) for the $C^{17}O$ (1-0) line (*top panels*) and the CH_3OH (2-1) lines (*bottom panels*). The offset position has been chosen to be where CH_3OH shows wider line widths towards the western part of the core (indicated with a white triangle in Fig. 5.4).

Appendix A

Complementary material for Chapter 2

A.1 NIKA and *Herschel*/SPIRE filtering

Sadavoy et al. (2016) presented a way to filter *Herschel*/SPIRE large scale emission, based on the work of Wang et al. (2015), by cutting off the low spatial frequencies in the Fourier domain based on their GISMO 2 mm data. To study this method with our data, we smoothed all the bands to the lowest resolution ($\sim$38.5″, corresponding to the 500 μm SPIRE band; these maps can be seen in Fig. A.1) and performed a Fourier transform on all the maps. We then obtained the radial amplitude profile of the 2 mm frequency domain maps by averaging in rings one pixel wide, as done in Sadavoy et al. (2016). This profile is shown in Fig. A.2, together with that at 1.2 mm for comparison. This profile is then fitted with an exponential function, and the fit is used to construct a mask for SPIRE maps in the same manner as described in Sadavoy et al. (2016).

There is not be much difference between using the 1.2 mm map and the 2 mm map as a mask as both profiles have identical slopes within the errors (see Fig. A.2). This is also an indication of similar filtering in both bands, as expected from the similarity of the fields of view and as predicted by Adam et al. (2015).

The final filtered SPIRE maps are shown in Fig. A.3 for the Fourier transform method and in Fig. A.4 for the method used in this work (see Section 2.3), where an aperture is chosen to subtract the emission from the original maps. In the first case, they show very centrally concentrated emission with a decrease in the peak surface brightness of 40, 60, and 50% for the 500, 350, and 250 μm bands, respectively, with respect to the original SPIRE maps. The peak emission we obtained with the aperture filtering method, compared with the Fourier transform method results, gives differences of approximately 30, 25, and 40% for the 500, 350, and 250 μm bands, respectively. As the two shorter wavelengths bands see an increase in surface brightness, there is an increase in the spectral index and the opacity, obtaining in this case $\beta = 2.5 \pm 0.6$ and $\kappa_{250\mu m} = 0.28 \pm 0.14$ cm^{2}g^{-1}. Although this is still within our uncertainties, this opacity and spectral index do not reproduce the observed NIKA millimeter emission as accurately: the ratio between the observed emission and the model is 1.3 in both cases. This difference can be due to the high concentration

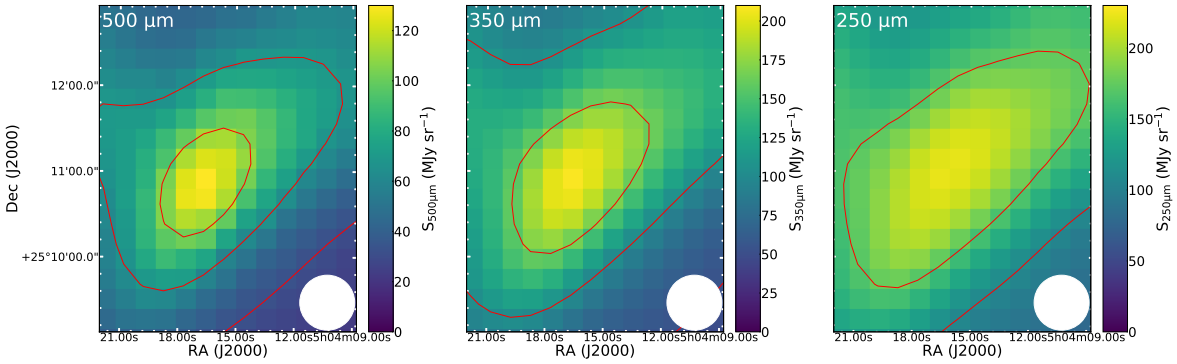

Figure A.1: Original *Herschel*/SPIRE maps after smoothing to the lowest resolution and before applying any filtering method. The contours represent steps of 25% of the peak emission at each band. The HPBW, which corresponds to the higher resolution of *Herschel*/SPIRE (38.5″), is shown by the white circle in the bottom right corner.

of emission in the central pixel, and this may be a source of error. It could artificially increase the peak emission, making the slope of the spectral energy distribution increase as well. We therefore used the method that reproduces the millimeter observations more closely, although the two methods give similar results within the uncertainties.

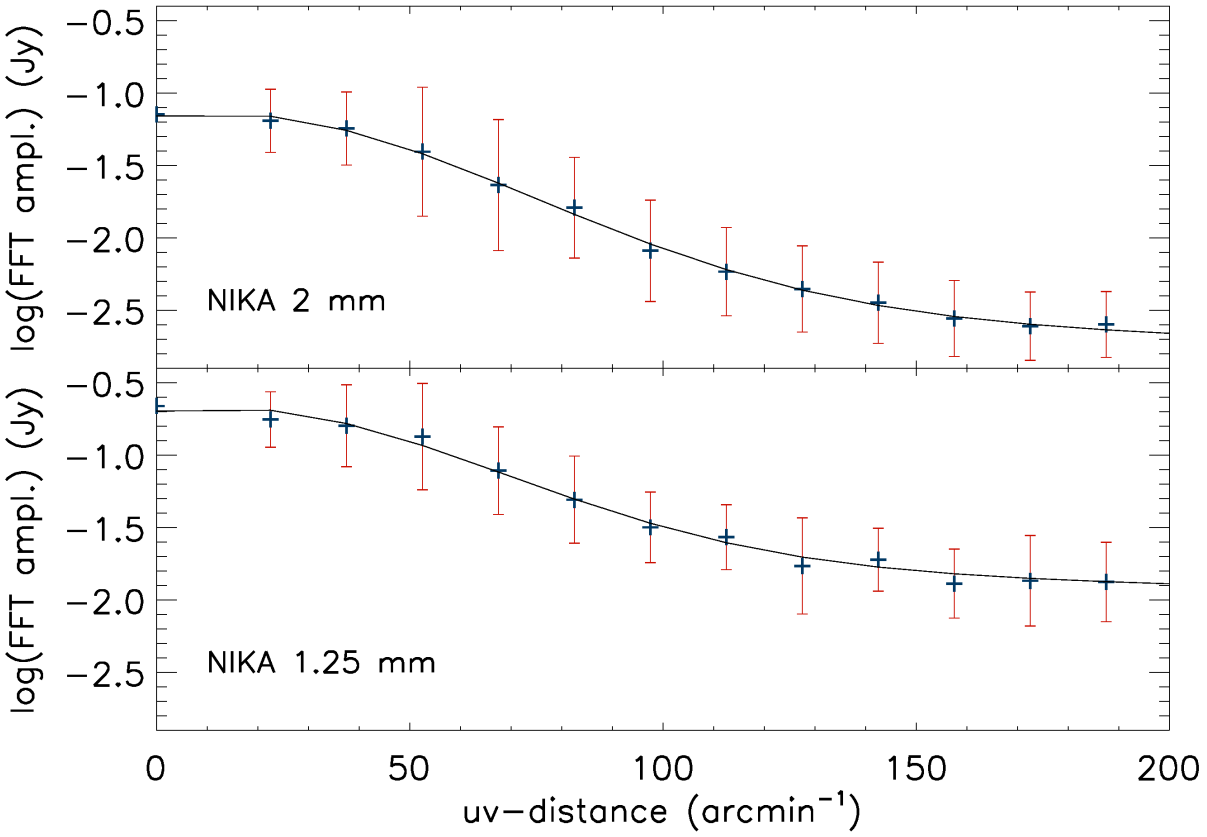

Figure A.2: Fourier amplitude profiles of the 1.2 mm (*top*) and 2 mm (*bottom*) data in the frequency domain. The profiles are obtained by averaging in rings of 1 pixel in width at different distances from the center of the Fourier transformed emission maps. The profile at 2 mm is used to derive a mask, which is applied to the *Herschel*/SPIRE data in order to filter out the large-scale emission.

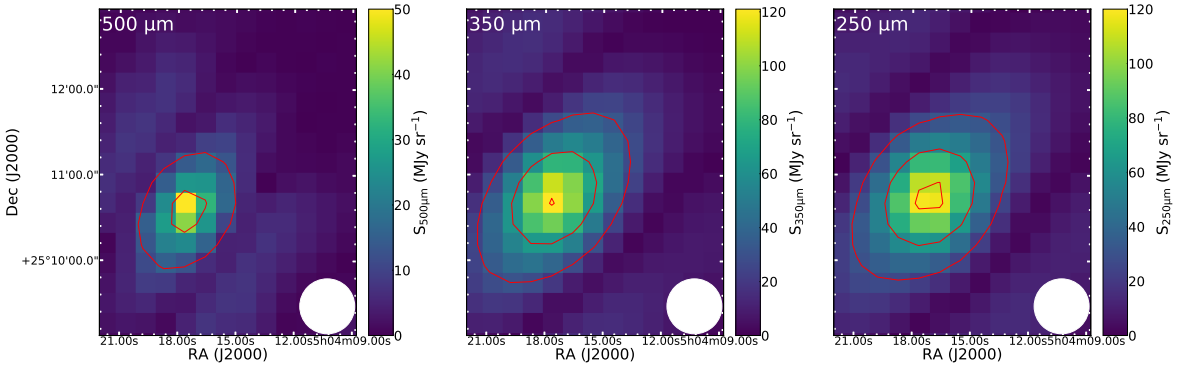

Figure A.3: Resulting *Herschel*/SPIRE maps after applying the filtering method from Sadavoy et al. (2016). The contours represent steps of 25% of the peak emission at each band. The emission is seen to be centrally concentrated in the central pixels.

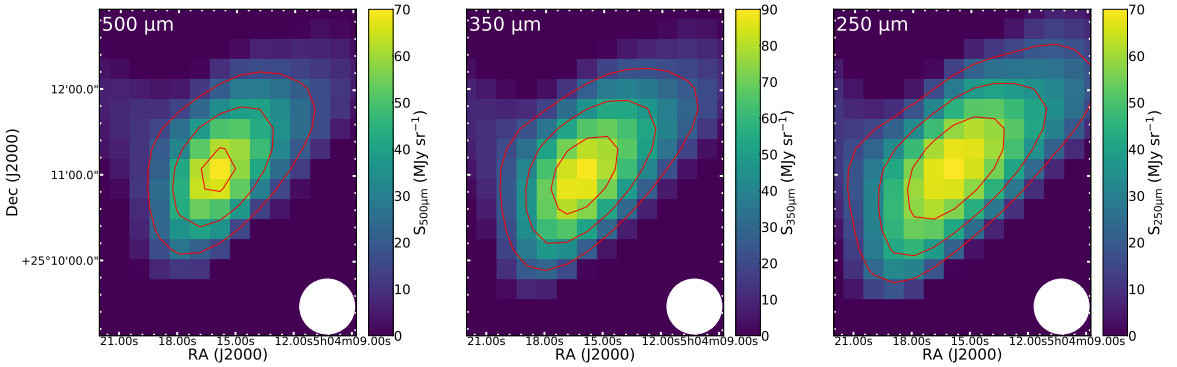

Figure A.4: Resulting *Herschel*/SPIRE maps after applying the filtering method used in this work, extracting the emission around the core where no emission is detected in mm wavelengths. The contours represent steps of 25% of the peak emission at each band.

Appendix B

Complementary material for Chapter 3

B.1 Integrated intensity maps

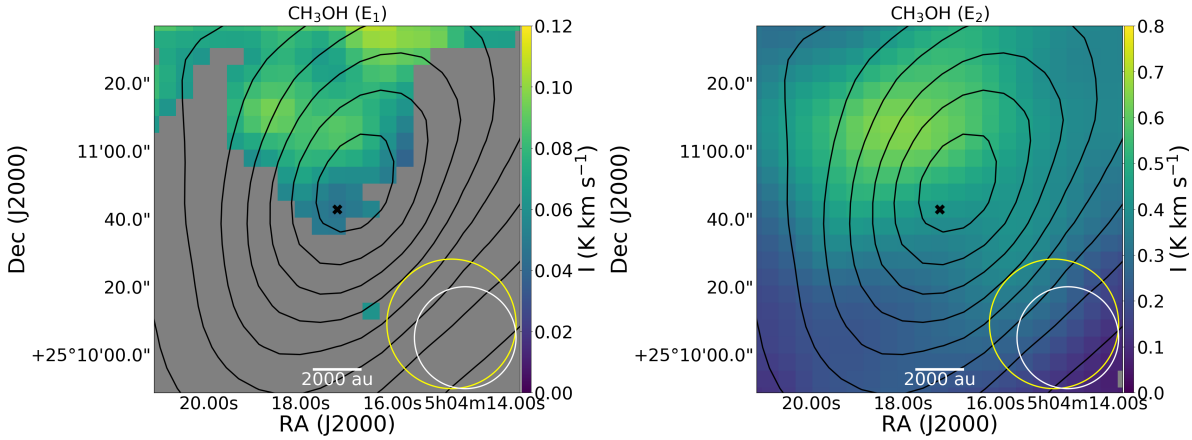

Figure B.1: Integrated intensity maps of the E_1 (*left panel*), and E_2 (*right panel*) methanol transitions. Only pixels with flux values above a 3σ detection level are presented. The black contours represent increasing 10% steps of the N_{H_2} column density map, derived by Spezzano et al. (2016). The noise in the integrated intensities is 0.02 K km s^{-1}. The HPBWs are shown in the bottom right corner of the figures, in yellow for *Herschel*/SPIRE and in white for the 30 m telescope. The black cross marks the dust continuum peak.

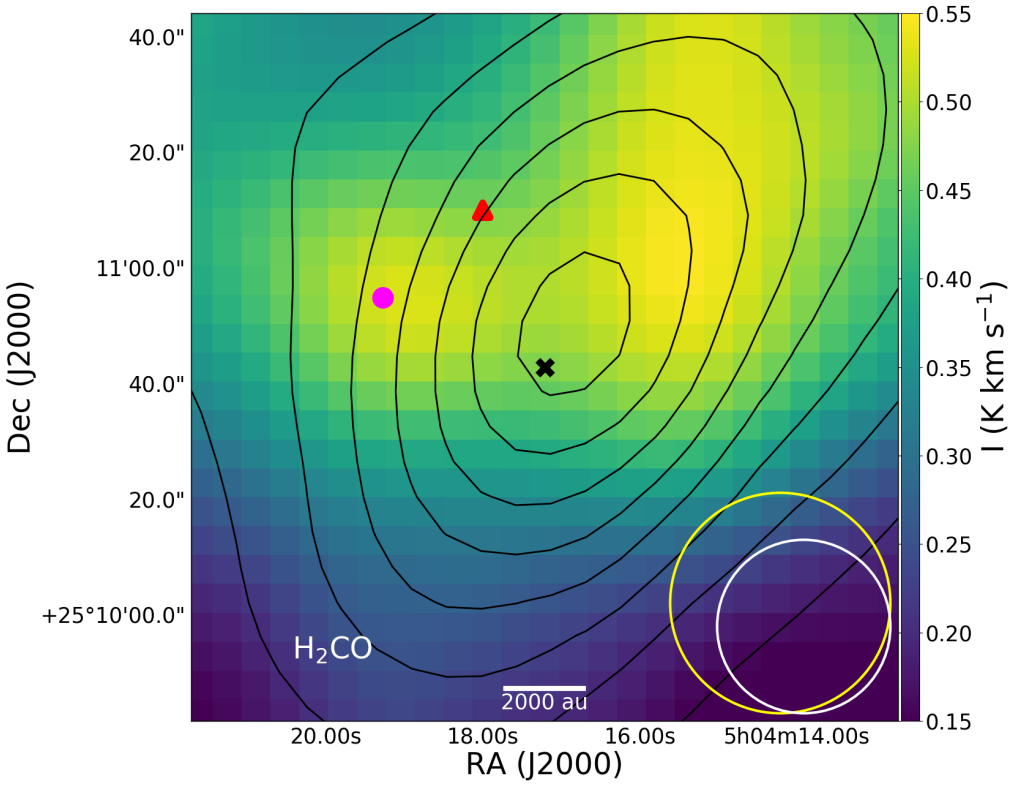

Figure B.2: Integrated intensity map of the H_2CO ($2_{1,2}$-$1_{1,1}$) line. The black contours represent increasing 10% steps of the N_{H_2} column density map, derived by Spezzano et al. (2016). The error in the integrated intensity is 0.014 K km s^{-1}. The HPBWs are shown in the bottom right corner of the figures, in yellow for *Herschel*/SPIRE and in white for the 30m telescope. The black cross marks the dust continuum peak, the red triangle the methanol peak and the pink circle the $C^{17}O$ peak.

B.2 Column density maps

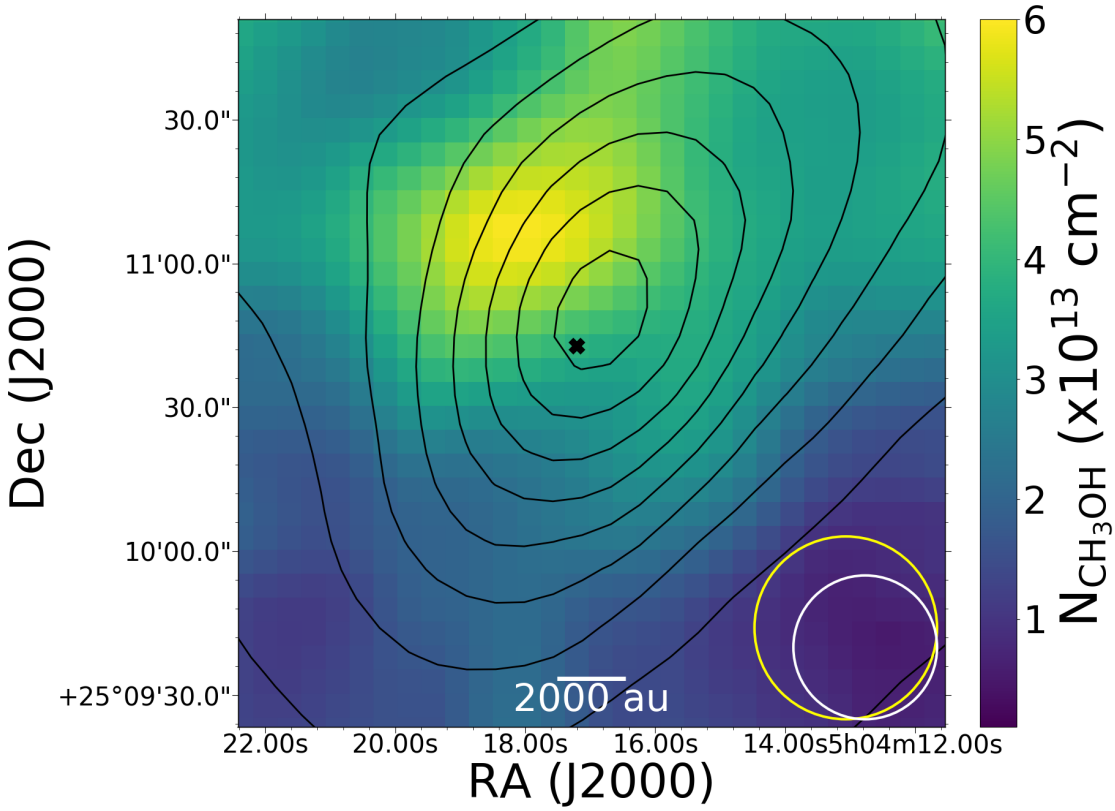

Figure B.3: Column density map of CH_3OH derived as explained in Section 3.5.1. The black contours represent increasing 10% steps of the N_{H_2} column density map, derived by Spezzano et al. (2016). The HPBWs are shown in the bottom right corner of the figures, in yellow for *Herschel*/SPIRE and in white for the 30m telescope. The black cross marks the dust continuum peak.

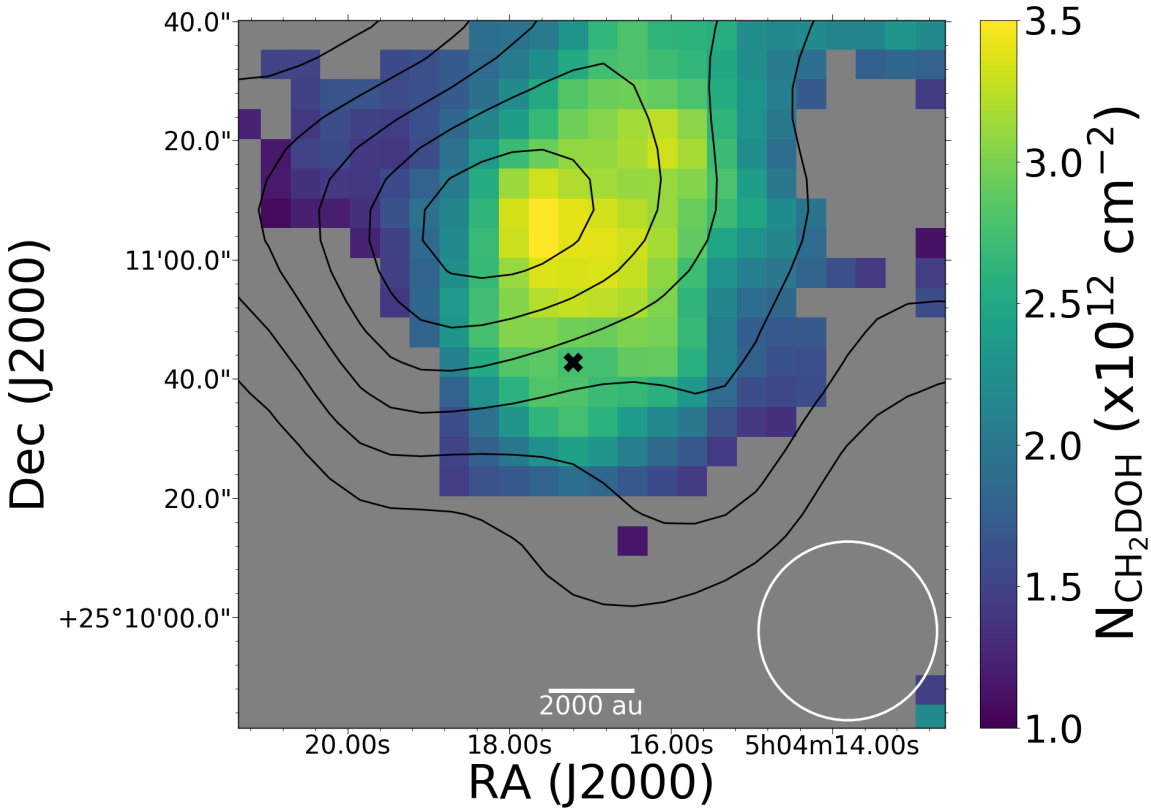

Figure B.4: Column density map of CH_2DOH derived as explained in Section 3.5.1. The black contours represent 10% steps in the CH_3OH column density. The black cross marks the dust continuum peak. The HPBW is shown in the bottom right corner.

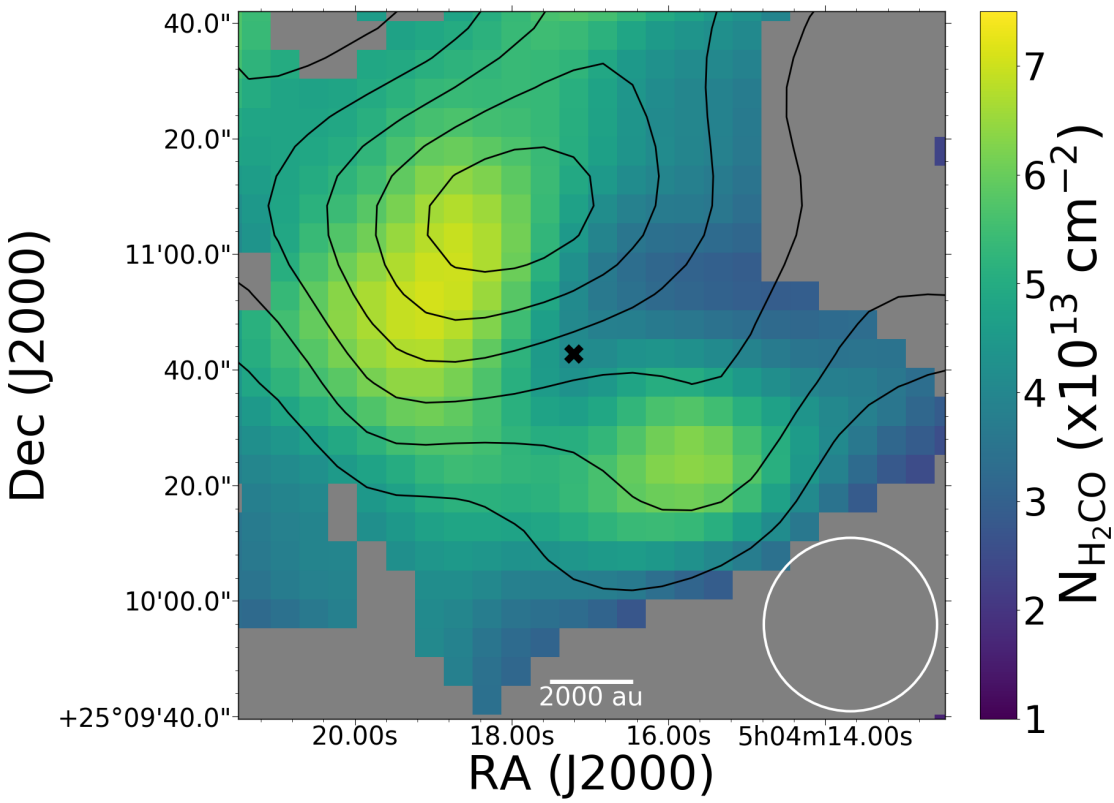

Figure B.5: Column density map of H_2CO derived as explained in Section 3.5.1. The black contours represent 10% steps in the CH_3OH column density. The black cross marks the dust continuum peak. The HPBW is shown in the bottom right corner.

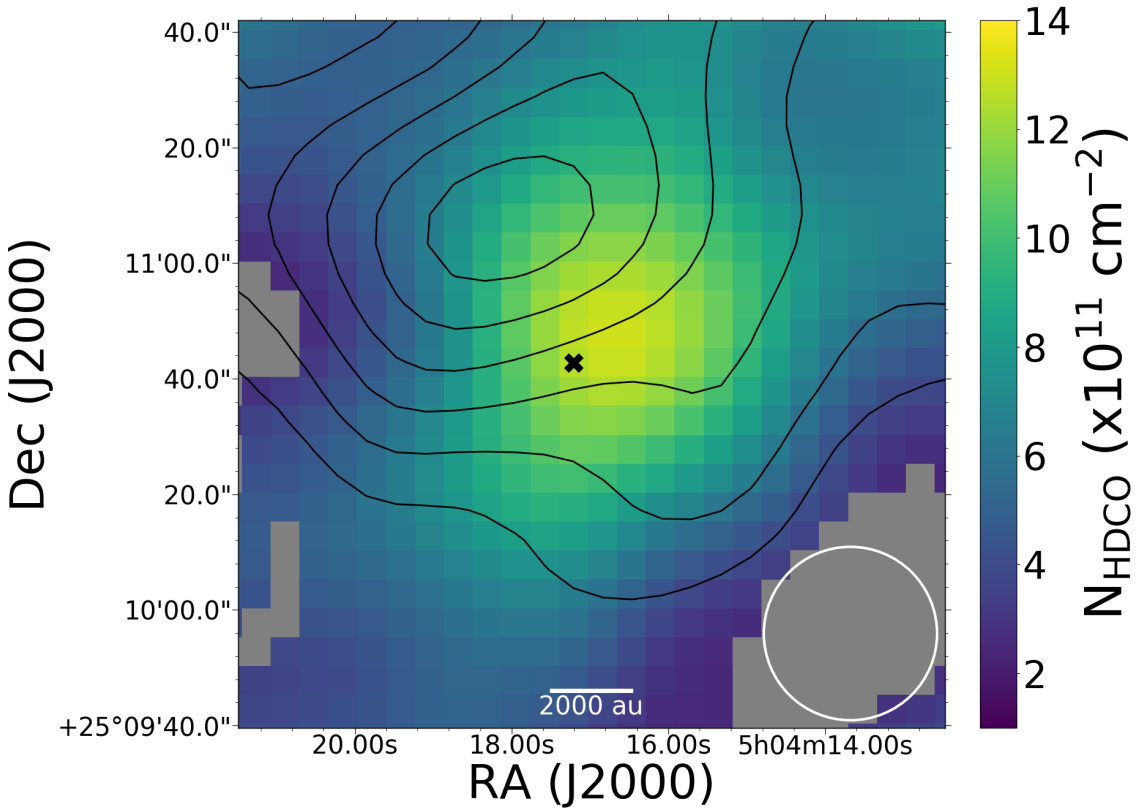

Figure B.6: Column density map of HDCO derived as explained in Section 3.5.1. The black contours represent 10% steps in the CH_3OH column density. The black cross marks the dust continuum peak. The HPBW is shown in the bottom right corner.

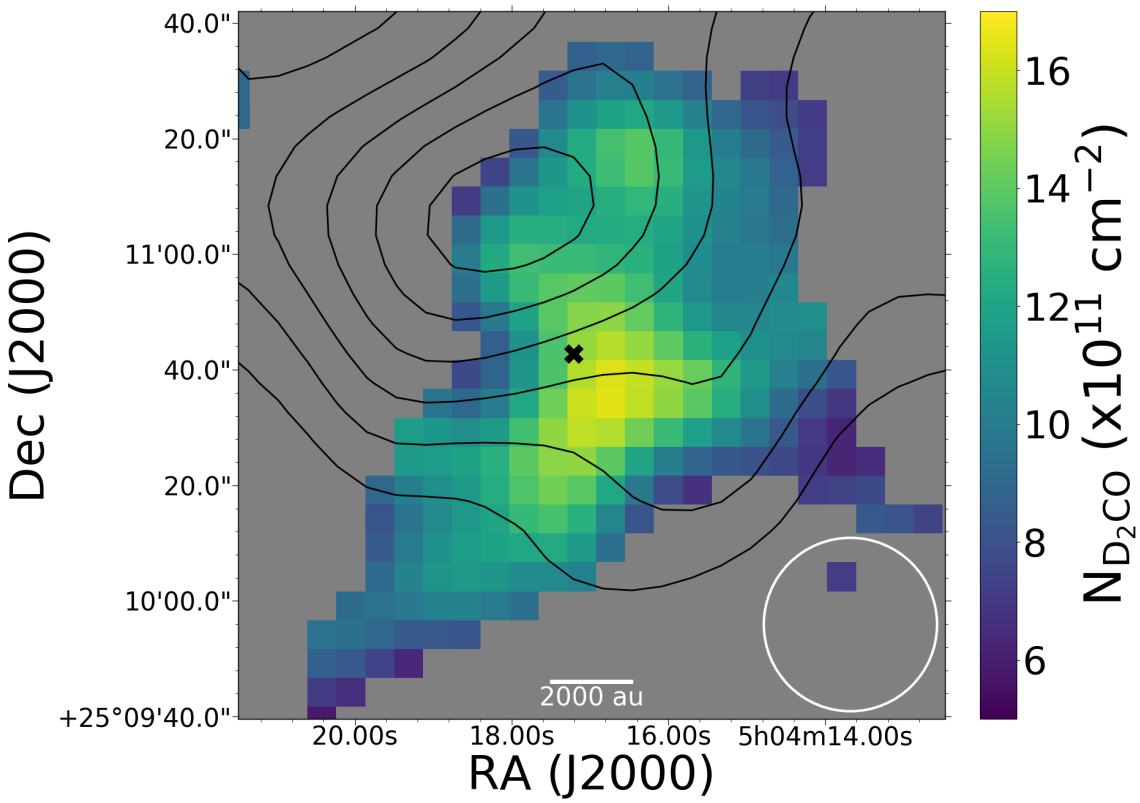

Figure B.7: Column density map of D_2CO derived as explained in Section 3.5.1. The black contours represent 10% steps in the CH_3OH column density. The black cross marks the dust continuum peak. The HPBW is shown in the bottom right corner.

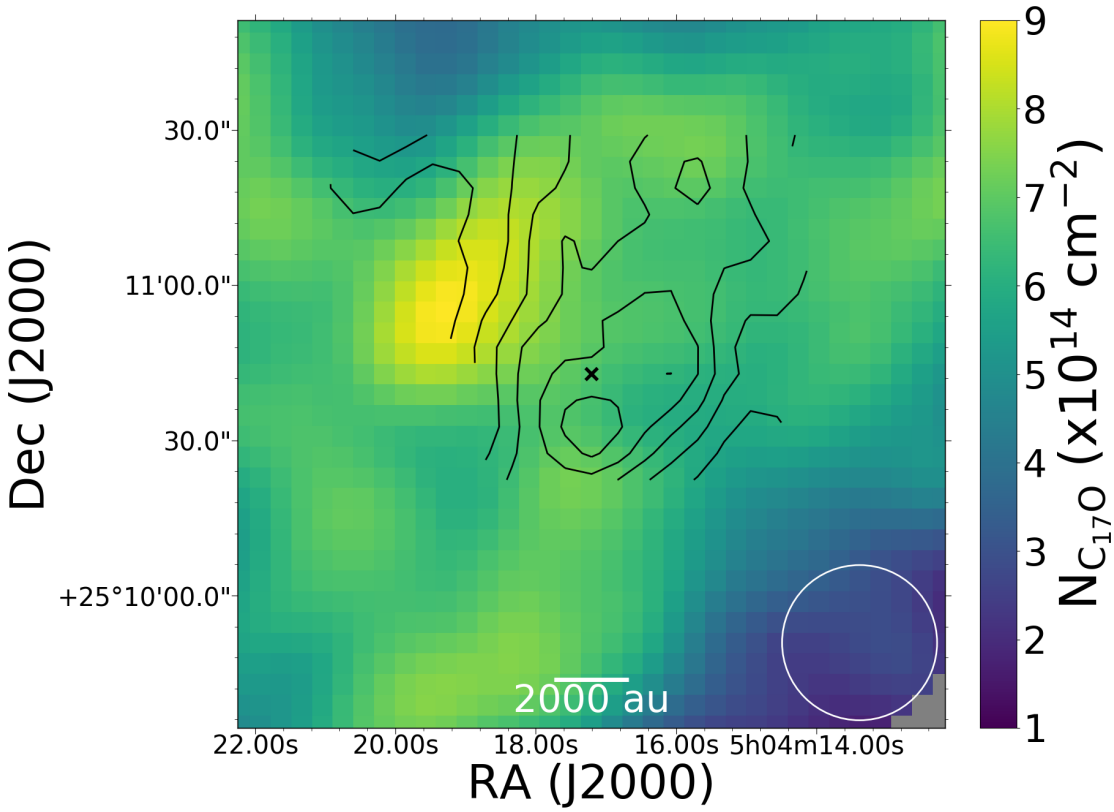

Figure B.8: Column density map of $C^{17}O$ derived as explained in Section 3.5.1. The black contours represent 10% steps in the methanol deuterium fraction. The black cross marks the dust continuum peak. The HPBW is shown in the bottom right corner.

B.3 Errors on the deuteration maps

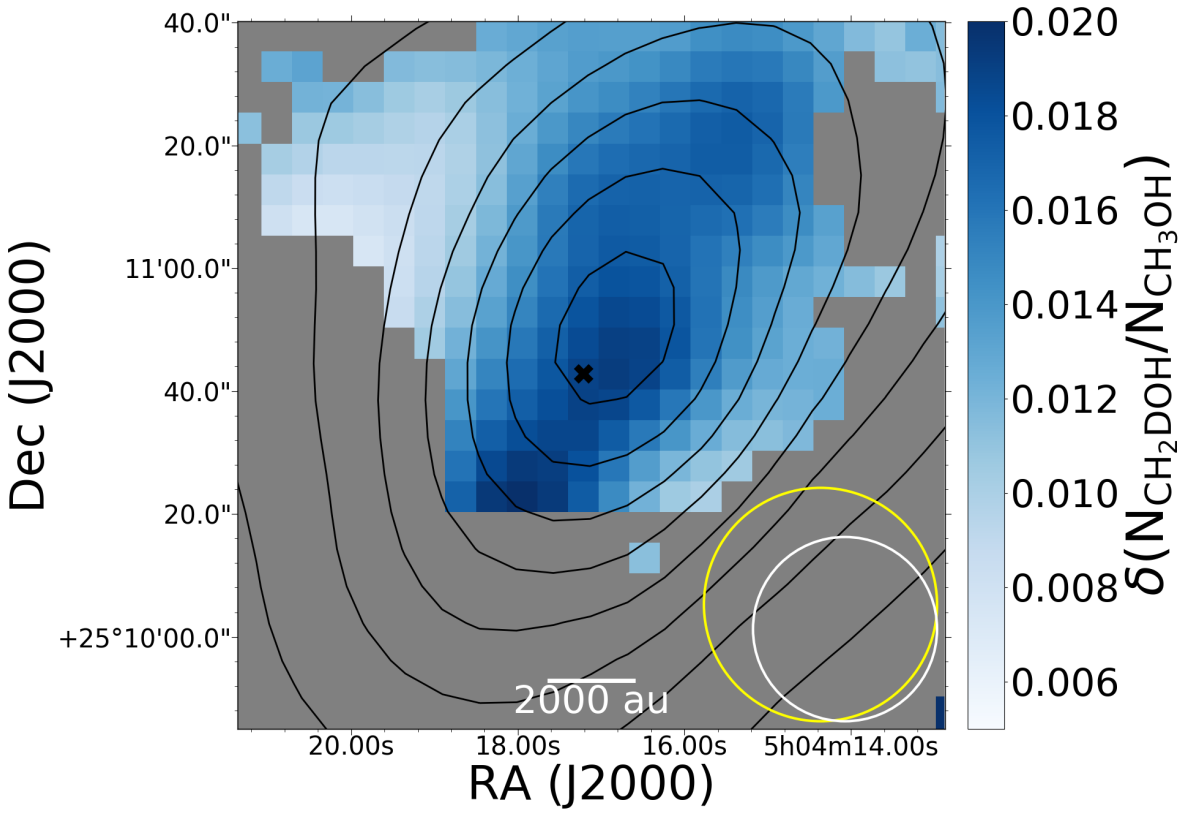

Figure B.9: Error on the ratio between N(CH_2DOH) and N(CH_3OH). The black contours represent increasing 10% steps of the peak of the *Herschel* N(H_2) map, presented by Spezzano et al. (2016). The HPBWs are shown in the bottom right corner of the figures, in yellow for *Herschel*/SPIRE and in white for the 30m telescope. The black cross marks the dust continuum peak.

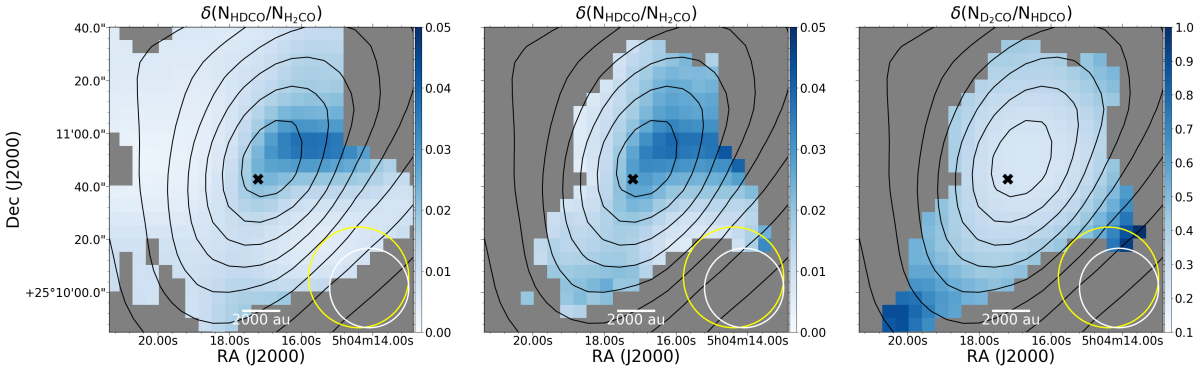

Figure B.10: Error on the ratio between N(HDCO) and N(H_2CO) (*left panel*) and N(D_2CO) and N(H_2CO) (*right panel*). The black contours represent increasing 10% steps of the peak of the Herschel N(H_2) map, presented by Spezzano et al. (2016). The HPBWs are shown in the bottom right corner of the figures, in yellow for *Herschel*/SPIRE and in white for the 30m telescope. The black cross marks the dust continuum peak.

Appendix C

Complementary material for Chapter 4

C.1 Modeling based on previous results

Here we compare the observations with the modeled emission using the physical structure from Keto et al. (2015), following the same steps as in Section 4.5.2, but using the spectral index and the opacity values from Chacón-Tanarro et al. (2017), which are $\kappa_{250\mu\mathrm{m}} = 0.2\,\mathrm{cm^2 g^{-1}}$ and $\beta = 2.3$. This is to check the results following exactly the same procedure of Chacón-Tanarro et al. (2017). The results are presented in Fig. C.1. As it is seen, the model does not reproduce the observations.

C.2 A_V from *Herschel*/SPIRE

To derive a value for the visual extinction, A_V, corresponding to the external low density layer of the cloud, we take the $N_{\mathrm{H_2}}$ map from Spezzano et al. (2016), derived from the emission of *Herschel*/SPIRE, and transformed it into A_V using the following equation (Bohlin et al. 1978):

$$N_{\mathrm{H_2}} = 9.4 \times 10^{20} \mathrm{cm^{-2}} (A_V/\mathrm{mag}). \tag{C.1}$$

This produces the A_V map presented in Fig. C.2. At distances far away from the dust continuum peak (>10 000 au), the A_V has a value of ∼2 mag. This is not seen in the ground based millimeter maps as this part of the cloud is filtered out. This outer layer shields the inner core structure seen in our data from the external radiation field, and therefore it affects the internal temperature.

C.3 A different type of profile

Here we consider another starting point for the derivation of the density, temperature and opacity profiles that reproduce our observations.

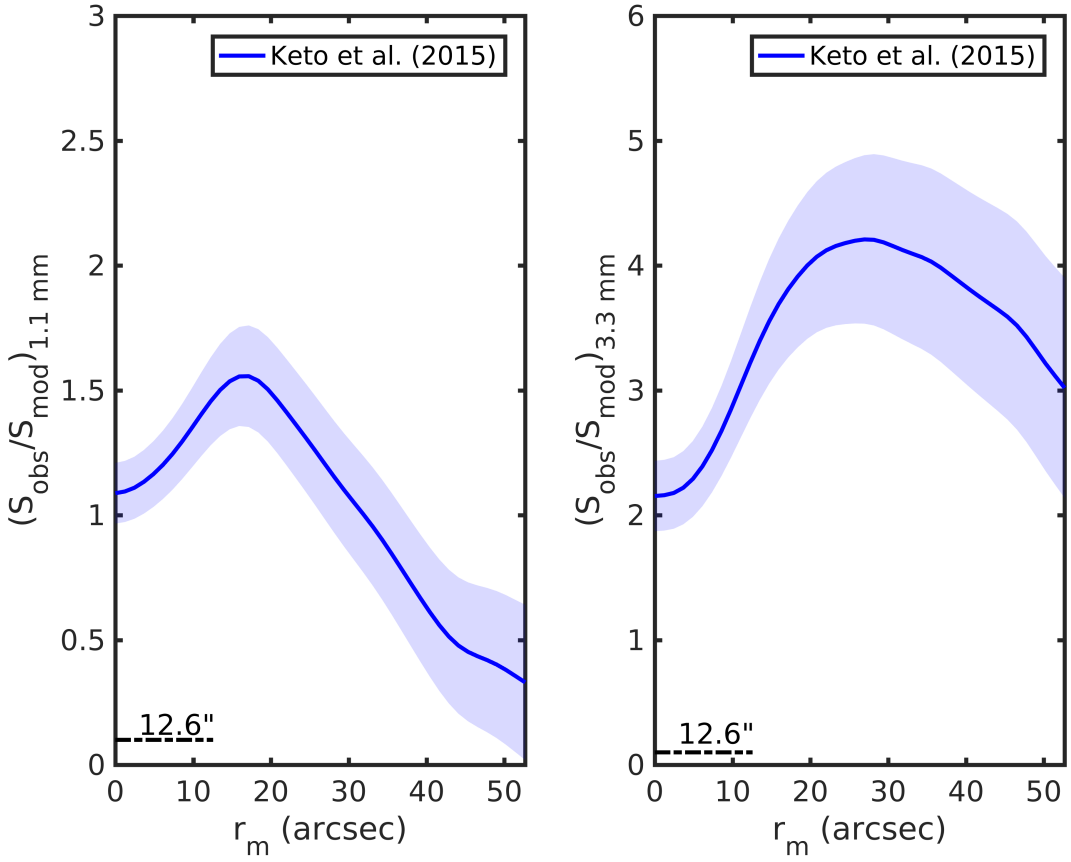

Figure C.1: Ratio between the observed emission profiles and the modeled emission profiles using the same modeling parameters as in Chacón-Tanarro et al. (2017). The shaded regions show the noise associated with the data.

From the Abel transform, one direct measurement is the factor $\kappa_\nu n_{H_2}$. Therefore we do the following:

1. $\kappa_{1.1mm} n_{H_2}$ and $\kappa_{3.3mm} n_{H_2}$ are derived from the Abel transform (Eq. (4.4)) for each band.

2. β is derived from $\beta = \frac{\log(A_1/A_3)}{\log(\nu_{1.1mm}/\nu_{3.3mm})}$, being A_1 and A_3 the right hand side of Eq. (4.4) at 1 and 3 mm, respectively.

3. The density is derived from $\kappa_{3.3mm} n_{H_2}$, assuming $\kappa_{3.3mm}$ is constant across the cloud and consistent with Ossenkopf & Henning (1994) thin ice mantles and $\beta = 2.0$, i.e. $\kappa_{3.3mm}$=0.0011 cm^{2}g^{-1}.

4. The variation of the opacity at 1.1 mm is derived from $\kappa_{1.1mm} n_{H_2}$.

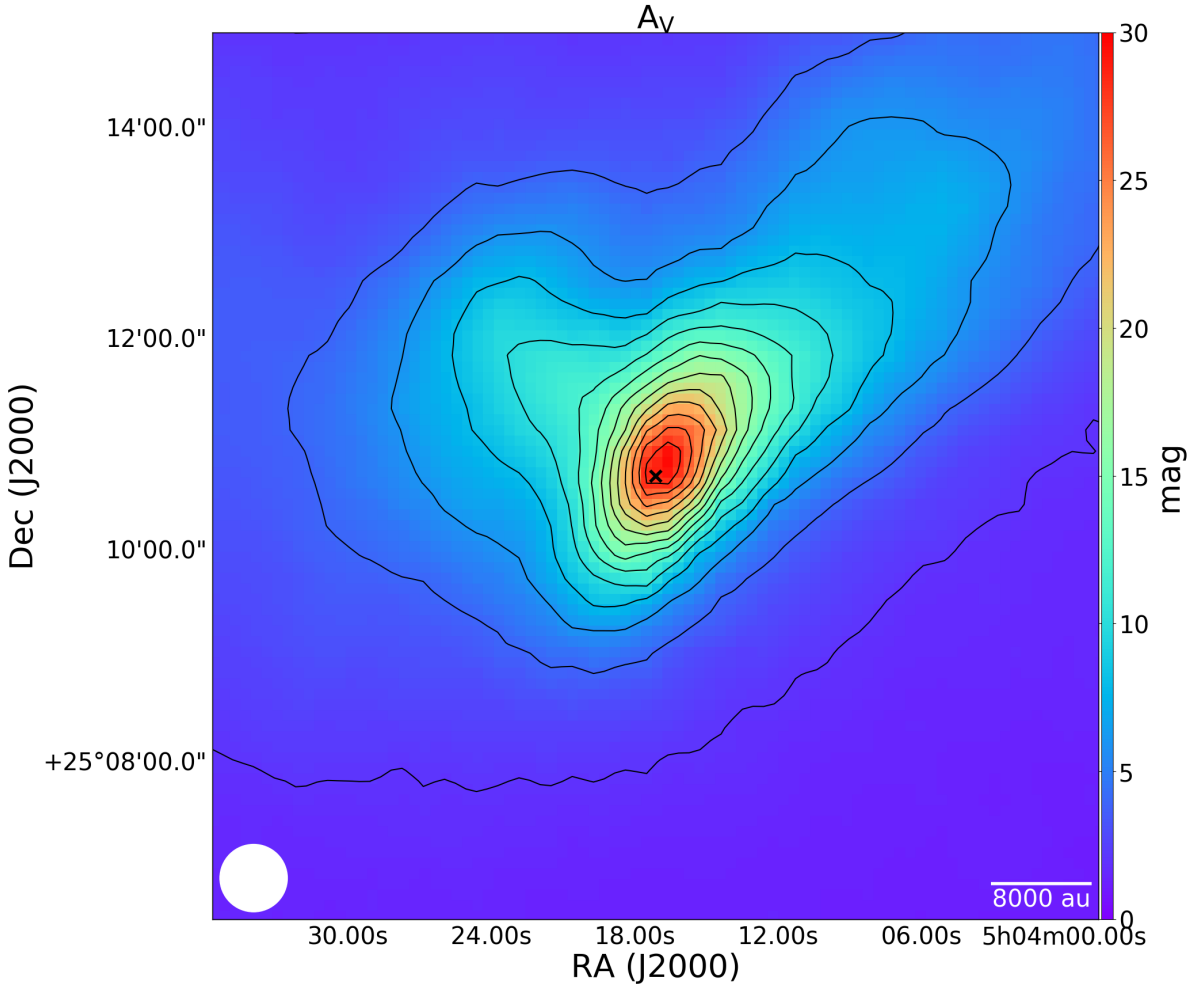

Figure C.2: Visual extinction map of L1544 derived from the N_{H_2} map from Spezzano et al. (2016). The contours represent steps of 2 magnitudes.

5. The temperature profile is derived for the opacity and spectral index variation at 1.1 mm.

Iterating the previous points until the opacity converges, we find the new density, temperature and opacity profiles in Fig. C.3 and Fig. C.4. These results reproduce the observations, as shown in Fig. C.5.

The opacities in this case are similar to those presented by Ossenkopf & Henning (1994) for thin ice mantles. However, the central density has declined below 10^6 cm^{-3}. This central density is inconsistent with previous observations (e.g. Crapsi et al. 2005) and modeling including simple chemistry and dynamics constrained by observed line profiles (Keto & Caselli 2010). We therefore follow the method presented in the main text, but ask the reader to be cautious, as more observations are needed to constrain the absolute values.

C.4 MUSTANG-2 resolution

Fig. C.6 shows the radial opacity variations derived at the intrinsic resolution of each map (9.7″ at 3.3 mm and 12.6″ at 1.1 mm), and Fig. C.7 shows the corresponding comparison between the observed and the modeled emission. The opacity at 3.3 mm at 9.7″ resolution shows differences up to 20% when compared to the same opacity derived at a resolution of 12.6″.

C.5 Grain growth model

The grain growth model used in Section 4.6.3 is based on the analytic estimation of grain growth presented by Blum (2004), which was compared with the more complex grain growth model from Ormel et al. (2009), finding a good match. For a complete description of how this model is used, see Chacón-Tanarro et al. (2017).

As discussed in Chacón-Tanarro et al. (2017), models which do not account for a density evolution of a dense core overestimate the grain sizes present in the core center by orders of magnitude. As no information about the dynamical history is available, the cloud is assumed to follow the evolution described in Keto et al. (2015): we first obtain the ratio between the maximum density at each time and the central density value which best describes the current structure of L1544; this gives percentages which provide the time evolution of the central density. Such percentages are then applied to our new density profile, obtaining an approximation of the cloud evolution with time based on a Bonnor-Ebert sphere modeling. For the evolution of the size of the inner flatter region, Equation (2) from Keto & Caselli (2010) was used.

This evolution of the density profile is seen in Fig. C.8. We stress that this is an approximation only to estimate how much can grain growth impact opacity variations at 1.1 and 3.3 mm.

The final grain distribution found reaches sizes of ∼3-4 μm in the central 2 000 au, which is consistent with the results from Ormel et al. (2009) for densities of or above $10^5\,\mathrm{cm}^{-3}$ and time evolution above 0.1 Myrs. However, transforming this to opacities using the code presented by Woitke et al. (2016), in the same way as described in Chacón-Tanarro et al. (2017), yields very light changes in the opacity (less than 0.001%), impossible to check observationally. However, this code does not include ice mantles, which could be the source of opacity change in the core: the closer to the center, the thicker the ice mantles. This needs to be checked with more complex and complete grain growth and opacity models, as well as higher angular resolution observations.

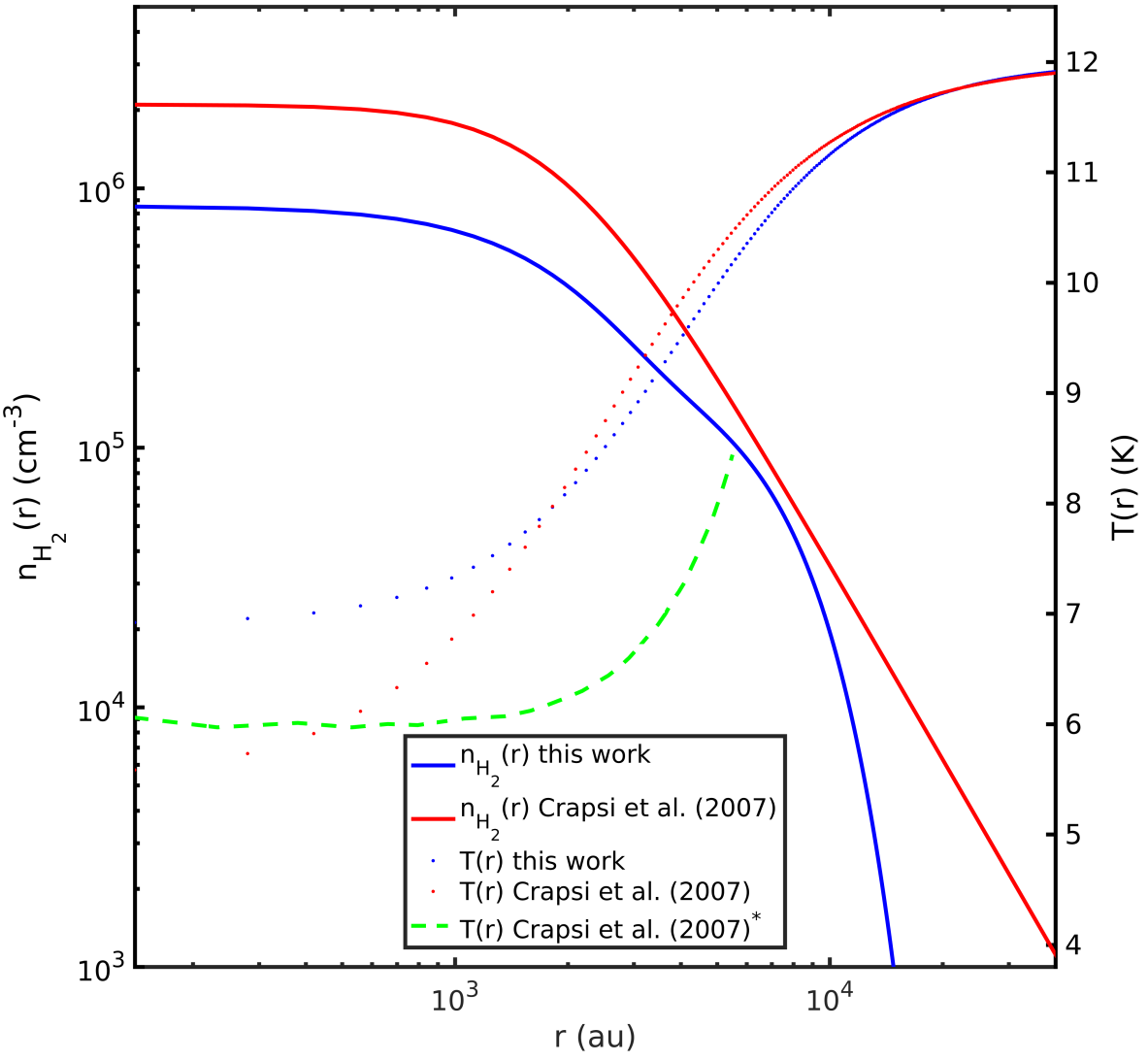

Figure C.3: New density (blue solid line) and temperature (blue dotted line) profiles derived as described in Section C.3. In red, density (solid line) and temperature (dotted line) profiles from Crapsi et al. (2007). In green, temperature profile from Crapsi et al. (2007) derived using the formulae from Zucconi et al. (2001), here Crapsi et al. (2007)*.

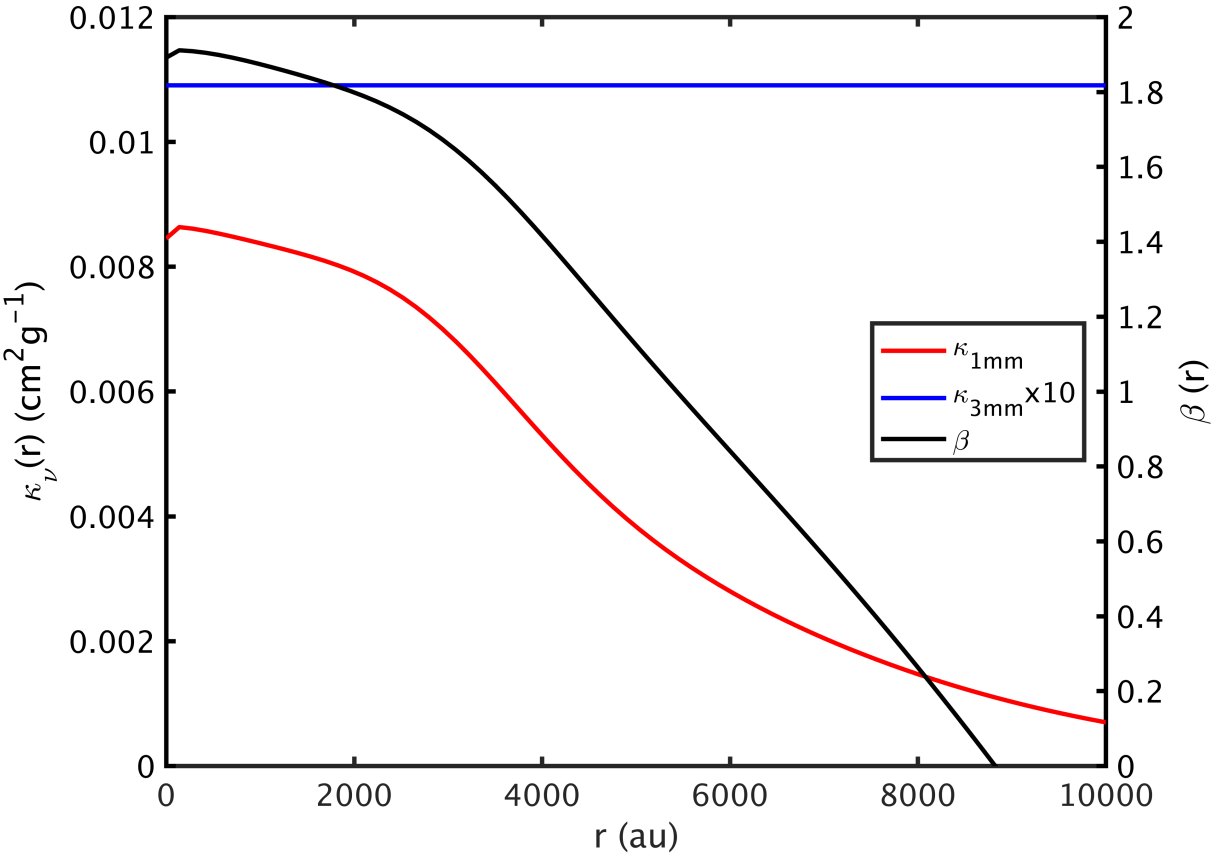

Figure C.4: Radial opacity and spectral index variations derived as described in Section C.3.

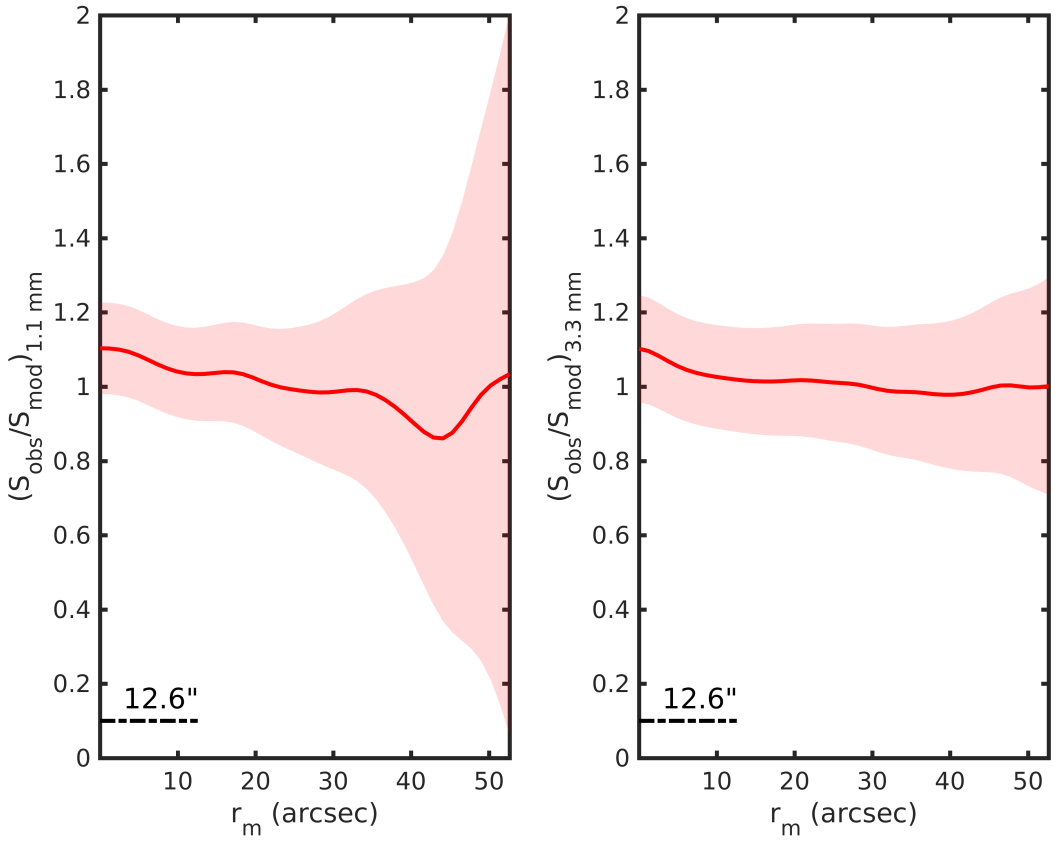

Figure C.5: Ratio between the observed emission profiles and the modeled emission profiles taking into account the radial opacity variations, and new density and temperature profiles, as explained in Section C.3. The shaded regions show the noise associated with the data.

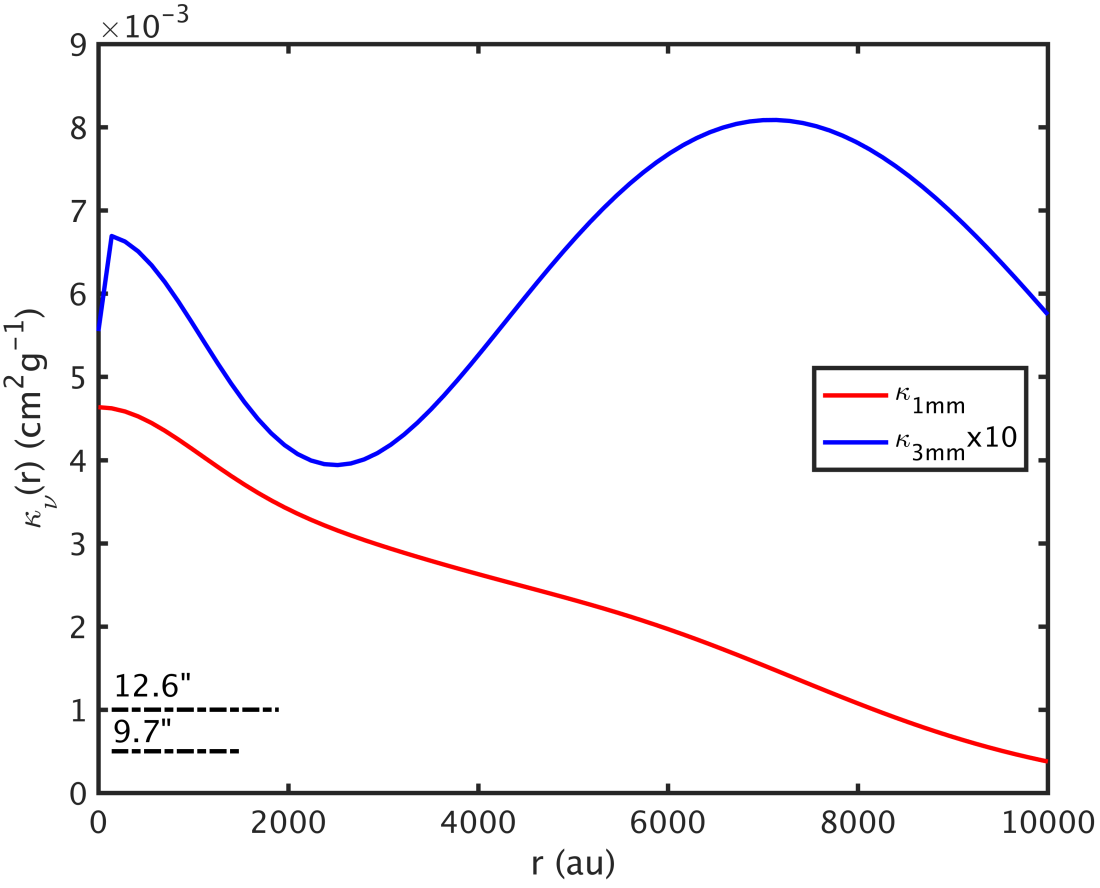

Figure C.6: Radial opacity variations derived as described in Section 4.6.1. The resolution of the opacity at 1.1 mm is 12.6″, and the one at 3.3 mm is 9.7″, both shown in the figure.

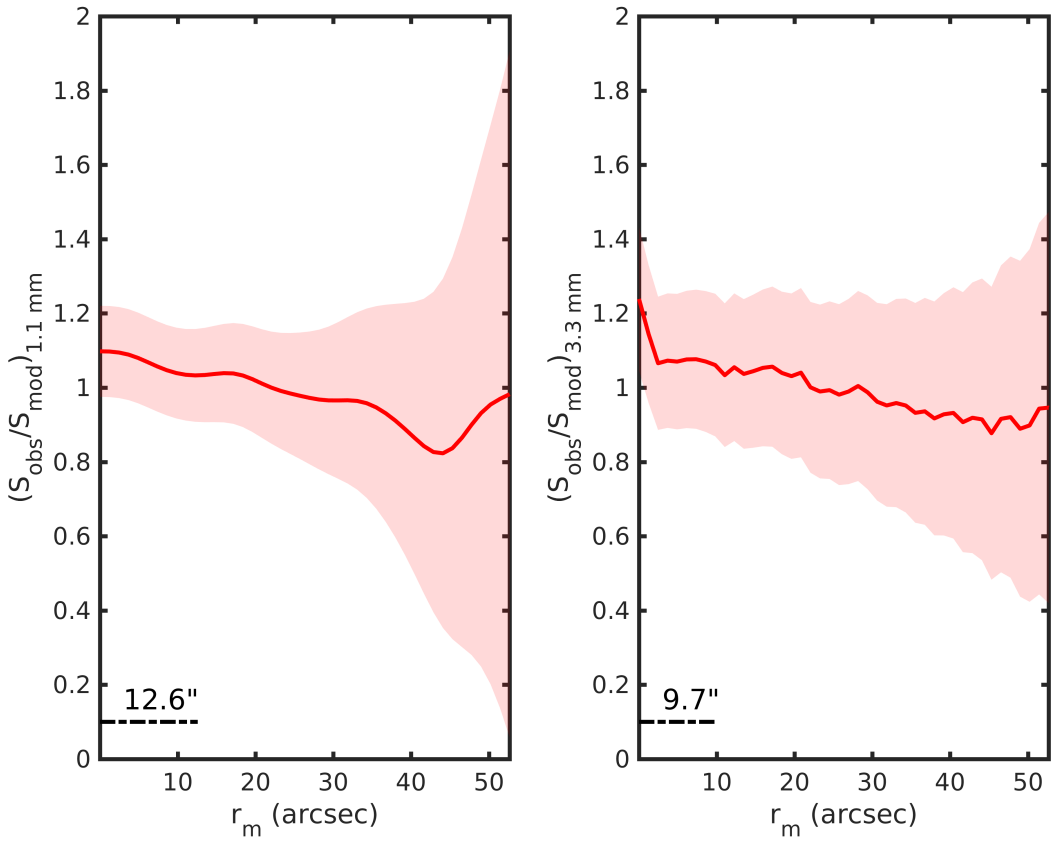

Figure C.7: Ratio between the observed emission profiles and the modeled emission profiles taking into account the radial opacity variations and new density and temperature profiles, as explained in Section 4.6.1. The shaded regions show the noise associated with the data, and the bars the resolution of the data.

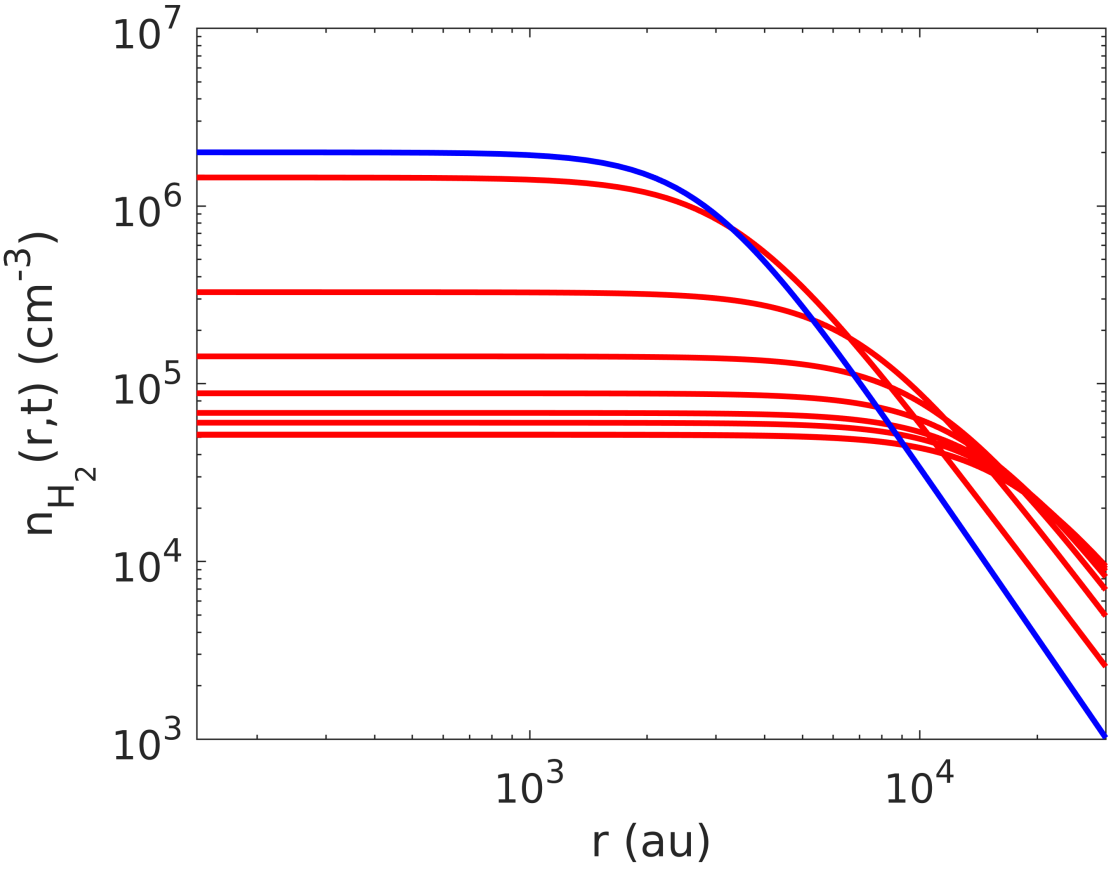

Figure C.8: Variation of the density with time extrapolated from that of Keto et al. (2015). The times at which the density is shown are, from low density to higher density: 0.06, 0.10, 0.60, 0.73, 0.85, 0.94, 1.01, 1.05 Myrs, and the current one, in blue, at t$\sim$1.06 Myrs.

Bibliography

Adam, R., Bartalucci, I., Pratt, G. W., et al. 2017, A&A, 598, A115

Adam, R., Comis, B., Macías-Pérez, J.-F., et al. 2015, A&A, 576, A12

Agladze, N. I., Sievers, A. J., Jones, S. A., Burlitch, J. M., & Beckwith, S. V. W. 1996, ApJ, 462, 1026

Aikawa, Y., Wakelam, V., Hersant, F., Garrod, R. T., & Herbst, E. 2012, ApJ, 760, 40

Andersen, M., Thi, W.-F., Steinacker, J., & Tothill, N. 2014, A&A, 568, L3

André, P., Men'shchikov, A., Bontemps, S., et al. 2010, A&A, 518, L102

Astropy Collaboration, Robitaille, T. P., Tollerud, E. J., et al. 2013, A&A, 558, A33

Bacmann, A., Lefloch, B., Ceccarelli, C., et al. 2003, ApJ, 585, L55

Bergin, E. A. & Tafalla, M. 2007, ARA&A, 45, 339

Bergman, P., Parise, B., Liseau, R., & Larsson, B. 2011, A&A, 527, A39

Bertincourt, B., Lagache, G., Martin, P. G., et al. 2016, A&A, 588, A107

Bianchi, E., Codella, C., Ceccarelli, C., et al. 2017, MNRAS, 467, 3011

Bizzocchi, L., Caselli, P., Spezzano, S., & Leonardo, E. 2014, A&A, 569, A27

Black, J. H. 1994, in Astronomical Society of the Pacific Conference Series, Vol. 58, The First Symposium on the Infrared Cirrus and Diffuse Interstellar Clouds, ed. R. M. Cutri & W. B. Latter, 355

Blum, J. 2004, in Astronomical Society of the Pacific Conference Series, Vol. 309, Astrophysics of Dust, ed. A. N. Witt, G. C. Clayton, & B. T. Draine, 369

Blum, J. & Schräpler, R. 2004, Physical Review Letters, 93, 115503

Bocquet, R., Demaison, J., Cosléou, J., et al. 1999, Journal of Molecular Spectroscopy, 195, 345

Bohlin, R. C., Savage, B. D., & Drake, J. F. 1978, ApJ, 224, 132

Böhm-Vitense, E. 1992, Introduction to Stellar Astrophysics, 301

Bonnor, W. B. 1956, MNRAS, 116, 351

Boogert, A. C. A., Gerakines, P. A., & Whittet, D. C. B. 2015, ARA&A, 53, 541

Boudet, N., Mutschke, H., Nayral, C., et al. 2005, ApJ, 633, 272

Bracco, A., Palmeirim, P., André, P., et al. 2017, A&A, 604, A52

Bracewell, R. N. 1986, The Fourier Transform and its applications

Brünken, S., Sipilä, O., Chambers, E. T., et al. 2014, Nature, 516, 219

Calvo, M., Roesch, M., Désert, F.-X., et al. 2013, A&A, 551, L12

Calzetti, D., Wilson, G. W., Draine, B. T., et al. 2018, ApJ, 852, 106

Caselli, P., Bizzocchi, L., Keto, E., et al. 2017, A&A, 603, L1

Caselli, P. & Ceccarelli, C. 2012, A&A Rev., 20, 56

Caselli, P., Keto, E., Bergin, E. A., et al. 2012, ApJ, 759, L37

Caselli, P., van der Tak, F. F. S., Ceccarelli, C., & Bacmann, A. 2003, A&A, 403, L37

Caselli, P., Walmsley, C. M., Tafalla, M., Dore, L., & Myers, P. C. 1999, ApJ, 523, L165

Caselli, P., Walmsley, C. M., Zucconi, A., et al. 2002a, ApJ, 565, 331

Caselli, P., Walmsley, C. M., Zucconi, A., et al. 2002b, ApJ, 565, 344

Catalano, A., Calvo, M., Ponthieu, N., et al. 2014, A&A, 569, A9

Ceccarelli, C., Caselli, P., Bockelée-Morvan, D., et al. 2014, Protostars and Planets VI, 859

Chacón-Tanarro, A., Caselli, P., Bizzocchi, L., et al. 2017, A&A, 606, A142

Chen, M. C.-Y., Di Francesco, J., Johnstone, D., et al. 2016, ApJ, 826, 95

Clemens, D. P., Tassis, K., & Goldsmith, P. F. 2016, ApJ, 833, 176

Cornet, R. & Winnewisser, G. 1980, Journal of Molecular Spectroscopy, 80, 438

Cottingham, D. A. 1987, PhD thesis, Princeton Univ., NJ.

Coupeaud, A., Demyk, K., Meny, C., et al. 2011, A&A, 535, A124

Crapsi, A., Caselli, P., Walmsley, C. M., et al. 2005, ApJ, 619, 379

Crapsi, A., Caselli, P., Walmsley, M. C., & Tafalla, M. 2007, A&A, 470, 221

Dalgarno, A. & Lepp, S. 1984, ApJ, 287, L47

Debye, P. 1909, Annalen der Physik, 335, 57

Demyk, K., Meny, C., Leroux, H., et al. 2017, A&A, 606, A50

Demyk, K., Meny, C., Leroux, H., et al. 2013, in Proceedings of The Life Cycle of Dust in the Universe: Observations, Theory, and Laboratory Experiments (LCDU2013). 18-22 November, 2013. Taipei, Taiwan. Editors: Anja Andersen (University of Copenhagen, Denmark), Maarten Baes (Universiteit Gent, Belgium), Haley Gomez (Cardiff University, UK), Ciska Kemper (Academia Sinica, Taiwan), Darach Watson (University of Copenhagen, Denmark). Online at <A href="http://pos.sissa.it/cgi-bin/reader/conf.cgi?confid=207">http://pos.sissa.it/cgi-bin/reader/conf.cgi?confid=207</A>, id.44, 44

Dicker, S. R., Ade, P. A. R., Aguirre, J., et al. 2014, Journal of Low Temperature Physics, 176, 808

Dorschner, J., Begemann, B., Henning, T., Jaeger, C., & Mutschke, H. 1995, A&A, 300, 503

Draine, B. T. 2006, ApJ, 636, 1114

Draine, B. T. 2011, Physics of the Interstellar and Intergalactic Medium

Emprechtinger, M., Caselli, P., Volgenau, N. H., Stutzki, J., & Wiedner, M. C. 2009, A&A, 493, 89

Forbrich, J., Lada, C. J., Lombardi, M., Román-Zúñiga, C., & Alves, J. 2015, A&A, 580, A114

Foster, J. B., Mandel, K. S., Pineda, J. E., et al. 2013, MNRAS, 428, 1606

Goldsmith, D. 2001, Search for Life in the Universe, 3rd Ed. (University Science Books)

Gould, R. J. & Salpeter, E. E. 1963, ApJ, 138, 393

Herbst, E. & Klemperer, W. 1973, ApJ, 185, 505

Herbst, E. & van Dishoeck, E. F. 2009, ARA&A, 47, 427

Hildebrand, R. H. 1983, QJRAS, 24, 267

Hincks, A. D., Acquaviva, V., Ade, P. A. R., et al. 2010, ApJS, 191, 423

Hollenbach, D. & Salpeter, E. E. 1970, J. Chem. Phys., 53, 79

Jones, A. P., Fanciullo, L., Köhler, M., et al. 2013, A&A, 558, A62

Juvela, M., Demyk, K., Doi, Y., et al. 2015a, A&A, 584, A94

Juvela, M., Ristorcelli, I., Marshall, D. J., et al. 2015b, A&A, 584, A93

Kauffmann, J., Bertoldi, F., Bourke, T. L., Evans, II, N. J., & Lee, C. W. 2008, A&A, 487, 993

Keto, E. & Caselli, P. 2010, MNRAS, 402, 1625

Keto, E., Caselli, P., & Rawlings, J. 2015, MNRAS, 446, 3731

Keto, E., Rawlings, J., & Caselli, P. 2014, MNRAS, 440, 2616

Keto, E. & Rybicki, G. 2010, ApJ, 716, 1315

Klapper, G., Surin, L., Lewen, F., et al. 2003, ApJ, 582, 262

Köhler, M., Ysard, N., & Jones, A. P. 2015, A&A, 579, A15

Kong, S., Caselli, P., Tan, J. C., Wakelam, V., & Sipilä, O. 2015, ApJ, 804, 98

Könyves, V., André, P., Men'shchikov, A., et al. 2015, A&A, 584, A91

Kruegel, E. & Siebenmorgen, R. 1994, A&A, 288, 929

Latusseck, A. 2008, Journal of Astronomical History and Heritage, 11, 235

Lazarian, A. & Hoang, T. 2007, ApJ, 669, L77

LeBlanc, F. 2010, An Introduction to Stellar Astrophysics

Lefèvre, C., Pagani, L., Min, M., Poteet, C., & Whittet, D. 2016, A&A, 585, L4

Linsky, J. L., Draine, B. T., Moos, H. W., et al. 2006, ApJ, 647, 1106

Lynds, B. T. 1962, ApJS, 7, 1

Mangum, J. G., Emerson, D. T., & Greisen, E. W. 2007, A&A, 474, 679

Mathis, J. S., Mezger, P. G., & Panagia, N. 1983, A&A, 128, 212

Mathis, J. S., Rumpl, W., & Nordsieck, K. H. 1977, ApJ, 217, 425

Mennella, V., Baratta, G. A., Palumbo, M. E., & Bergin, E. A. 2006, ApJ, 643, 923

Mennella, V., Brucato, J. R., Colangeli, L., et al. 1998, ApJ, 496, 1058

Mennella, V., Palumbo, M. E., & Baratta, G. A. 2004, ApJ, 615, 1073

Mie, G. 1908, Annalen der Physik, 330, 377

Min, M., Hovenier, J. W., de Koter, A., Waters, L. B. F. M., & Dominik, C. 2005, Icarus, 179, 158

Minissale, M., Dulieu, F., Cazaux, S., & Hocuk, S. 2016, A&A, 585, A24

Miyake, K. & Nakagawa, Y. 1993, Icarus, 106, 20

Muller, H. S. P., Gendriesch, R., Margules, L., et al. 2000, Phys. Chem. Chem. Phys., 2, 3401

Müller, H. S. P., Schlöder, F., Stutzki, J., & Winnewisser, G. 2005, Journal of Molecular Structure, 742, 215

Müller, H. S. P., Thorwirth, S., Roth, D. A., & Winnewisser, G. 2001, A&A, 370, L49

Müller, H. S. & Lewen, F. 2017, Journal of Molecular Spectroscopy, 331, 28

Natta, A. & Testi, L. 2004, in Astronomical Society of the Pacific Conference Series, Vol. 323, Star Formation in the Interstellar Medium: In Honor of David Hollenbach, ed. D. Johnstone, F. C. Adams, D. N. C. Lin, D. A. Neufeeld, & E. C. Ostriker, 279

Ohashi, N., Lee, S. W., Wilner, D. J., & Hayashi, M. 1999, ApJ, 518, L41

Ormel, C. W. & Cuzzi, J. N. 2007, A&A, 466, 413

Ormel, C. W., Min, M., Tielens, A. G. G. M., Dominik, C., & Paszun, D. 2011, A&A, 532, A43

Ormel, C. W., Paszun, D., Dominik, C., & Tielens, A. G. G. M. 2009, A&A, 502, 845

Ossenkopf, V. 1993, A&A, 280, 617

Ossenkopf, V. & Henning, T. 1994, A&A, 291, 943

Pagani, L., Steinacker, J., Bacmann, A., Stutz, A., & Henning, T. 2010, Science, 329, 1622

Parise, B., Castets, A., Herbst, E., et al. 2004, A&A, 416, 159

Parise, B., Ceccarelli, C., Tielens, A. G. G. M., et al. 2006, A&A, 453, 949

Parise, B., Ceccarelli, C., Tielens, A. G. G. M., et al. 2002, A&A, 393, L49

Parise, B., Leurini, S., Schilke, P., et al. 2009, A&A, 508, 737

Pearson, J. C., Yu, S., & Drouin, B. J. 2012, in 67th International Symposium on Molecular Spectroscopy, RF12

Planck Collaboration, Adam, R., Ade, P. A. R., et al. 2016, A&A, 594, A10

Punanova, A., Caselli, P., Feng, S., et al. 2018, ApJ, 855, 112

Roberts, H., Herbst, E., & Millar, T. J. 2003, ApJ, 591, L41

Rohlfs, K. & Wilson, T. L. 2004, Tools of radio astronomy

Roy, A., André, P., Palmeirim, P., et al. 2014, A&A, 562, A138

Ruffle, D. P. & Herbst, E. 2001, MNRAS, 324, 1054

Sadavoy, S. I., Stutz, A. M., Schnee, S., et al. 2016, A&A, 588, A30

Schnee, S. & Goodman, A. 2005, ApJ, 624, 254

Schnee, S., Mason, B., Di Francesco, J., et al. 2014, MNRAS, 444, 2303

Scott, K. S., Austermann, J. E., Perera, T. A., et al. 2008, MNRAS, 385, 2225

Shetty, R., Kauffmann, J., Schnee, S., & Goodman, A. A. 2009a, ApJ, 696, 676

Shetty, R., Kauffmann, J., Schnee, S., Goodman, A. A., & Ercolano, B. 2009b, ApJ, 696, 2234

Sipilä, O., Caselli, P., & Harju, J. 2015a, A&A, 578, A55

Sipilä, O., Harju, J., Caselli, P., & Schlemmer, S. 2015b, A&A, 581, A122

Sipilä, O., Spezzano, S., & Caselli, P. 2016, A&A, 591, L1

Spezzano, S., Bizzocchi, L., Caselli, P., Harju, J., & Brünken, S. 2016, A&A, 592, L11

Spezzano, S., Brünken, S., Schilke, P., et al. 2013, ApJ, 769, L19

Stahler, S. W. & Palla, F. 2005, The Formation of Stars, 865

Stanchfield, S. M., Ade, P. A. R., Aguirre, J., et al. 2016, Journal of Low Temperature Physics, 184, 460

Tafalla, M., Mardones, D., Myers, P. C., et al. 1998, ApJ, 504, 900

Tafalla, M., Myers, P. C., Caselli, P., Walmsley, C. M., & Comito, C. 2002, ApJ, 569, 815

Taquet, V., Ceccarelli, C., & Kahane, C. 2012, ApJ, 748, L3

Testi, L., Birnstiel, T., Ricci, L., et al. 2014, Protostars and Planets VI, 339

Tielens, A. G. G. M. 2005, The Physics and Chemistry of the Interstellar Medium

Tielens, A. G. G. M. & Hagen, W. 1982, A&A, 114, 245

Toon, O. B. & Ackerman, T. P. 1981, Appl. Opt., 20, 3657

van der Walt, S., Colbert, S. C., & Varoquaux, G. 2011, Computing in Science & Engineering, 13, 22

Vastel, C., Ceccarelli, C., Lefloch, B., & Bachiller, R. 2014, ApJ, 795, L2

Vasyunin, A. I., Caselli, P., Dulieu, F., & Jiménez-Serra, I. 2017, ApJ, 842, 33

Vasyunin, A. I. & Herbst, E. 2013, ApJ, 769, 34

Vasyunin, A. I., Semenov, D., Henning, T., et al. 2008, ApJ, 672, 629

Vasyunin, A. I., Sobolev, A. M., Wiebe, D. S., & Semenov, D. A. 2004, Astronomy Letters, 30, 566

Walmsley, C. M., Flower, D. R., & Pineau des Forêts, G. 2004, A&A, 418, 1035

Wang, K., Testi, L., Ginsburg, A., et al. 2015, MNRAS, 450, 4043

Ward-Thompson, D., Motte, F., & Andre, P. 1999, MNRAS, 305, 143

Watanabe, N. & Kouchi, A. 2002, ApJ, 571, L173

Whittet, D. C. B., Gerakines, P. A., Tielens, A. G. G. M., et al. 1998, ApJ, 498, L159

Wickramasinghe, N. C. & Hoyle, F., eds. 1991, Astrophysics and Space Science Library, Vol. 168, The Theory of Cosmic Grains

Willacy, K., Langer, W. D., & Velusamy, T. 1998, ApJ, 507, L171

Wilson, T. L. & Rood, R. 1994, ARA&A, 32, 191

Woitke, P., Min, M., Pinte, C., et al. 2016, A&A, 586, A103

Xu, L.-H. & Lovas, F. J. 1997, Journal of Physical and Chemical Reference Data, 26, 17

Yamamoto, S. 2017, Introduction to Astrochemistry: Chemical Evolution from Interstellar Clouds to Star and Planet Formation

Zhao, B., Caselli, P., Li, Z.-Y., et al. 2016, MNRAS, 460, 2050

Zubko, V. G., Mennella, V., Colangeli, L., & Bussoletti, E. 1996, MNRAS, 282, 1321

Zucconi, A., Walmsley, C. M., & Galli, D. 2001, A&A, 376, 650

Acknowledgments

I deeply thank you, Paola, for giving me the opportunity of living this huge experience and working on what I have always dreamed of. I have learned from the best, not only scientifically, but also personally.

A Luca y a Jaime, gracias, por vuestra dedicación, tiempo y paciencia. He aprendido muchísimo de vosotros y nunca podré estar suficientemente agradecida. To Jorma, who gave me a lot of good advises, always with a smile.

I also want to thank my Bachelor's thesis supervisor, Aurora, Carlos, and Min, who introduced me to the world of star formation, and shared with me an initial enthusiasm which was the reason that got me here. There are many professors from my former University that deserve a word, but the list would be too long. But I do not want to miss that word for Angelo; I still remember how, in the end, he was one of those people who made me believe in me.

A Víctor, que aún no sé cómo accedió a ayudarme, pero al que le debo un gran gracias. Gracias también a Felipe y Michela, por contestar a esas dudas de última hora. To Angelika, for being always so kind with all of us.

To my friends, office mates, my group. Thank you CAS group, to all of you. In particular, to Vlas, Anna and Birgitta, for your help in these last steps and for not killing me any time spiders appeared, or for forgiving my obsession with windows and heating. To Carolina, Elena, Johanna, Domenico, and Ashley, for sharing with me so many moments, stress and frustration included. To Gisela, for being there from the distance. I keep with me a lot of new friends and moments, thanks to all of you.

A mi familia, mis padres, Ana y Enrique, y mis hermanos, Kike, Pablo y Carmen, quienes me han apoyado desde la distancia y han cogido un avión cada vez que lo necesitaba. A mis abuelos, y en especial a Agustín y Encarnita, quienes han sido mi luz, mi inspiración y mi razón de luchar por ser mejor. Os echaré siempre de menos, y ojalá pueda ser como vosotros algún día. A mi pequeño sobrino, por ser esa luz necesaria para nuestra familia cuando nos hace falta. A mis tíos, tías, primos y primas. Sois la razón por la que me considero afortunada. Y en especial, me gustaría agradecer a Magdalena y José, quienes dedicaron su tiempo a ayudarme a conseguir esta oportunidad, y a Isabel, por hacer que nuestro punto en común sea especial.

A mi segunda familia, gracias por hacerme sentir como una más desde el primer día.

A mis amigos de España. A los del pueblo, los del instituto, los de la carrera, los de Lupiana, los de Cercedilla, todos. Se os echa de menos, y habéis sido un gran pilar en mi

vida. Pero en especial a Gloria, por soportarme tantos y tantos años, y a su familia, por tener siempre sus puertas abiertas. A Lidia, por ayudarnos con el alemán cada vez que veíamos que nos llevaba por delante y por estar ahí. A Paula, Isa y Laura, por aparecer en ciertos momentos que fueron claves. To Sydney, to my American family, thank you for being there.

A ti, por estar siempre ahí, por vernirte a vivir conmigo esta aventura. Sin ti no lo hubiese conseguido. Gracias a ti he podido disfrutar y vivir esta experiencia como una de las mejores de mi vida. Te quiero.

Thank you all. Gracias a todos.